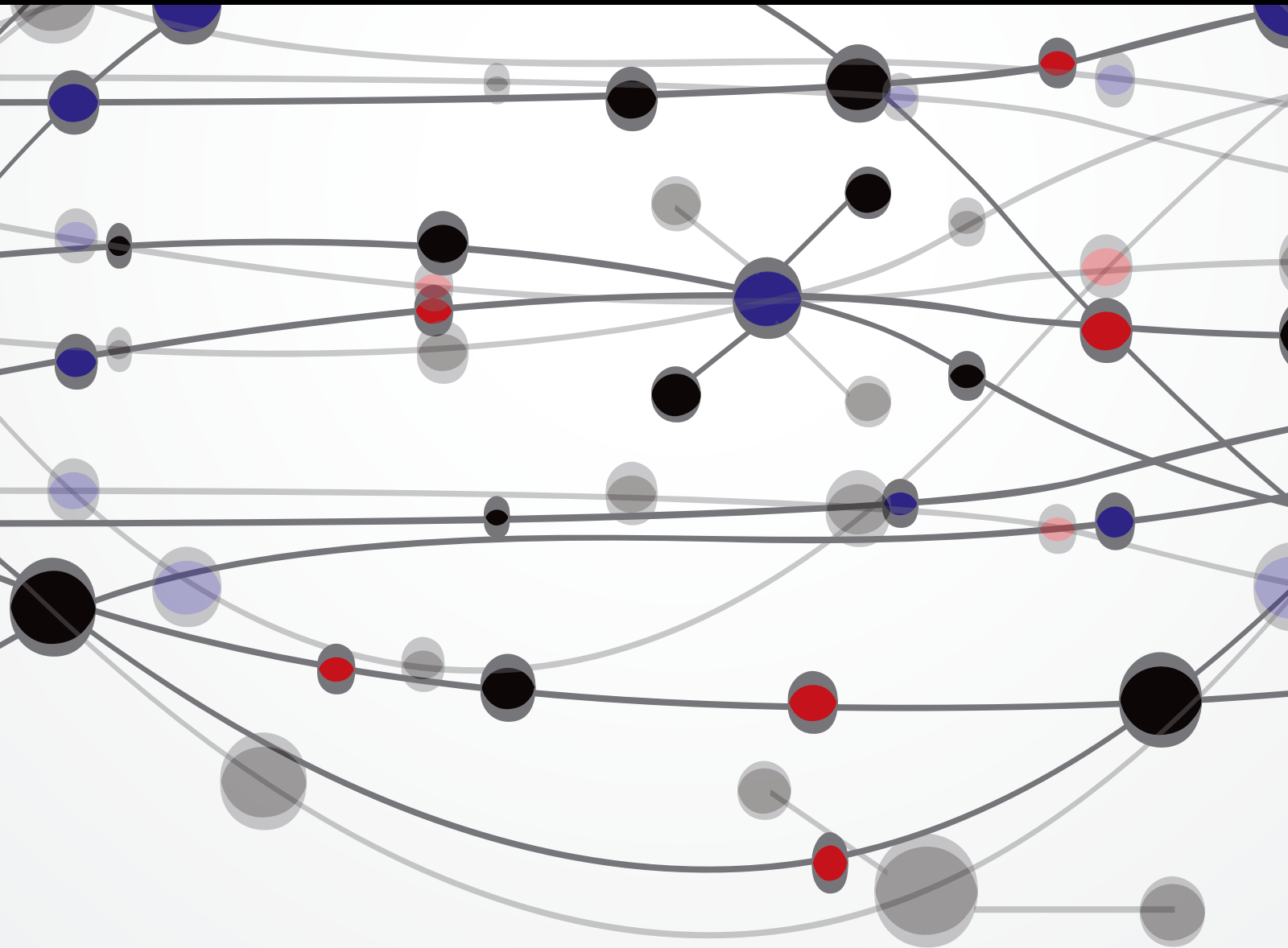


Computational Simulations in the Cardiovascular System

Guest Editors: Aike Qiao, Hai-Chao Han, Makoto Ohta, and Yi Qian





Computational Simulations in the Cardiovascular System

The Scientific World Journal

Computational Simulations in the Cardiovascular System

Guest Editors: Aike Qiao, Hai-Chao Han, Makoto Ohta,
and Yi Qian



Copyright © 2014 Hindawi Publishing Corporation. All rights reserved.

This is a special issue published in “The Scientific World Journal.” All articles are open access articles distributed under the Creative Commons Attribution License, which permits unrestricted use, distribution, and reproduction in any medium, provided the original work is properly cited.

Contents

Computational Simulations in the Cardiovascular System, Aike Qiao, Hai-Chao Han, Makoto Ohta, and Yi Qian

Volume 2014, Article ID 253619, 1 page

How Does Calcification Influence Plaque Vulnerability? Insights from Fatigue Analysis, Baijian Wu, Xuan Pei, and Zhi-Yong Li

Volume 2014, Article ID 417324, 8 pages

Drug Release Analysis and Optimization for Drug-Eluting Stents, Hongxia Li, Yihao Zhang, Bao Zhu, Jinying Wu, and Xicheng Wang

Volume 2013, Article ID 827839, 5 pages

Blood Clot Simulation Model by Using the Bond-Graph Technique, Gregorio Romero, M. Luisa Martinez, Joaquin Maroto, and Jesus Felez

Volume 2013, Article ID 519047, 10 pages

Use of Computational Fluid Dynamics to Estimate Hemodynamic Effects of Respiration on Hypoplastic Left Heart Syndrome Surgery: Total Cavopulmonary Connection Treatments, Jinlong Liu, Yi Qian, Qi Sun, Jinfen Liu, and Mitsuo Umezu

Volume 2013, Article ID 131597, 12 pages

Preliminary Computational Hemodynamics Study of Double Aortic Aneurysms under Multistage Surgical Procedures: An Idealised Model Study, Yosuke Otsuki, Nhat Bui Minh, Hiroshi Ohtake, Go Watanabe, and Teruo Matsuzawa

Volume 2013, Article ID 601470, 9 pages

Transient Hemodynamic Changes upon Changing a BCPA into a TCPC in Staged Fontan Operation: A Computational Model Study, Fuyou Liang, Hideaki Senzaki, Zhaofang Yin, Yuqi Fan, Koichi Sugimoto, and Hao Liu

Volume 2013, Article ID 486815, 10 pages

Design Optimization of Coronary Stent Based on Finite Element Models, Hongxia Li, Tianshuang Qiu, Bao Zhu, Jinying Wu, and Xicheng Wang

Volume 2013, Article ID 630243, 10 pages

Propose a Wall Shear Stress Divergence to Estimate the Risks of Intracranial Aneurysm Rupture, Y. Zhang, H. Takao, Y. Murayama, and Y. Qian

Volume 2013, Article ID 508131, 8 pages

Why Is ABI Effective in Detecting Vascular Stenosis? Investigation Based on Multibranch Hemodynamic Model, Xiaoyun Li, Ling Wang, Chi Zhang, Shuyu Li, Fang Pu, Yubo Fan, and Deyu Li

Volume 2013, Article ID 185691, 10 pages

Editorial

Computational Simulations in the Cardiovascular System

Aike Qiao,¹ Hai-Chao Han,² Makoto Ohta,³ and Yi Qian⁴

¹ College of Life Science and Bioengineering, Beijing University of Technology, Pingleyuan 100, Chaoyang District, Beijing 100124, China

² Department of Mechanical Engineering, The University of Texas at San Antonio, 1 UTSA Circle San Antonio, TX 78249, USA

³ Intelligent Fluid Systems Division Institute of Fluid Science, Tohoku University, 2-1-1 Katahira, Aoba-ku, Sendai, Miyagi 980-8577, Japan

⁴ Australian School of Advanced Medicine, Macquarie University, 2 Technology Place, NSW 2109, Australia

Correspondence should be addressed to Aike Qiao; qak@bjut.edu.cn

Received 26 February 2014; Accepted 26 February 2014; Published 7 April 2014

Copyright © 2014 Aike Qiao et al. This is an open access article distributed under the Creative Commons Attribution License, which permits unrestricted use, distribution, and reproduction in any medium, provided the original work is properly cited.

Cardiovascular diseases are the leading cause of mortality worldwide. Understanding the mechanism and developing techniques for diagnosis, treatment, and prevention remain as challenging issues. Biomechanics research plays an important role in all these aspects. Computer-based simulations of dynamic processes in the cardiovascular system are emerging as a powerful tool in delineating the biomechanical mechanisms and developing new treatment technologies for cardiovascular diseases. Although there have been extensive studies in these areas, many issues remain unsolved. The articles collected in this special issue presented new advances on the modeling and simulations of processes involving stenosis, clot, plaque, aneurysm, left ventricle syndrome, and so forth. These results reveal significant insights into the prediction, evaluation, and treatment of cardiovascular diseases. We hope that this special issue will also advance research in medical devices and surgical planning through computational simulations.

*Aike Qiao
Hai-Chao Han
Makoto Ohta
Yi Qian*

Research Article

How Does Calcification Influence Plaque Vulnerability? Insights from Fatigue Analysis

Baijian Wu,¹ Xuan Pei,² and Zhi-Yong Li^{2,3}

¹ Department of Engineering Mechanics, Southeast University, Nanjing 210096, China

² School of Biological Science & Medical Engineering, Southeast University, Nanjing 210096, China

³ University Department of Radiology, University of Cambridge, Cambridge CB2 0QQ, UK

Correspondence should be addressed to Zhi-Yong Li; zylicam@gmail.com

Received 20 November 2013; Accepted 18 January 2014; Published 6 April 2014

Academic Editors: H.-C. Han and A. Qiao

Copyright © 2014 Baijian Wu et al. This is an open access article distributed under the Creative Commons Attribution License, which permits unrestricted use, distribution, and reproduction in any medium, provided the original work is properly cited.

Background. Calcification is commonly believed to be associated with cardiovascular disease burden. But whether or not the calcifications have a negative effect on plaque vulnerability is still under debate. *Methods and Results.* Fatigue rupture analysis and the fatigue life were used to evaluate the rupture risk. An idealized baseline model containing no calcification was first built. Based on the baseline model, we investigated the influence of calcification on rupture path and fatigue life by adding a circular calcification and changing its location within the fibrous cap area. Results show that 84.0% of calcified cases increase the fatigue life up to 11.4%. For rupture paths 10D far from the calcification, the life change is negligible. Calcifications close to lumen increase more fatigue life than those close to the lipid pool. Also, calcifications in the middle area of fibrous cap increase more fatigue life than those in the shoulder area. *Conclusion.* Calcifications may play a positive role in the plaque stability. The influence of the calcification only exists in a local area. Calcifications close to lumen may be influenced more than those close to lipid pool. And calcifications in the middle area of fibrous cap are seemingly influenced more than those in the shoulder area.

1. Introduction

Rupture of atherosclerotic plaque is a major cause of human mortality worldwide, which makes the prerule identification of vulnerable atheroma extremely important for patient risk evaluation. Evidences have shown that the composition of an atherosclerotic plaque, rather than its degree of stenosis or size, is usually of more importance for acute clinical events. Generally a vulnerable plaque is often found to be associated with a thin fibrous cap, a high inflammation burden, a large lipid pool, macroscopic heterogeneity, and so on [1, 2]. Calcification is commonly believed to be associated with cardiovascular disease burden [3–7]. Recently, the influence of calcification on plaque vulnerability has raised many research interests [8–12]. There are many ways to image the calcification in plaque, such as noninvasive molecular imaging probes. Chen and Dilsizian [13] used the molecular probe 18 F-sodium fluoride (18 F-NaF) for positron emission tomography (PET) imaging, which targets active

microcalcifications in atherosclerotic plaques. Kimura et al. [14] revealed a significantly higher frequency of lipid-rich plaque with microcalcification in lesions with echo signal attenuation.

The role that the calcification plays in plaque vulnerability is still under debate. Some studies indicated beneficial effects in stabilizing the plaque, making it stiffer and less prone to rupture [15, 16], while others tended to believe it would increase the risk of plaque rupture [3, 17]. Studies from Mauriello et al. [18] showed that the calcification, as well as its distance from the lumen, is not correlated with the presence of unstable plaques. Thus, the authors suggested that the calcification is not useful to identify the vulnerable plaque. Hermann et al. [19] found that individuals suffering a stroke have significantly higher coronary artery calcification (CAC) values at baseline than the remaining individuals, and furthermore CAC is an independent stroke predictor in addition to classical risk factors for those patients at low or intermediate vascular risk. Moreover, mechanical

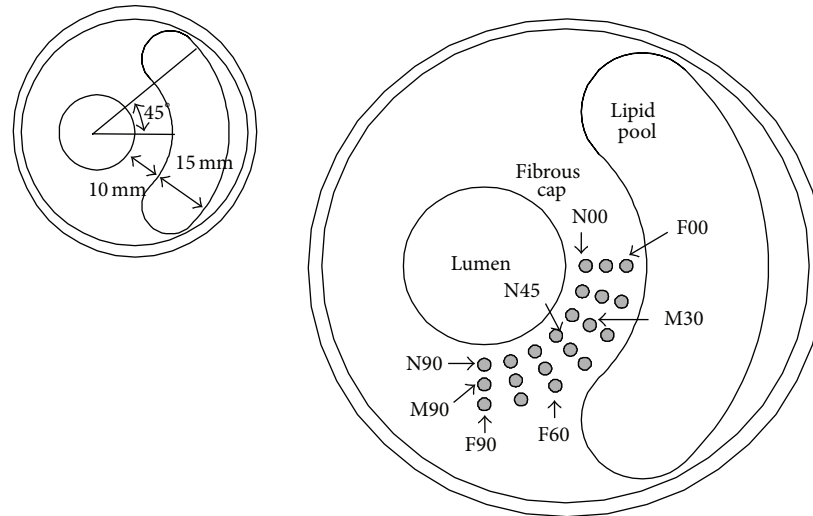


FIGURE 1: Different calcification cases. Here the capitals N, M, and F, respectively, mean a near, middle, and far distance from the lumen; and the number after the letter means the angle from the x -axis.

experiments on human carotid plaques by Mulvihill et al. [20] showed that calcification in the tissue structure may lead to increased vulnerability of the plaque. On the other hand, it was demonstrated by Shaalan et al. [21] that symptomatic plaques are less calcified and more inflamed than asymptomatic plaques, implying that the calcification may reduce the plaque rupture risk. Wahlgren et al. [22] investigated thirty carotid endarterectomy plaques which were classified as noncalcified and calcified and obtained a similar result that fibrous cap inflammation is more likely to occur in noncalcified than in calcified plaques, suggesting that plaque calcification may result in protection against the rupture of plaque.

Computational studies on microcalcifications have also been investigated previously. Kelly-Arnold et al. [23] examined the spatial distribution, clustering, and the shape of different microcalcification size in fibrous caps and found that nearly all fibrous caps have microcalcifications, but only a small subset has rupture potential. Bluestein et al. [24] developed a fluid-structure interaction (FSI) model to study the microcalcification effects on the plaque vulnerability and found that calcification can increase plaque vulnerability. Cilla et al. [25] investigated the effect of microcalcifications on the stress field of an atheroma plaque vessel section by performing a parametric finite element study on an idealized model. Vengrenyuk et al. [26] investigated the stress distribution using the multilevel micro-CT based 3D numerical modeling techniques. Results showed that the peak circumferential stress increases with the existence of calcifications (inclusions) and may grow even higher by elongated microcalcifications, while in contrast, macrocalcifications in cap shoulders were shown to actually increase the plaque stability.

Despite the above viewpoints that the stress induced by normal blood pressure or shearing flow characterizes the vulnerability of plaques, another possible mechanism that the rupture may result from fatigue accumulating process

has been investigated [27–29]. The remaining fatigue life of plaque thus may be used to evaluate the rupture risk [30, 31]. In the current study, we investigated the influence of calcium deposition on plaque rupture from the fatigue crack growth point of view. Here, we built an idealized model in which only one calcification is included. Based on the model, we investigated the influence of calcification on crack path and fatigue life. Moreover, we changed the calcification location in order to inquire its impact.

2. Methods

An idealized model was created with a blunt crescent-shaped lipid pool and a circular calcification embedded. The cross-section includes 5 parts: the arterial wall, the fibrous cap, the lumen, the lipid pool, and the calcified inclusion. The baseline cross-section without the calcification had the thickness of the fibrous cap as 10 mm, the thickness of the lipid pool as 15 mm, and the angle of the lipid pool which is used to control the length of the lipid pool as 45° .

The calcification was assumed to be a circular inclusion in fibrous cap area with the radius r of 0.8 mm. Calcified inclusions are put into variable locations to investigate their influence of the fatigue life as well as the vulnerability of the plaque. Here two parameters, the distance from the lumen d and the angle from the x -axis α , were used to locate the calcification center. In the study, d varied among 2.5 mm (Near), 5.0 mm (Middle), and 7.5 mm (Far), and α was among 0° , 15° , 30° , 45° , 60° , 75° , and 90° . Totally 21 different calcification locations as shown together in Figure 1 were investigated. In Figure 1, the capital letters N, M, and F, respectively, mean a near, middle, and far distance from the lumen; and number next to the letter means the angle from the x -axis.

In our study, plaque rupture was understood as a result of fatigue process under cyclic blood pressure. As the stress at the crack tip is infinity, we adopt stress intensity factor (SIF) K to describe the status at the crack tip. The Paris Law was

used to calculate the crack growth rate. Paris found that the fatigue crack growth rate is related to the change of SIF within one stress cycle, and the equation is

$$\frac{da}{dN} = C \cdot \Delta K^m. \quad (1)$$

Here a is the crack length. N is the number of cycles, namely, the number of heartbeats. K is the SIF change within one stress cycle (one heartbeat), namely, the K under the systolic pressure minus that under diastolic pressure. C and m are material constants. Since no fatigue test on human plaque has been reported so far, here the outcome from rubber will be used and C and m are, respectively, chosen given as $3.16E-5$ and 2.12 [32]. Using a different value of C and m would not change the general conclusions for this study.

The maximum circumferential stress criteria [33] were adopted to calculate the crack growth direction. In the theory, the growth angle θ , defined as the angle between the growth path and the local x' -axis, is determined by

$$\theta = \arctan \frac{K_{II}}{\sqrt{K_I^2 + 8K_{II}^2}} - \arctan \frac{3K_{II}}{K_I}. \quad (2)$$

In numerical simulation, the initial crack should be created first. Then the finite element model of the cracked vessel is solved. With the obtained $\Delta K(a_j)$, the crack growth rate and direction can be calculated through (1) and (2), respectively. The new crack tip could thus be predicted. And with updated crack tip, the above calculation starts again. This loop keeps running until the crack reaches the boundary of plaque boundary, that is, the lipid pool or artery wall. At this time, we will judge the plaque as “ruptured,” and the crack growth path L as well as the total number of heartbeats N_r could be obtained. Thus, the plaque life T for this rupture path L could be estimated as

$$T_L = \frac{N_r}{\text{Heart rate}}. \quad (3)$$

As said above, the study includes a baseline vessel and 21 calcified vessels. Here for each *vessel case*, we also introduce many different crack initial locations. Each crack initialization— we called it one *computational case*—leads to a crack growth path L and its corresponding plaque life T_L . These crack growth paths could be understood as possible rupture paths for the plaque. Thus, the value of computed plaque life could thus be used to evaluate the possibility of a rupture path. A longer life implies a lower rupture risk within a fixed and upcoming time period, one year for instance, and vice versa.

In the study, initial cracks in baseline cross-section were manually created from 0° to 180° with a step of 9° , respectively (21 cases). Correspondingly, the results are used as baseline values for comparison. Initial cracks for calcified cross-sections are created mainly from $\alpha - 45^\circ$ to $\alpha + 45^\circ$, also with a step of 9° (10~12 cases for each cross-section). This is because the calcification is relatively in a very small size that cracks initialized farther than $\alpha \pm 45^\circ$ will lead to nearly the same results as that of the baseline.

The numerical simulation was implemented in the finite element software ABAQUS (Version 6.10, Providence,

RI). The distributed blood pressure (a systolic pressure of 120 mm Hg and a diastolic pressure of 80 mm Hg) is applied on the lumen surface. The heart rate is given as 70 per minute here. 8-node quadrilateral elements are used to mesh all models, while collapsed triangle elements are distributed around the crack tip.

Linear and elastic constitutive relation is used for all plaque components. The Young modulus of the arterial wall, the fibrous cap, the lipid pool, and the calcification was chosen as $E_w = 0.3$ Mpa, $E_p = 0.6$ Mpa, $E_l = 0.02$ Mpa, and $E_c = 10$ Mpa, respectively [30]. Poisson's ratio for each component was set as $\nu_w = \nu_p = \nu_l = \nu_c = 0.48$.

3. Results

As said above, our computations covered the baseline vessel and 21 calcified vessels. Also, there are 21 crack attempts of initialization (computational cases) for the baseline and 10~12 for the calcified cases. Totally $21 + 231 = 252$ cases are calculated. Results are shown in Figure 2, in which a rupture path corresponds to a computational case. It could be found that the calcification seemly will not significantly change the baseline rupture directions.

The fatigue life changes due to the calcification at all crack paths are investigated, aiming to answer the following three questions. (1) Does the calcification influence the plaque vulnerability, positively or negatively? (2) How large a scope of area the calcification will influence? (3) Does the influence depend on the location of calcification?

3.1. Calcification May Increase Plaque Stability. All data are collected and box-plotted together in Figure 3. It could be seen that, for 194 out of 231 calcified cases (84.0%), the fatigue life of the plaque increases up to 11.4%. In contrast, the biggest life decrease is just -1.3% , which actually could be ignored. Therefore, it could be inferred that the existence of calcifications may play a positive role in the plaque stability.

3.2. Influence Scope. To investigate scope of area in which the calcification may influence, all results are regrouped and plotted together in Figure 4. Here the x -axis is a ratio between crack-calcification distance d_{CL} and the calcification diameter D (1.6 mm), where d_{CL} means the distance from the calcification center to the calculated rupture path. The y -axis is the fatigue life changed (in percentage) due to the calcification.

It could be found that the calcification most possibly influence the rupture paths of which the d_{CL}/D are among 1~6, while for those paths directly going through the calcification, fatigue life seemly changes little. Also, it is found that when $d_{CL}/D > 10$, the influences are all below $\pm 2\%$. It is said that, for areas $10D$ far from the calcification, the influence is negligible. The influence scope of area is about $10D$.

3.3. Calcification Locations. To investigate if the above influence of calcifications depends on their locations, first for each calcified cross-section, we extract the max life changes among all crack paths. Then results for all 15 calcified vessels are

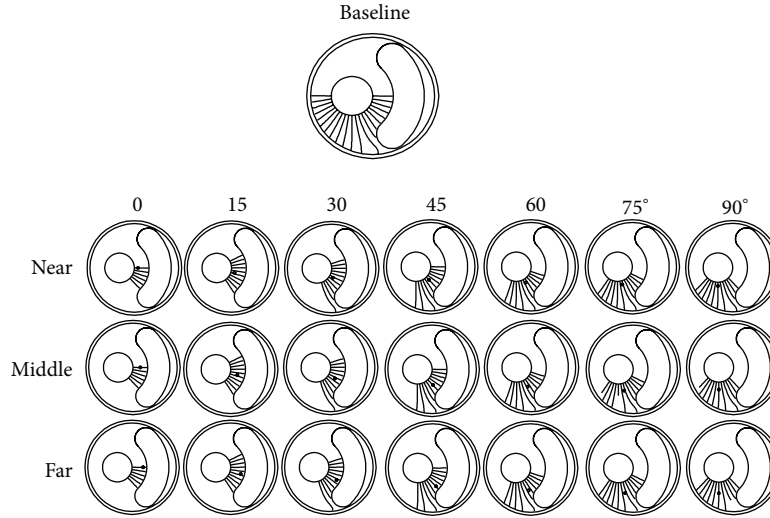


FIGURE 2: Rupture paths for all cases.

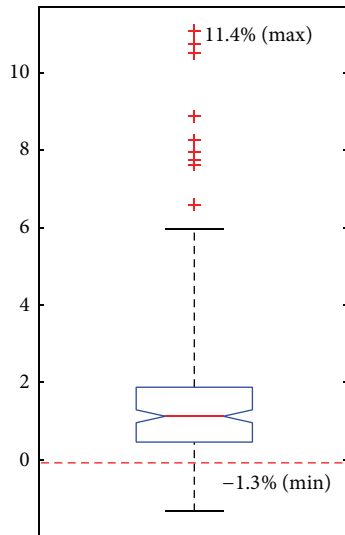


FIGURE 3: Fatigue life changes (%).

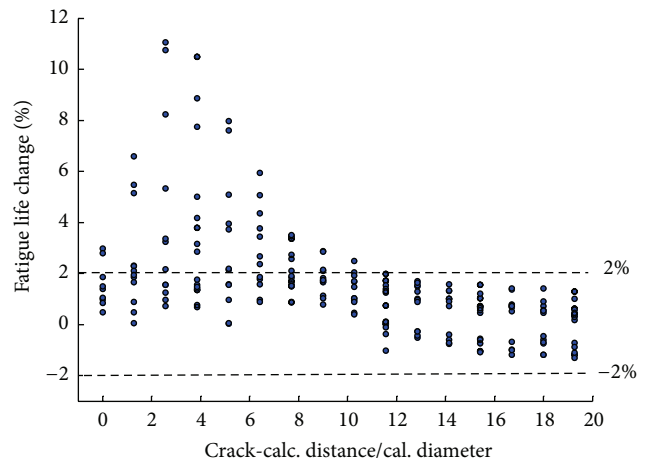


FIGURE 4: Relationship between crack-calcification distance and fatigue life changes.

plotted together in Figure 5. It is found that calcification close to lumen may be influenced more than those close to lipid pool. Besides that, calcifications locating in the middle area (small α) of fibrous cap are seemingly influenced more than those in the shoulder area (large α).

4. Discussion

The role that the calcification plays in plaque vulnerability is controversial. In the study, the results tend to show that it may increase plaque stability, which generally agrees with the viewpoints in [21, 22, 34]. Here we try to explain the mechanisms from the biomechanical insights. First, as we know, the rupture is mainly due to the tensile force/stress. If the potential rupture path is known, locally the dominated stress status should be in tension and be perpendicular to

the rupture path (Figure 6(a)). We define a local coordinate system here that 1-direction and 2-direction are parallel to the rupture path and the tensile stress, respectively. Then the calcification, a hard inclusion embedded in a soft matrix (the plaque), is considered. Figure 6(b) shows the result of σ_{22} field induced by the calcification and the remote tensile stress. It is found that, in the neighborhood of the calcification, stress in Zone 1 (Figure 6(c)) slightly decreases and in Zone 2, the stress increases; that is to say, the risk of plaque broken in Zone 1 decreases, while the broken risk in Zone 2 increases. Now, we assume a crack or plaque damage occurs on the upper and lower side (the largest stress concentration location as shown in Figure 6(b)), for which the deformation field could be solved and shown in Figure 6(d). It could be found that still due to the hard inclusion (the calcification) the left and right sides extrude the calcification even more, and at

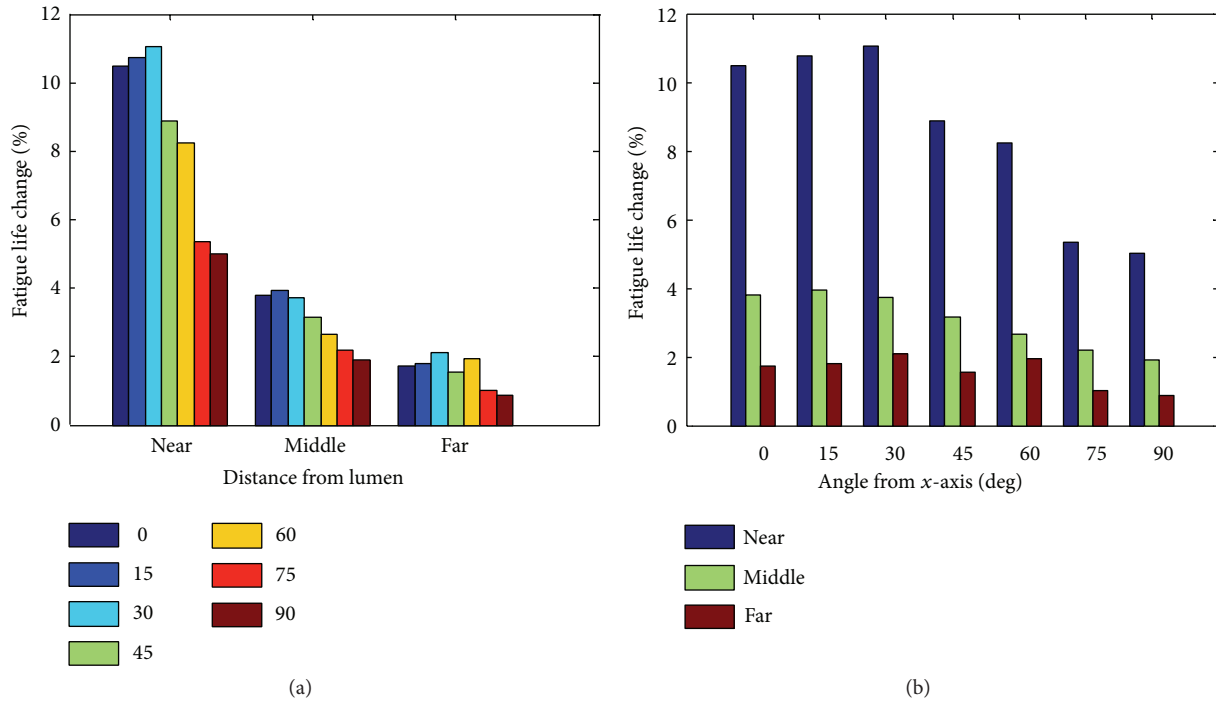


FIGURE 5: Calcification locations and fatigue life changes.

the same time, the damage/crack in the upper and lower side intensifies. A new rupture direction in fact generates and blocks the direction of original rupture path (Figure 6(e)), which may finally explain why the calcification increases the stability.

From the classical viewpoint that the maximal stress value characterizes the vulnerability, here the plaque stability should decrease because the stress near the upper and lower side of the calcification significantly increases, as shown in Figure 6(b). It should be noted that researches have shown that ruptures often (for about 40%) occur in regions where the numerical model does not predict the maximal stress [8]. Here we suggest that detailed analysis on failure modes/paths should also be taken into account. For example, obviously the stress concentration happens in nearly all material heterogeneous cases. However, equally as a heterogeneous inclusion, a hard calcification or a weakened void caused by inflammation may lead to totally different results even though they all have stress concentrations around.

It is interesting that the calcification influences the rupture paths a little far from it (with d_{CL}/D among 1~6) more than those directly going through it. This may coincide with the mechanisms revealed above that, for cases of $1 < d_{CL}/D < 6$, cracks may grow into Zone 2 and retard due to the reason shown in Figure 6(e). Seemly for cases $d_{CL}/D < 1$, the retard of crack growth which is mainly caused by the stress reduction in Zone 1 is not so significant.

The position of calcification is thought to be of importance for rupture risk stratification by some researches [35, 36], where it is found that calcification locating in middle cap area is influenced more than that in shoulder area. Results

are similar in this study (Figure 5). As for the distance of calcification from the lumen, this study shows that calcification close to lumen may be influenced more than that close to lipid pool, while some studies reported that they have no obvious difference [18]. In our study, areas near to lumen usually have greater circumferential tensile stresses than those far from lumen. Greater stresses usually lead to a more rapid crack growth, which consequently will change the life more. This may be the reason for our outcome.

It should be noted that only one calcified inclusion embedded in fibrous cap is considered. Actually there may have several calcifications coalesced together, which may lead to extra influences. Also, the baseline fibrous cap is not an extremely thin case; a much thinner cap possibly has other effects because the calcification may strongly influence the stress distribution nearby. These two aspects are planned to be considered.

5. Conclusion

Calcifications may play a positive role in the plaque vulnerability—at least not negative. In our study, the max fatigue life increase is about 12% with the radius of calcification 0.8 mm. Considering that the practical size is much less, actual influence may be even small. The influence of the calcification is local rather than global, which is mainly concentrated in an area in the size of $10D$ neighborhood. It is found that calcification close to the lumen may be influenced more than those close to the lipid pool. And calcifications located in the middle area of fibrous cap are seemly influenced more than those in the shoulder area. In all, since calcification

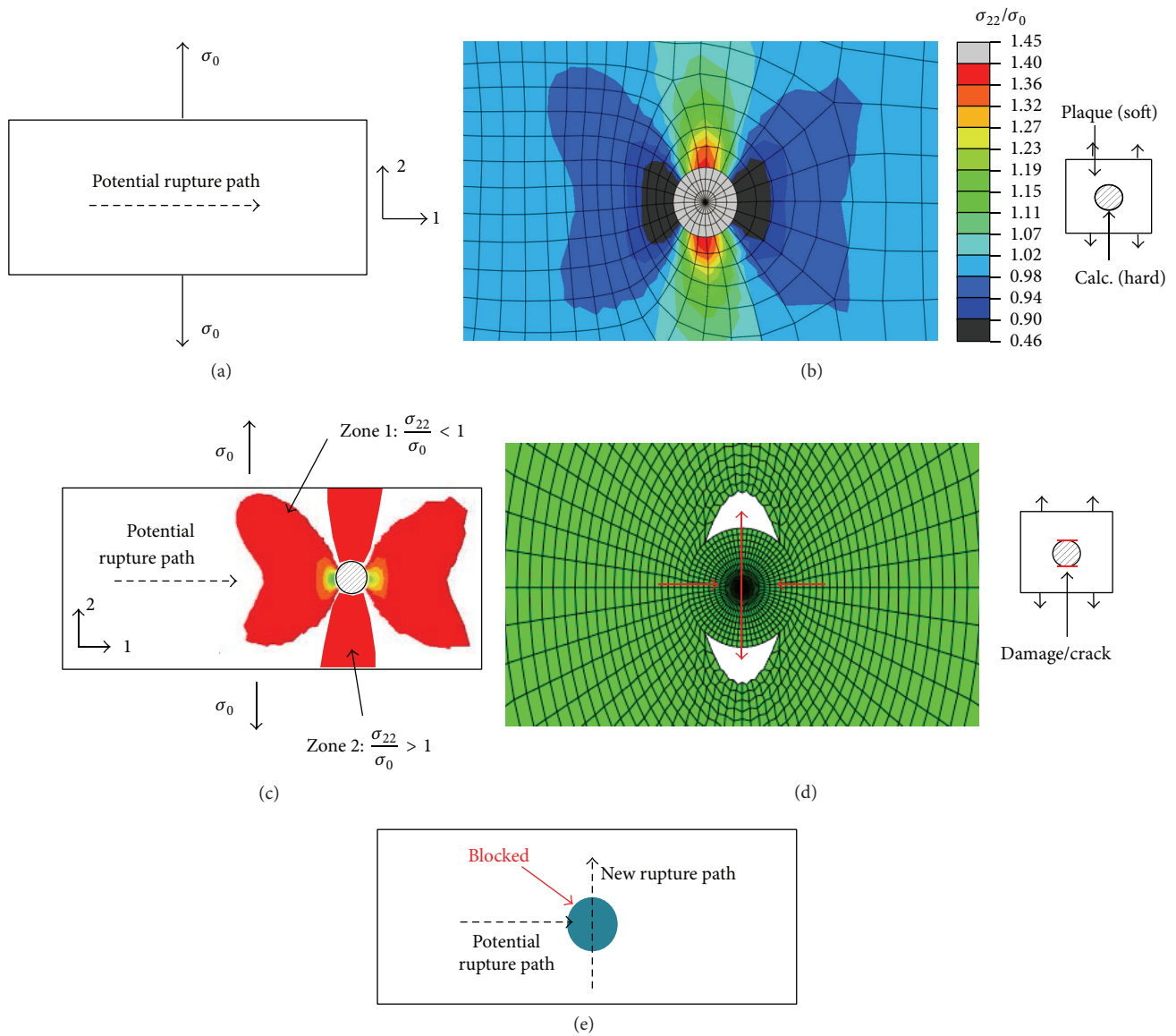


FIGURE 6: Diagram of the possible mechanism of reducing rupture risk.

would not increase the rupture risk, ignoring the calcification is acceptable. At least it will not lead to an underestimated risk.

Conflict of Interests

The authors declare that there is no conflict of interests regarding the publication of this paper.

Authors' Contribution

Baijian Wu and Xuan Pei contributed equally to this work.

Acknowledgments

This study was partially supported by the National 973 Basic Research Program of China (no. 2013CB733803) and the National Natural Science Foundation of China (NSFC) (no. 11272091).

References

[1] T. S. Hatsukami, R. Ross, N. L. Polissar, and C. Yuan, "Visualization of fibrous cap thickness and rupture in human atherosclerotic carotid plaque *in vivo* with high-resolution magnetic resonance imaging," *Circulation*, vol. 102, no. 9, pp. 959-964, 2000.

- [2] G. Finet, J. Ohayon, and G. Rioufol, "Biomechanical interaction between cap thickness, lipid core composition and blood pressure in vulnerable coronary plaque: impact on stability or instability," *Coronary Artery Disease*, vol. 15, no. 1, pp. 13–20, 2004.
- [3] H. C. Stary, "Natural history of calcium deposits in atherosclerosis progression and regression," *Zeitschrift fur Kardiologie*, vol. 89, supplement 2, pp. 28–35, 2000.
- [4] P. Raggi, A. Boulay, S. Chasan-Taber et al., "Cardiac calcification in adult hemodialysis patients: a link between end-stage renal disease and cardiovascular disease?" *Journal of the American College of Cardiology*, vol. 39, no. 4, pp. 695–701, 2002.
- [5] Y. Arad, K. J. Goodman, M. Roth, D. Newstein, and A. D. Guerci, "Coronary calcification, coronary disease risk factors, C-reactive protein, and atherosclerotic cardiovascular disease events: the St. Francis heart study," *Journal of the American College of Cardiology*, vol. 46, no. 1, pp. 158–165, 2005.
- [6] J. C. M. Witteman, W. B. Kannel, P. A. Wolf et al., "Aortic calcified plaques and cardiovascular disease (the Framingham study)," *American Journal of Cardiology*, vol. 66, no. 15, pp. 1060–1064, 1990.
- [7] F. Folsom, R. A. Kronmal, R. C. Detrano et al., "Coronary artery calcification compared with carotid intima-media thickness in the prediction of cardiovascular disease incidence: the multi-ethnic study of atherosclerosis (MESA)," *Archives of Internal Medicine*, vol. 108, no. 12, pp. 1333–1339, 2008.
- [8] Y. Vengrenyuk, S. Carlier, S. Xanthos et al., "A hypothesis for vulnerable plaque rupture due to stress-induced debonding around cellular microcalcifications in thin fibrous caps," *Proceedings of the National Academy of Sciences of the United States of America*, vol. 103, no. 40, pp. 14678–14683, 2006.
- [9] M. Relucanti, R. Heyn, L. Petruzzello, G. Pugliese, M. Taurino, and G. Familiari, "Detecting microcalcifications in atherosclerotic plaques by a simple trichromic staining method for epoxy embedded carotid endarterectomies," *European Journal of Histochemistry*, vol. 54, no. 3, article e33, 2010.
- [10] J. F. Wenk, P. Papadopoulos, and T. I. Zohdi, "Numerical modeling of stress in stenotic arteries with microcalcifications: a micromechanical approximation," *Journal of Biomechanical Engineering*, vol. 132, no. 9, Article ID 091011, 2010.
- [11] N. Maldonado, A. Kelly-Arnold, Y. Vengrenyuk et al., "A mechanistic analysis of the role of microcalcifications in atherosclerotic plaque stability: potential implications for plaque rupture," *The American Journal of Physiology—Heart and Circulatory Physiology*, vol. 303, no. 5, pp. H619–H628, 2012.
- [12] S. H. Rambhia, X. Liang, M. Xenos et al., "Microcalcifications increase coronary vulnerable plaque rupture potential: a patient-based micro-CT fluid-structure interaction study," *Annals of Biomedical Engineering*, vol. 40, no. 7, pp. 1443–1454, 2012.
- [13] W. Chen and V. Dilsizian, "Targeted PET/CT imaging of vulnerable atherosclerotic plaques: microcalcification with sodium fluoride and inflammation with fluorodeoxyglucose," *Current Cardiology Reports*, vol. 15, no. 6, article 364, 2013.
- [14] S. Kimura, T. Kakuta, T. Yonetsu et al., "Clinical significance of echo signal attenuation on intravascular ultrasound in patients with coronary artery disease," *Circulation: Cardiovascular Interventions*, vol. 2, no. 5, pp. 444–454, 2009.
- [15] H. Huang, R. Virmani, H. Younis, A. P. Burke, R. D. Kamm, and R. T. Lee, "The impact of calcification on the biomechanical stability of atherosclerotic plaques," *Circulation*, vol. 103, no. 8, pp. 1051–1056, 2001.
- [16] G. C. Cheng, H. M. Loree, R. D. Kamm, M. C. Fishbein, and R. T. Lee, "Distribution of circumferential stress in ruptured and stable atherosclerotic lesions: a structural analysis with histopathological correlation," *Circulation*, vol. 87, no. 4, pp. 1179–1187, 1993.
- [17] A. Schmermund and R. Erbel, "Unstable coronary plaque and its relation to coronary calcium," *Circulation*, vol. 104, no. 14, pp. 1682–1687, 2001.
- [18] A. Mauriello, F. Servadei, G. B. Zoccai et al., "Coronary calcification identifies the vulnerable patient rather than the vulnerable plaque," *Atherosclerosis*, vol. 229, no. 1, pp. 124–129, 2013.
- [19] D. M. Hermann, J. Gronewold, N. Lehmann et al., "Coronary artery calcification is an independent stroke predictor in the general population," *Stroke*, vol. 44, no. 4, pp. 1008–1013, 2013.
- [20] J. J. Mulvihill, E. M. Cunnane, S. M. McHugh, E. G. Kavanagh, S. R. Walsh, and M. T. Walsh, "Mechanical, biological and structural characterization of *in vitro* ruptured human carotid plaque tissue," *Acta Biomaterialia*, vol. 9, no. 11, pp. 9027–9035, 2013.
- [21] W. E. Shaalan, H. Cheng, B. Gewertz et al., "Degree of carotid plaque calcification in relation to symptomatic outcome and plaque inflammation," *Journal of Vascular Surgery*, vol. 40, no. 2, pp. 262–269, 2004.
- [22] C. M. Wahlgren, W. Zheng, W. Shaalan, J. Tang, and H. S. Bassiouny, "Human carotid plaque calcification and vulnerability: relationship between degree of plaque calcification, fibrous cap inflammatory gene expression and symptomatology," *Cerebrovascular Diseases*, vol. 27, no. 2, pp. 193–200, 2009.
- [23] A. Kelly-Arnold, N. Maldonado, D. Laudier, E. Aikawa, L. Cardoso, and S. Weinbaum, "Revised microcalcification hypothesis for fibrous cap rupture in human coronary arteries," *Proceedings of the National Academy of Sciences of the United States of America*, vol. 110, no. 26, pp. 10741–10746, 2013.
- [24] D. Bluestein, Y. Alemu, I. Avrahami et al., "Influence of microcalcifications on vulnerable plaque mechanics using FSI modeling," *Journal of Biomechanics*, vol. 41, no. 5, pp. 1111–1118, 2008.
- [25] M. Cilla, D. Monterde, E. Peña, and M. Á. Martínez, "Does microcalcification increase the risk of rupture?" *Proceedings of the Institution of Mechanical Engineers H*, vol. 227, no. 5, pp. 588–599, 2013.
- [26] Y. Vengrenyuk, L. Cardoso, and S. Weinbaum, "Micro-CT based analysis of a new paradigm for vulnerable plaque rupture: cellular microcalcifications in fibrous caps," *MCB Molecular and Cellular Biomechanics*, vol. 5, no. 1, pp. 37–47, 2008.
- [27] A. J. Bank, A. Versluis, S. M. Dodge, and W. H. Douglas, "Atherosclerotic plaque rupture: a fatigue process?" *Medical Hypotheses*, vol. 55, no. 6, pp. 480–484, 2000.
- [28] A. Versluis, A. J. Bank, and W. H. Douglas, "Fatigue and plaque rupture in myocardial infarction," *Journal of Biomechanics*, vol. 39, no. 2, pp. 339–347, 2006.
- [29] W. E. Stehbens, "The fatigue hypothesis of plaque rupture and atherosclerosis," *Medical Hypotheses*, vol. 58, no. 4, pp. 359–360, 2002.
- [30] X. Pei, B. J. Wu, and Z. Y. Li, "Fatigue crack propagation analysis of plaque rupture," *Journal of Biomechanical Engineering*, vol. 135, no. 10, pp. 101003–101009, 2013.
- [31] Y. Huang, Z. Teng, U. Sadat, J. He, M. J. Graves, and J. H. Gillard, "In vivo MRI-based simulation of fatigue process: a possible trigger for human carotid atherosclerotic plaque

- rupture,” *BioMedical Engineering OnLine*, vol. 12, article 36, 2013.
- [32] W. V. Mars and A. Fatemi, “Factors that affect the fatigue life of rubber: a literature survey,” *Rubber Chemistry and Technology*, vol. 77, no. 3, pp. 391–412, 2004.
- [33] F. Erdogan and G. Sih, “On the crack extension in plates under plane loading and transverse shear,” *Journal of Basic Engineering*, vol. 85, no. 4, pp. 519–525, 1963.
- [34] L. Wexler, B. Brundage, J. Crouse et al., “Coronary artery calcification: pathophysiology, epidemiology, imaging methods, and clinical implications. A statement for health professionals from the American heart association,” *Circulation*, vol. 94, no. 5, pp. 1175–1192, 1996.
- [35] Z.-Y. Li, J. U-King-Im, T. Y. Tang, E. Soh, T. C. See, and J. H. Gillard, “Impact of calcification and intraluminal thrombus on the computed wall stresses of abdominal aortic aneurysm,” *Journal of Vascular Surgery*, vol. 47, no. 5, pp. 928–935, 2008.
- [36] Z.-Y. Li, S. Howarth, T. Tang, M. Graves, J. U-King-Im, and J. H. Gillard, “Does calcium deposition play a role in the stability of atheroma? Location may be the key,” *Cerebrovascular Diseases*, vol. 24, no. 5, pp. 452–459, 2007.

Research Article

Drug Release Analysis and Optimization for Drug-Eluting Stents

Hongxia Li,¹ Yihao Zhang,¹ Bao Zhu,² Jinying Wu,¹ and Xicheng Wang¹

¹ State Key Laboratory of Structural Analysis for Industrial Equipment, Department of Engineering Mechanics, Dalian University of Technology, Dalian 116024, China

² Surface Engineering Laboratory, School of Materials Science and Engineering, Dalian University of Technology, Dalian 116024, China

Correspondence should be addressed to Hongxia Li; lihongxia3379@mail.dlut.edu.cn

Received 21 August 2013; Accepted 1 October 2013

Academic Editors: H.-C. Han, Y. Qian, and A. Qiao

Copyright © 2013 Hongxia Li et al. This is an open access article distributed under the Creative Commons Attribution License, which permits unrestricted use, distribution, and reproduction in any medium, provided the original work is properly cited.

The drug release analysis and optimization for drug-eluting stents in the arterial wall are studied, which involves mechanics, fluid dynamics, and mass transfer processes and design optimization. The Finite Element Method (FEM) is used to analyze the process of drug release in the vessels for drug-eluting stents (DES). Kriging surrogate model is used to build an approximate function relationship between the drug distribution and the coating parameters, replacing the expensive FEM reanalysis of drug release for DES in the optimization process. The diffusion coefficients and the coating thickness are selected as design variables. An adaptive optimization approach based on kriging surrogate model is proposed to optimize the lifetime of the drug in artery wall. The adaptive process is implemented by an infilling sampling criterion named Expected Improvement (EI), which is used to balance local and global search and tends to find the global optimal design. The effect of coating diffusivity and thickness on the drug release process for a typical DES is analyzed by means of FEM. An implementation of the optimization method for the drug release is then discussed. The results demonstrate that the optimized design can efficiently improve the efficacy of drug deposition and penetration into the arterial walls.

1. Introduction

Cardiocerebrovascular disease is a serious threat to human health. There are three main treatments for vascular diseases: surgery, coronary angioplasty, and coronary stenting. Coronary stenting is minimally invasive catheter-based interventions. Compared to surgery, the coronary stenting is less invasive, so postoperative recovery is quick. Compared to coronary angioplasty, it can avoid restenosis, efficiently. So coronary stenting has been widely applied to clinical; so far coronary stenting technique has become the most promising treatment for coronary artery diseases; however, the arterial wall damage and restenosis caused by stent have not been completely resolved. This is the main reason that development of stenting is hampered. Fortunately, the coronary stent can carry the drug through drug eluting. The drug-eluting stents (DES) could provide the local high concentration of the drug by local drug delivery system and minimize the systemic side effects. Thereby, the generation of thrombus is suppressed, and the risk of restenosis is reduced

[1]. Therefore, the DES is a revolutionary technology for stenosis disease in the clinical treatment. However, the drug release in the blood and drug concentration gradient in the blood vessels are complex fluid dynamics problems. How to control the drug release in the blood and drug concentration gradient in the blood vessels is a challenging task. So dosing and extending the efficacy period are very important.

A few works about DES were reported, Yang and Burt [1] explored several factors that impact the drug release of DES, such as physiological transport forces, drug physicochemical properties, local biological tissue properties, and stent design. Pontrelli and de Monte [2] proposed a novel computational approach and studied the impact of tissue properties, local hemodynamics, and stent design for the drug release of DES based on a consistent mathematical model. The previous work for DES mainly researched the drug release of DES but did not propose how to extend the efficacy of DES. Drug release process is very complex, and the drug concentration is nonuniform. The relative function of drug concentration and the factors that affect drug release cannot be described

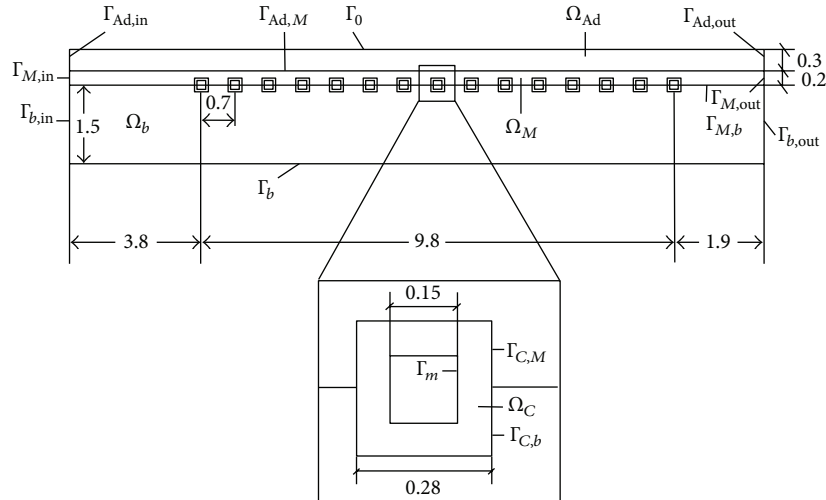


FIGURE 1: 2D simplified model.

by an explicit expression. So it is very difficult to propose how to extend the efficacy of DES. Fortunately, kriging surrogate model can be used to establish the approximate functional relationship between drug concentration and the factor of drug release, effectively. Based on the kriging surrogate model, we can optimize the design of the DES and extend the efficacy of DES easily.

The Finite Element Method (FEM) is here used to analyze the process of drug release in the vessels for DES, in which the microstructure of tissue (anisotropic diffusion of the drug, porosity, and retention of the drug protein) and the macrostructure of tissue (thrombus/blood clots) are considered. Based on the FEM analysis, an optimization approach combined with Expected Improvement (EI) function [3] which is based on kriging surrogate model [4] is used to extend the lifetime of the drug in artery wall. The diffusion coefficients and the coating thickness are selected as design variables. The Latin Hypercube Sampling Method is used to obtain sample points for the initial model established by kriging surrogate model method; EI function is used to balance local and global search and tends to find the global optimal design.

2. Methods

The Finite Element Method (FEM) is used to analyze the process of drug release in the vessels for Drug Eluting Stents (DES). As shown in Figure 1, a simplified axisymmetric model [5] for (DES) is adopted for quantitative analysis, which was proposed to research the drug release of the DES by Mongrain et al. [6]. As the intima and media layers have similar property and the stent is usually embedded in media layer, the arterial wall is modeling with two layers (intima and media layer and adventitia layer).

As shown in Figure 1, Ω_M , Ω_{Ad} , Ω_C , and Ω_b are the intima and media layer, the adventitia layer, the coating, and the blood, respectively. Γ_s is the symmetry axis of the blood, $\Gamma_{b,in}$ is the inflow boundary, $\Gamma_{b,out}$ is the outflow boundary, Γ_m is

the interface of coating and stent, and $\Gamma_{M,in}$ and $\Gamma_{M,out}$ are the artery boundaries of inflow and outflow for intima and media layer, respectively. $\Gamma_{Ad,in}$ and $\Gamma_{Ad,out}$ are the artery boundaries of inflow and outflow for adventitia layer. Γ_0 is the interface of arterial wall and trophoblast tube; $\Gamma_{C,b}$, $\Gamma_{C,M}$, $\Gamma_{M,b}$, and $\Gamma_{Ad,M}$ are the interfaces of blood, artery, and coating, respectively.

At initial time ($t = 0$), the drug was assumed completely dissolved in the coating and the concentration is uniform. The coating is modeled as a homogeneous isotropic porous media, and plasma cannot penetrate the coating. The control equation, boundary condition and initial time in the coating can be found in [5].

The arterial wall is also modeling as porous media. Because the inner and outer walls in the presence of physiological arterial pressure will lead to plasma flow, mass transfer was under diffusion and convection equations [7]. The convection effect is only acting on the drug dissolved in the blood, according to the report by Creel et al. [8], without considering transient absorption effect of the drug in artery, and the drug concentration in artery is $c' = c/k\varepsilon$, in which c is the average drug concentration in arterial tissue and k is the partition coefficient in arterial wall, and ε is the arterial porosity. On the interface of artery and coating, the boundary conditions are the same as reference [5].

The control equation of blood flow is the general convection diffusion equation. The control equation and the boundary condition on the interface of artery and coating can be found in reference [5].

First of all, considering the plasma flow in the arterial wall, the plasma flow velocity in arterial wall, and the pressure difference between inside and outside surfaces determined by the Darcy law, the blood in artery is modeled as incompressible Newtonian Equation. As the drug release in the blood does not affect blood flow, the velocity field can be obtained, and then, with the velocity field as given conditions, the drug concentration distribution at different times can be obtained [5].

The material properties are the same in reference [5]. The blood velocity distribution at the entrance is as parabolic

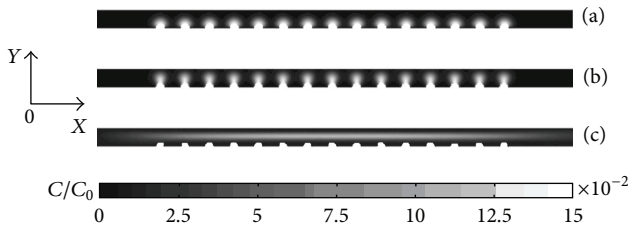


FIGURE 2: Drug concentration of the artery wall with different models. (a) Isotropic nonporous medium, (b) isotropic porous media, and (c) anisotropic porous media.

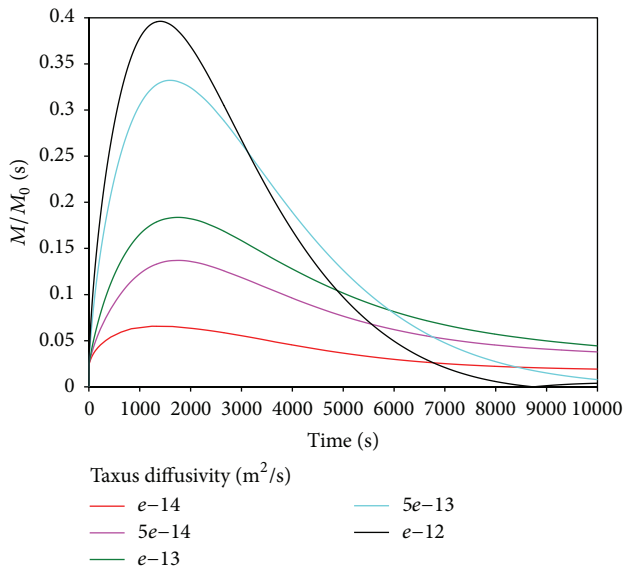


FIGURE 3: Influence of coating diffusivity on drug concentration into the artery wall.

shape. The maximum speed is 14.0 cm/s. The drug diffusion in coating, blood, and adventitia layer is isotropic. The drug diffusion in intima and media layer is anisotropic. The coefficients of control equations are the same as reference [5].

Figure 2 shows the difference between isotropic and anisotropic diffusion coefficients. Drug distribution is more uniform in the x direction for anisotropic diffusion coefficients than isotropic diffusion coefficients because it is easier in the horizontal direction (the axial direction) than the vertical diffusion direction (radial direction) and seepage flow of plasma in porous media. The convection effect of y direction promotes the diffusion of the drug.

Figure 3 shows the drug concentration versus time with different diffusion coefficients in the coating. It is clear that drug concentration reached the peak in arterial wall, and then it decreased. It is reasonable; because drug will diffuse into artery, gradually by the difference of drug concentration in the coating and artery, and due to the elution effect, the drug concentration decreased outside of the artery wall. The elution effect is not significant at initial moment because of the low drug concentration in the artery wall. When the drug reaches certain concentration in artery wall and drug release

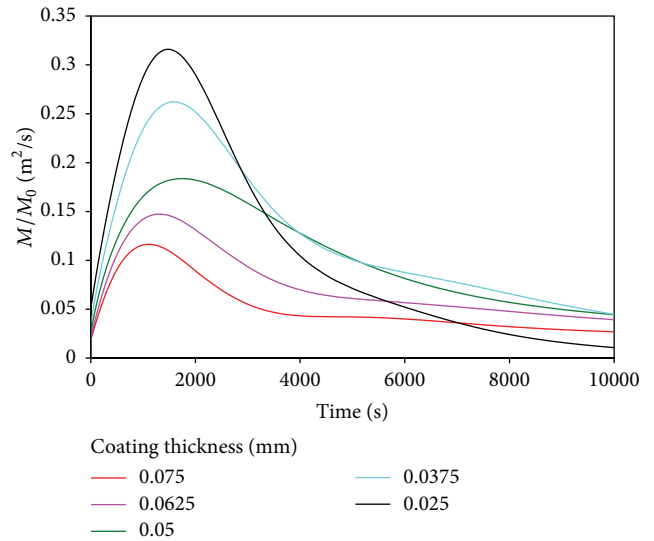


FIGURE 4: Influence of coating thickness on drug concentration into the artery wall.

to a certain degree in coating, the elution effect will be quite significant. As the coating cannot continue to provide drugs continuously, the drug concentration will decrease.

As the diffusion coefficient increases, the drug concentration in the artery wall reaches a higher peak with a faster growth. The decay rate of the peak is not proportional to the diffusion coefficient, so the trend of the change of drug concentration is not linear relationship with diffusion coefficient. This conclusion is important, because if we want a longer time drug concentration in the artery wall, it should not increase or decrease the diffusion coefficients of the coating, simply. Therefore, it appears optimal to find an appropriate diffusion coefficient to make the longest time with certain drug concentration. That provides a theoretical basis for DES coating optimization.

Figure 4 shows drug concentration versus time with different thicknesses of coating in the artery wall. It is clear that drug concentration reached the peak in arterial wall, and then it decreased. It is because drug will diffuse into artery, gradually by the difference of drug concentration in the coating and artery, due to the elution effect, the drug concentration decreased outside of the artery wall. The elution effect is not significant at initial moment because of the low drug concentration in the artery wall. When the drug reaches certain concentration in artery wall and drug release a certain degree in coating, the elution effect will be quite significant. As the coating cannot continue to provide drugs continuously, the drug concentration will decrease.

The initial concentration of drugs in the coating shifted to a higher level with the decrease of the coating thickness. It is clear that the drug concentration in the artery wall reaches a higher peak with a faster growth. The duration of the drug in the artery wall is not inversely proportional to the coating thickness. So the trend of the change of drug concentration is not linear relationship with the coating thickness. Therefore, it appears optimal to find an appropriate coating thickness.

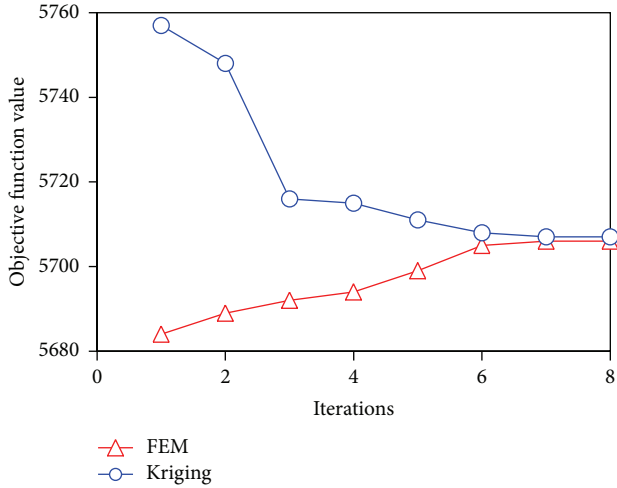


FIGURE 5: Iterative optimized process.

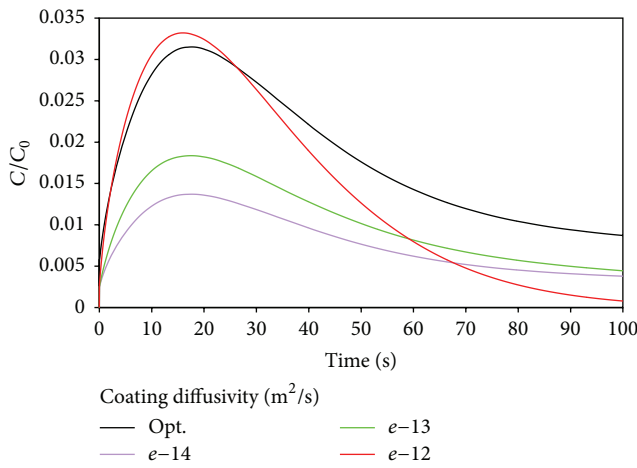


FIGURE 6: Influence of coating diffusivity on drug concentration into the artery wall.

The two important factors for the distribution of drugs in artery wall are diffusion coefficients and the coating thickness. Therefore, diffusion coefficients and the coating thickness can be chosen as the design variables. An optimization approach based on kriging surrogate model is used to optimize the lifetime of the drug in artery wall. The kriging model was used to build an approximate function relationship between the objective function and design variables (the diffusion coefficients in coating and the thickness of coating), thereby replacing the expensive FEM reanalysis of the objective function value during the optimization. The optimization iterations are based on the approximate relationship for reducing the high computational cost. An adaptive optimization method based on the kriging surrogate model with Latin Hypercube Sampling (LHS) strategy [9] was used to improve the effect of the drug release of DES. The adaptive process was implemented by the EI function [10], which can balance local and global searches and tends to find the global optimal design. The FEM was used to analyze the drug release of DES in stented artery.

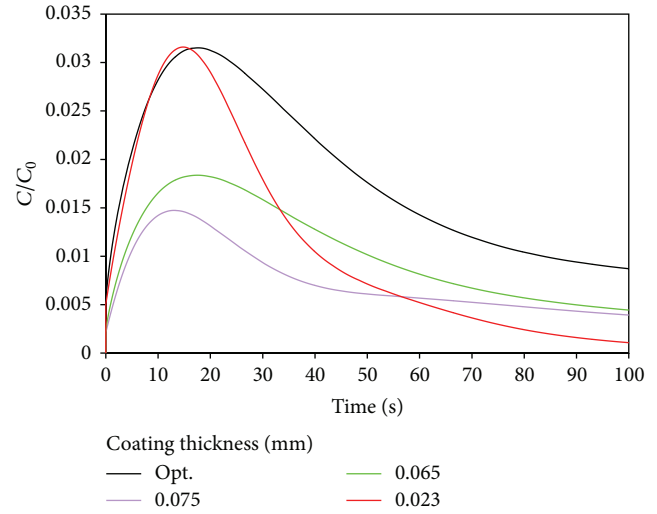


FIGURE 7: Influence of coating thickness on drug concentration into the artery wall.

The evaluation standard of effect of the drug release on the stent is Mean Residence Time (MRT) [2]: the equation is as follows

$$MRT_n = \max \left\{ t \mid \iiint_{\text{wall}} c_{\text{wall}}(x, y, z, t) dx dy dz \geq \frac{n}{100} \iiint_{\text{polymer}} c_0(x, y, z, 0) dx dy dz \right\}. \quad (1)$$

MRT is an important indicator for judging the effect of the drug-eluting stent. In this paper, MRT_{10} is the objective function, assuming that the initial drug concentration is constant in the coating. The diffusion coefficients in the artery wall are constant, and the shape of the stent remains unchanged. For the range of design variables, the range of the diffusion coefficients is $10^{-12} \text{ m}^2/\text{s} \sim 10^{-14} \text{ m}^2/\text{s}$; range of the coating thickness is $0.023 \text{ mm} \sim 0.075 \text{ mm}$. The sample points and the corresponding response are listed in Table 1.

3. Results and Discussion

As shown in Figure 5, the optimization results have fast convergence. The study indicates that when the diffusion coefficient equals $2.5 \times 10^{-13} \text{ m}^2/\text{s}$ and the coating thickness equals 0.05 mm , the drug duration time reaches its maximum under MRT_{10} .

Another judge standard is the ratio of mean concentration and initial concentration in the media layer. So the objective function is selected as the drug duration time when $C_m/C_0 \geq 1\%$, and the design variables are also diffusion coefficients and the coating thickness. As shown in Figures 6 and 7, the optimized objective function reached 85 h, and the drug duration time is increased by 41 h compared to initial design. The optimal diffusion coefficient is $3.2 \times 10^{-13} \text{ m}^2/\text{s}$, and optimal coating thickness is 0.05 mm . It will release the drug into arterial wall faster by increasing the diffusion

TABLE 1: Samples and responses.

Samples	Taxus diffusivity (m ² /s)	Coating thickness (mm)	Response (s)
1	4.82 * 10 ⁻¹³	0.057	4238
2	1.07 * 10 ⁻¹³	0.052	3658
3	9.45 * 10 ⁻¹³	0.073	3670
4	8.68 * 10 ⁻¹³	0.042	3416
5	1.53 * 10 ⁻¹³	0.065	2928
6	8.80 * 10 ⁻¹³	0.031	3078
7	3.84 * 10 ⁻¹³	0.027	3940
8	6.55 * 10 ⁻¹³	0.059	4104
9	8.07 * 10 ⁻¹³	0.072	3782
10	7.44 * 10 ⁻¹³	0.032	3112
11	6.84 * 10 ⁻¹³	0.065	3862
12	5.55 * 10 ⁻¹³	0.046	4604
13	2.37 * 10 ⁻¹³	0.038	4862
14	5.87 * 10 ⁻¹³	0.041	3984
15	3.54 * 10 ⁻¹³	0.062	4120

coefficient and reducing the coating thickness. However, when the drug concentration is too high, concentration difference will lead to lower drug diffusion. At the same time, the drug will diffuse into the outer layer because of the effect of convection caused by the seepage flow in arterial wall. This is the reason why the concentration decreased rapidly from the peak. So our results are reasonable.

4. Conclusions

This paper studies the relationship between the properties of the coating and the drug distribution in the arterial wall. The study indicates that diffusion coefficients and the coating thickness are two important factors of the distribution of drugs in artery wall. An optimization approach based on kriging surrogate model is used to optimize the lifetime of the drug in artery wall. The diffusion coefficients and the coating thickness are selected as design variables. The results demonstrate that the optimized design can efficiently control the release of drug in the blood and drug concentration gradient in the blood vessels.

Conflict of Interests

The authors declare that there is no conflict of interests regarding the publication of this paper.

Acknowledgment

The authors gratefully acknowledge financial support for this work from the National Natural Science Foundation of China (no. 11072048).

References

- [1] C. Yang and H. M. Burt, "Drug-eluting stents: factors governing local pharmacokinetics," *Advanced Drug Delivery Reviews*, vol. 58, no. 3, pp. 402–411, 2006.
- [2] G. Pontrelli and F. de Monte, "Modeling of mass dynamics in arterial drug-eluting stents," *Journal of Porous Media*, vol. 12, no. 1, pp. 19–28, 2009.
- [3] S. N. Lophaven, H. B. Nielsen, and J. Søndergaard, "DACE—a Matlab Kriging toolbox; version 2; informatics and mathematical modelling," Tech. Rep. IMM-TR-2002-12, Technical University of Denmark, Kongens Lyngby, Denmark, 2002.
- [4] D. R. Jones, M. Schonlau, and W. J. Welch, "Efficient global optimization of expensive black-box functions," *Journal of Global Optimization*, vol. 13, no. 4, pp. 455–492, 1998.
- [5] G. Vairo, M. Cioffi, R. Cottone, G. Dubini, and F. Migliavacca, "Drug release from coronary eluting stents: a multidomain approach," *Journal of Biomechanics*, vol. 43, no. 8, pp. 1580–1589, 2010.
- [6] R. Mongrain, I. Faik, R. L. Leask, J. Rodés-Cabau, É. Larose, and O. F. Bertrand, "Effects of diffusion coefficients and struts apposition using numerical simulations for drug eluting coronary stents," *Journal of Biomechanical Engineering*, vol. 129, no. 5, pp. 733–742, 2007.
- [7] J. M. Weiler, E. M. Sparrow, and R. Ramazani, "Mass transfer by advection and diffusion from a drug-eluting stent," *International Journal of Heat and Mass Transfer*, vol. 55, no. 1–3, pp. 1–7, 2012.
- [8] C. J. Creel, M. A. Lovich, and E. R. Edelman, "Arterial paclitaxel distribution and deposition," *Circulation Research*, vol. 86, no. 8, pp. 879–884, 2000.
- [9] H. Li and X. Wang, "Design optimization of balloon-expandable coronary stent," *Structural and Multidisciplinary Optimization*, vol. 48, no. 4, pp. 837–847, 2013.
- [10] D. Jones, M. Schonlau, and w. Welch, "Efficient global optimization of expensive black-box functions," *Journal of Global Optimization*, vol. 13, pp. 445–492, 1998.

Research Article

Blood Clot Simulation Model by Using the Bond-Graph Technique

Gregorio Romero, M. Luisa Martinez, Joaquin Maroto, and Jesus Felez

CITEE, Universidad Politecnica de Madrid, C. Jose Gutierrez Abascal 2, 28006 Madrid, Spain

Correspondence should be addressed to Gregorio Romero; gregorio.romero@upm.es

Received 2 August 2013; Accepted 19 September 2013

Academic Editors: H.-C. Han, M. Ohta, and A. Qiao

Copyright © 2013 Gregorio Romero et al. This is an open access article distributed under the Creative Commons Attribution License, which permits unrestricted use, distribution, and reproduction in any medium, provided the original work is properly cited.

The World Health Organization estimates that 17 million people die of cardiovascular disease, particularly heart attacks and strokes, every year. Most strokes are caused by a blood clot that occludes an artery in the cerebral circulation and the process concerning the removal of this obstruction involves catheterisation. The fundamental object of the presented study consists in determining and optimizing the necessary simulation model corresponding with the blood clot zone to be implemented jointly with other Mechanical Thrombectomy Device simulation models, which have become more widely used during the last decade. To do so, a multidomain technique is used to better explain the different aspects of the attachment to the artery wall and between the existing platelets, it being possible to obtain the mathematical equations that define the full model. For a better understanding, a consecutive approximation to the definitive model will be presented, analyzing the different problems found during the study. The final presented model considers an elastic characterization of the blood clot composition and the possibility of obtaining a consecutive detachment process from the artery wall. In conclusion, the presented model contains the necessary behaviour laws to be implemented in future blood clot simulation models.

1. Introduction

The World Health Organization reports that 15 million people worldwide suffer strokes [1] and of these, 5 million die and further 5 million are left permanently disabled, many severely impaired. Cardiovascular diseases (CVDs) are the primary cause of death globally. It is estimated that more than 15 million people died from this cause in 2004, which represents a very important percentage of all global deaths; this amounts to an estimated 5.5 million deaths due to stroke. In the United Kingdom alone there are 130,000 strokes each year and of the patients that survive many are left with severe disabilities. Strokes are devastating events, 85% of which are caused by the blockage of an artery that prevents blood from flowing to the brain.

Atheromatous plaques are a common cause associated with the narrowing or blockage of an artery. These plaques arise from a build-up of fatty deposits on the inner walls of the blood vessels. This results in the formation of an atheromatous plaque that narrows the artery that it is located in. Parts of the plaque may break away and travel to the brain blocking

a vessel or blood clots that arise from the alteration of blood flow dynamics associated with the narrowing of the vessel can cause a stroke. Generally speaking, changes in blood flow may arise due to a change in the composition of the blood or a change in the blood flow itself (e.g., due to an uneven surface within the vessel wall) such as would be created by plaque formation. Such a change in blood flow predisposes to clot formation. Blood clots arise when platelets adhere to each other and to the artery wall. A clot may therefore readily form at a site where a vessel is narrowed.

Although thrombolytic agents such as alteplase are used to dissolve blood clots that arise in the cerebral arteries of the brain, there are limitations to the use of such thrombolytic agents. During the last decade Mechanical Thrombectomy Devices (MTDs) have become more widely used as an alternative means for clot removal. A number of devices using a variety of methods to remove the clot are now available. These include the MERCI clot retriever, and, more recently, the penumbral device; other types of devices include angiography catheters, rheolytic catheters (Angiojet), Basket style devices, and microsnaaring devices. Thrombectomy may be associated

with risks, such as breakage of moving parts, penetration of the arterial wall, and downstream embolisation caused by clot dislodgment [2]. Studies suggest that mechanical embolectomy is most effective in large volume proximal occlusions [3]. Other interventional surgical treatments include endarterectomy, which involves surgically removing clots in the carotid arteries. This treatment has proved successful [4] but carries a risk of the clot becoming dislodged during the procedure.

New designs of Thrombectomy Devices to remove blood clots without the need to make contact with the clot itself, thereby potentially reducing the risk of problems such as downstream embolisation, for example, by using aspiration techniques, need to be studied and analyzed in order to obtain better results. The analysis, design, and optimization of one experimental device recently developed in the UK, called the “GP” Thrombus Aspiration Device (GPTAD) [5–10], has been recently done by using different simulation techniques [11, 12].

During the development of potential new medical devices computer premodelling may be required to help in the optimization and fine-tuning of the devices. The main objective of this simulation model is to obtain the characterization of a blood clot model considering the interaction between the blood clot and artery wall and the behaviour laws.

Next, the model used for the simulation is consecutively described as well as the phenomena considered, and, in addition, the values of the parameters used are defined.

2. Initial Blood Clot Approximation

Accurately defining the clot model in order to correctly simulate a full aspiration thrombectomy device interaction is the most complex part of the model. A clot is a cylindrically shaped element of 1.0–5.0 cm long, and a mass that falls between 0.5 and 2.0 gram. This element has usually formed in another location, usually in a vascular artery, and has become dislodged remaining trapped in smaller diameter arteries, such as the cerebral artery considered in this work. Therefore, due to this difference in diameter, the clot becomes attached to the wall by a force that needs to be overcome in order to begin its movement for removal. In addition, the relative movement between the clot and the artery presents static and dynamic friction, which needs to be taken into account. If a correct approximation to reality is to be achieved all these phenomena, as well as the circumstances restricting clot movement, need to be considered.

As already stated, the phenomenon preventing clot movement is the difference in diameter between the clot and the artery where it is located. Experimental data [5] and numerical studies [13] indicate that the clot begins its movement when this force is equal to 0.01 N. In order to decide when to begin the movement of the obstructive element, firstly we need to insert a spring into the model to measure the force supported by the beginning of the clot and its deformation. To obtain the value of this spring the phenomenon of surface tension must be taken into account, since it is this that joins the clot to the artery. This surface tension “ γ ” comes about

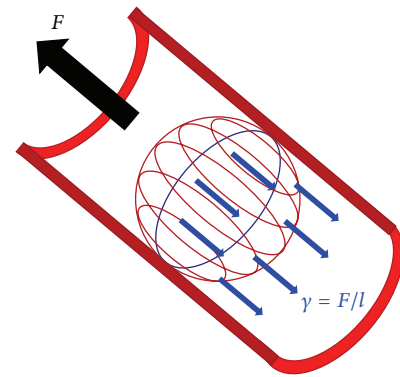


FIGURE 1: Surface tension (blue circle).

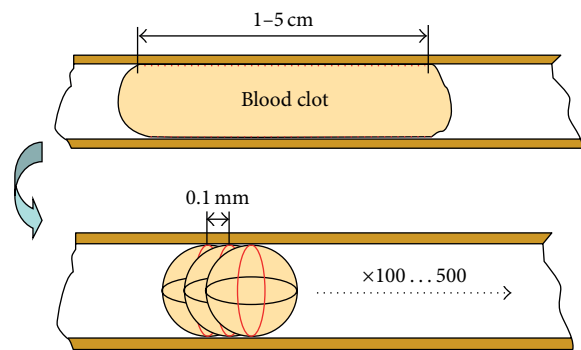


FIGURE 2: Surface tension from some spheres.

from the attraction forces between molecules and is defined as force by unit length:

$$\gamma = \frac{F}{l} \tag{1}$$

If we take the sphere shown in Figure 1, the surface tension would act on the circumference of the contact between the clot and the artery (marked with a blue ellipse).

Bearing in mind the above, if we take into account the value of the length of contact “ l ” from the radius “ r ” of the artery, the value for the surface tension “ γ ” can be obtained and, in turn, the value for the spring coefficient “ K ”, as

$$K = \gamma = \frac{F}{l} \tag{2}$$

As stated above, the clot is 1.0–5.0 cm long, which means it can be broken down into the union of several spheres (Figure 2), all with the same constant. Since over the whole surface of the clot there are adhesion forces, to obtain a correct approximation it is necessary to consider the existence of a sphere for every 0.1 mm. This means that between 100 and 500 spheres would need to be included in the model. On the other hand, since the clot behaves like a rigid body, the fact that all the spheres are located in parallel must be taken into account, so that until the resultant adhesion force is overcome in all of the spheres, the clot will not begin to move.

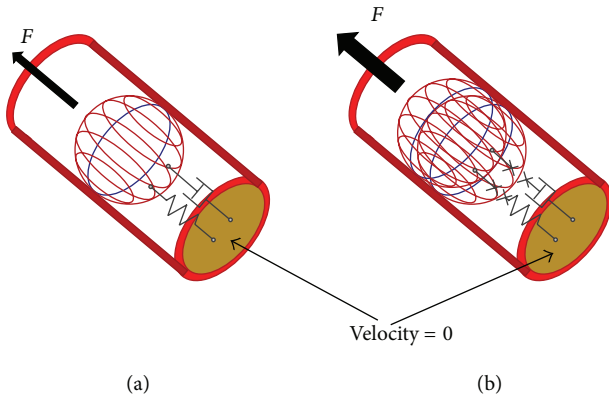


FIGURE 3: Spring-damper system. (a) $F < 0.01$ N. (b) $F \geq 0.01$ N.

Therefore, since all the individual springs are equal, the equivalent spring value “ K_{eq} ” for a determined clot length can be obtained considering the following expression

$$K_{eq} = \frac{K}{n}, \quad (3)$$

where “ K ” is the spring coefficient determined in (2) as the surface tension and “ n ” is the number of elements considered taking into account the existence of one sphere for every 0.1 mm length.

To know when the force will be reached in this equivalent spring and, therefore, when the clot movement will begin, it is essential to calculate the displacement of the spring when it is subjected to 0.01 N through a typical spring equation. Therefore, only when the spring undergoes this displacement should the clot be allowed to move; to the contrary it would be prevented:

$$x = \frac{F}{K_{eq}}. \quad (4)$$

Secondly, it is necessary to insert the resistance that represents the friction between the clot and the arterial wall. The value of this parameter must be variable depending on whether the clot has not begun its movement (static friction) or if it is already in movement (dynamic friction), so that when the clot begins to move the friction value will drop considerably (Figure 3). This value is obtained starting from the Stokes equation and can be given a value of $2.5 \cdot 10^{-6}$ N·s/m for the static friction and an order of magnitude lower than for the dynamic friction.

The transition between both values marks the beginning or end of the clot movement by means of the displacement of the spring representing the deformation described in expression (4). So, when the displacement undergone by this spring is less than that calculated, static friction will rule; to the contrary, if it is greater, the friction will be dynamic.

In addition to the spring and the resistance inserted, the model must have an inertance that represents the mass of the blood clot (0.5–2.0 gram):

$$I = m. \quad (5)$$

Finally, to ensure that the clot remains at rest while the force existing at its beginning is less than 0.01 N, a spring-damper system joined to a wall (zero flow source) must be used.

In this system, while the clot does not receive the force of minimum suction, it has a zero speed. However, when it begins its movement, the spring-damper system must be cancelled allowing its extraction. While the force representing the deformation of the clot is lower than 0.01 N, it will remain attached to the wall, thereby preventing any movement. To the contrary, if the force exceeds this figure the model will cause the bond imposed by the spring-damper system to be eliminated with the clot becoming free and moving in accordance with the suction pressure acting on it from the system, letting it be removed.

Therefore, the elimination of the spring-damper system will be performed from the displacement of the spring representing the clot deformation as was seen in the condition imposed on the static/dynamic friction. The initial values for the spring-damper system have been considered, $1 \cdot 10^{10}$ N/m and $1 \cdot 10^9$ N·s/m, respectively; these values have been taken to consider a very rigid union and the correct convergence of the system.

Figure 4 shows the Bond-Graph scheme of the different elements commented below, having indicated where the aspiration force created by the Aspiration Thrombectomy Device (ATD) would be added.

The main problem of this initial model is that the blood clot is fully considered as a simple element, while the possibility of partial disaggregation does not exist. In addition, this model is able to simulate the behaviour of the blood clot attachment but the values of the necessary compliances and resistances introduced can only be estimated from different experiments. The value of the constants in both the spring and the damper must be extremely high to simulate a firm anchor to the point of release. Simulating the moment when the clot breaks loose from the wall in the previous model method was very difficult, because the junction to the wall had to allow clot movement according to pressure, even if such pressure was not enough to move it in totality. In addition, low value changes introduced in these elements can modify substantially the pressure and time results.

The previous comments are the main reason why a better approximation model concerning the blood clot and artery wall attachment needs to be studied.

3. Extended Blood Clot Approximation

For a correct understanding of the blood clot detachment process (see Figure 5), it is necessary to take into account that the friction between the clot and the arterial wall creates a resistance factor, not over all the surface, but incrementally from the beginning to the end.

By considering this, it is possible to understand that the value of this parameter must be variable across the length depending on whether the clot has begun its movement (Figure 5(a)) or before it has begun to move (Figures 5(a) and 5(b)) during the clot extraction procedure. To do this,

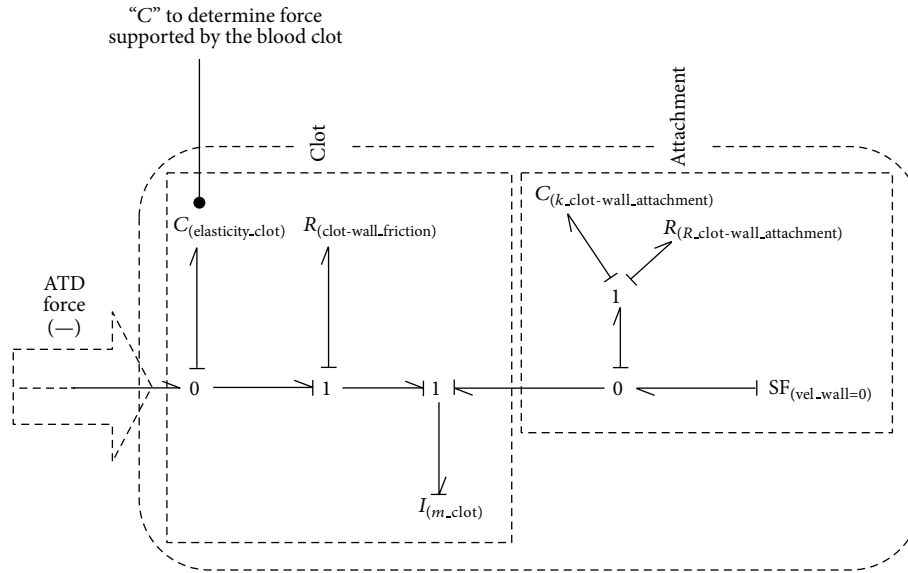


FIGURE 4: The simplest blood clot model by Bond-Graph technique.

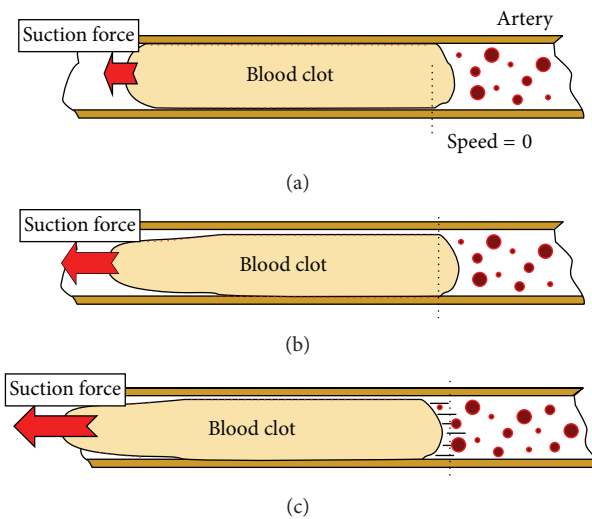


FIGURE 5: Influence of the suction force over blood clot. (a) The lowest value; no movement. (b) Medium value; beginning of the front part movement. (c) Higher value; blood clot movement.

an extended blood clot will incorporate different inertia elements representing different partitions of the blood clot, joined by different spring-damper systems (designed by K_{union} and R_{union} , resp.) between them to simulate the elastic and plastic behaviour of the clot, and the consequent spring-damper systems joined to the wall, which could be defined by a zero flow source.

When the clot begins to move the friction decreases considerably. In the same way as previously, this value is obtained from the Stokes equation and can be given a value of $2.5 \cdot 10^{-6}$ N-s/m for the static friction and an order of magnitude lower than for the dynamic friction; the transition between both values marks the beginning or end of the clot movement.

The existence of the different partitions (Figures 5 and 6), and the consequent spring-damper systems joined to the wall, let the model acquire a more realistic behaviour due to the fact that the different inertias detachment can be treated individually.

3.1. Platelet Composition Model. Although the extended clot approximation is necessary, due to the problems presented in the previous model, it is necessary to look for another solution to simulate the clot and its behaviour under a negative force. As we have seen before, we kept the partitions represented by inertia and joined by the spring-damper system (R_{union} , K_{union}) to simulate the elastic and plastic behaviour of the clot (Figure 7).

Nevertheless, to model the junction with the artery, the point of release, and the static and dynamic friction, we decided to add to each inertia an effort source that varies depending on the moment of the simulation. We can observe the new configuration in Figure 8. In this figure, it is possible to observe that each inertia will suffer a force due to suction, which should be compensated in the model with a force of friction to annul it while the clot is in the position of static friction. Once we have calculated the flow-effort table of the system, we apply the condition that the stress on the inertia must be zero.

The effort source, as we have stated before, varies; that is, when the clot begins its movement, the static friction disappears and the dynamic friction acts on the system, which is lower than the previous one. We have calculated it by means of the Stokes law for a cylindrical solid (see (7)):

$$F_{dynamic_friction} = \frac{C}{8} \cdot \rho \cdot \pi \cdot D^2 \cdot V^2, \quad (6)$$

where “C” is the form coefficient for a cylinder, “ ρ ” is the blood density, “D” the clot diameter, and “V” the velocity of the first partition.

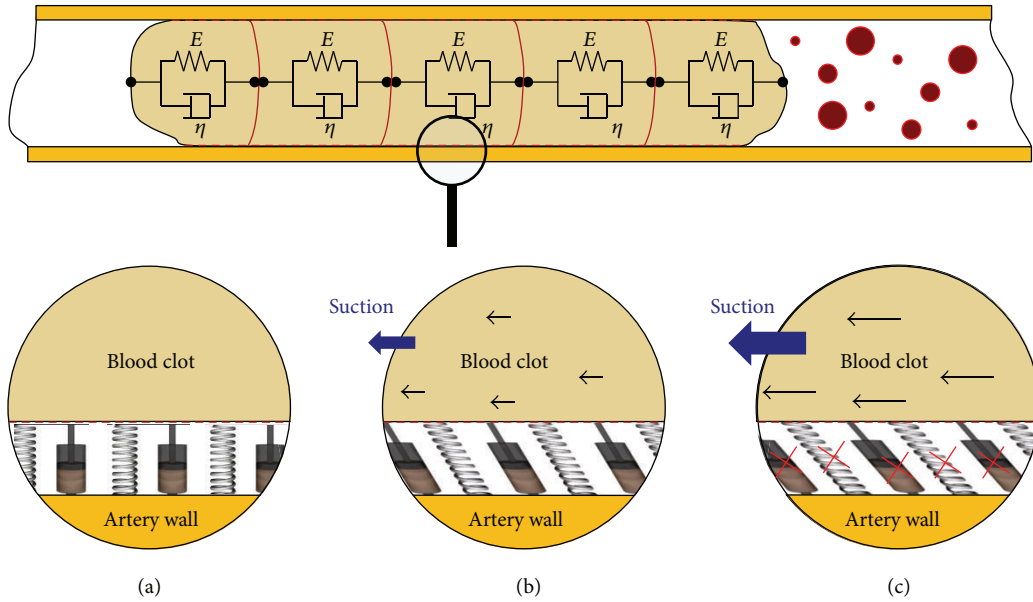


FIGURE 6: Artery wall adherence based on individual spring-damper systems. (a) No force. (b) Suction force lower than adherence force. (c) Suction force higher than adherence force.

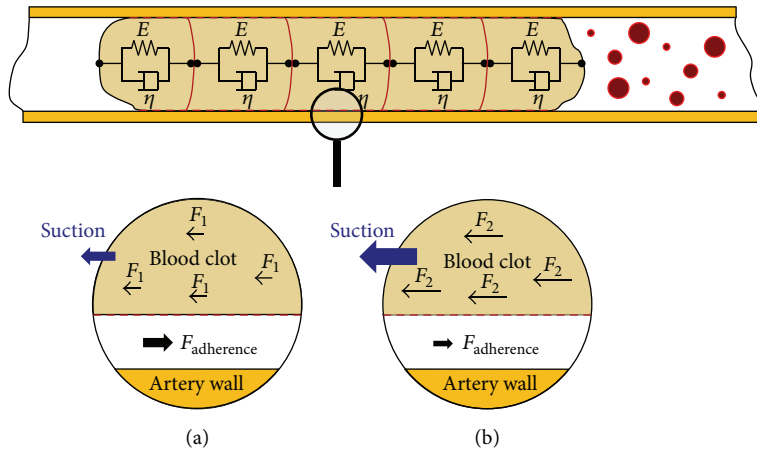


FIGURE 7: Adherence and friction based on effort source. (a) Lower suction force; no movement. (b) Suction force higher than adherence force.

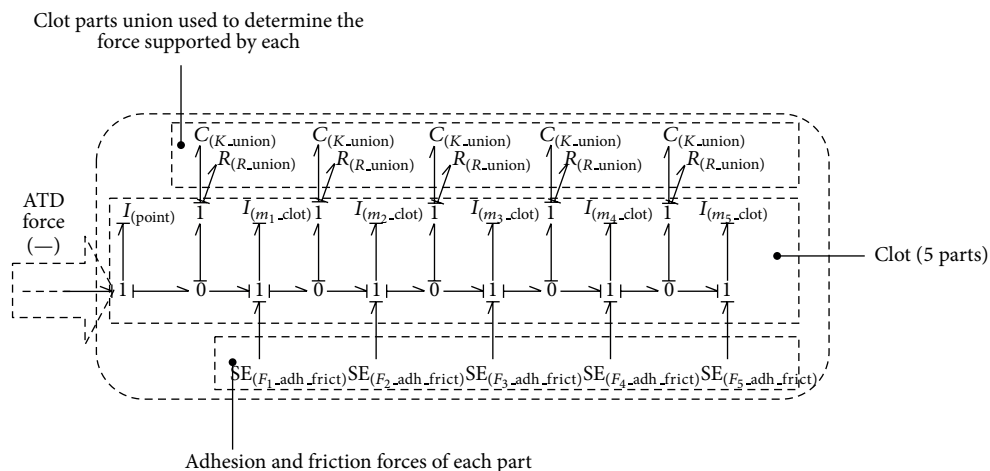


FIGURE 8: The simplest blood clot model by Bond-Graph technique.

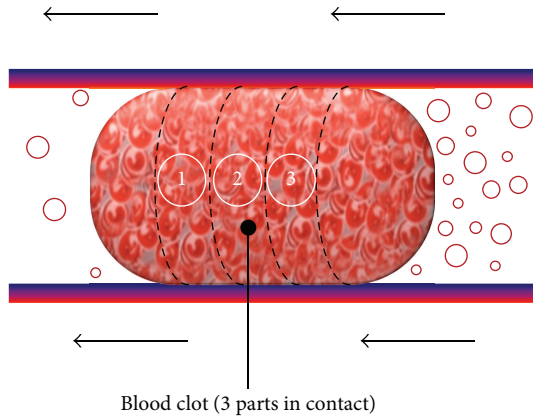


FIGURE 9: Blood clot 3 parts division.

The condition to determine if the clot is attached to the surface is based on the force that the spring suffers between partitions (K_{union}). Hence when $K_{\text{union}} \cdot \text{Displacement}(K_{\text{union}})$ is higher than the adherence force, the clot releases from the surface.

The value of the adherence force has been analyzed by Flannery [14] and we made use of all the necessary data from that. To calculate the adhesion strength Flannery divided the blood clot into some parts; this geometry is only valid for the condition of static friction, because, once the clot releases, it recovers a part of its form and again becomes like a cylinder. So, we assumed this model and we divided this clot into 3 parts (Figure 9).

As we have defined our clot, we then calculate the adhesion force by means of the platelet adhesion force; we have obtained from Flannery the equivalent number of platelets per area equation:

$$\text{No. platelets per area} = fp \cdot \frac{SA}{MPA}, \quad (7)$$

where “ fp ” is the % of platelets in the clot, “ MPA ” the mean platelet area, and “ SA ” is the area of the surface in contact with the artery, which can be obtained from the clot length, the number of partitions (3 in the case shown), and the artery diameter.

Once we have obtained the number of platelets in contact with the artery and the force platelet-artery wall, we can calculate the adhesion force of each partition and obviously of the entire clot:

$$F_{\text{adh}} = \text{No. platelets}_{\text{TOTAL}} \cdot F_{\text{platelet-artery_wall}} \quad (8)$$

In this way, we would have different adhesion forces depending on the form and size of the clot, and we can reference those to the artery diameter and the percentage of occlusion.

3.2. Atheroma Plaque Implementation. In pathology, an atheroma is an accumulation and swelling in artery walls that is made up of (mostly) macrophage cells, or debris that contain lipids (cholesterol and fatty acids), calcium, and a variable amount of fibrous connective tissue (Figure 10).

This accumulation modifies the geometry of the blood as Figure 11 shows and the clot can be considered as a cylindrical clot that narrows down the middle due to stenosis or an atherosclerotic plaque. We decided to make the partitions shown because each one has the same contact area with the artery and the same volume, in order to simplify the calculation of the adhesion force and the mass of each partition. To be more coherent, when the blood clot begins movement each section should be readapted and the mass and contact area recalculated according to Figure 11.

The implementation of the final blood clot model required for the simulation has been made by connecting the five partitions shown in this section and considering the different adhesion and friction forces, jointly with the platelet-platelet forces, which are represented by the K_{union} and R_{union} elements; this is shown in Figure 9.

3.3. Systolic and Diastolic Blood Pressure. For a correct implementation of the blood clot model, it is necessary to implement the systolic and diastolic blood pressure as results of the cardiovascular system.

One of the options that has been simulated jointly with the presented model has been that corresponding to the existing analog circuit developed by Noordergraaf at 1978 [15] for the human systemic circulatory system (Figure 12).

Although the simulation of the previous circuit by using Bond-Graph technique is extremely easy, the drawback found was that associated with the diode simulation, since it was observed that, depending on the algorithm used to solve it and the step values, sometimes it did not work properly.

Another existing model studied previously by using Bond-Graph technique and valid to be implemented jointly with the presented model in this paper is the one developed by Le Rolle et al. in 2005 [16], which enables the pulmonary and systemic circulation on the head, abdomen, and legs to be analyzed (Figure 13).

Nevertheless, for the analysis of the good performance associated with the presented blood clot model, the systolic and diastolic blood pressure has been introduced only by using a variable pressure.

If we consider that the blood pressure varies from about 120 mmHg to 80 mmHg (16 kPa to 11 kPa) in systolic to diastolic pressure variation in the normal cardiac cycle and we impose a rate of 1 cycle per second, we can approximate mathematically the pressure (kPa) in two parts (0.00–0.32 sec. and 0.32–1.00 sec.) by using the following polynomial expressions:

$$\begin{aligned} Pa = & 13415 \cdot t^5 - 8508.6 \cdot t^4 + 986.58 \cdot t^3 \\ & + 177.3 \cdot t^2 - 4.99 \cdot t + 11.01, \end{aligned} \quad (9)$$

$$\begin{aligned} Pb = & -1488 \cdot t^6 + 6237.6 \cdot t^5 - 10700 \cdot t^4 \\ & + 9595.3 \cdot t^3 - 4719.5 \cdot t^2 + 1188.3 \cdot t - 102.8. \end{aligned} \quad (10)$$

These equations have been obtained by taking different points from the typical pressure waveform associated.

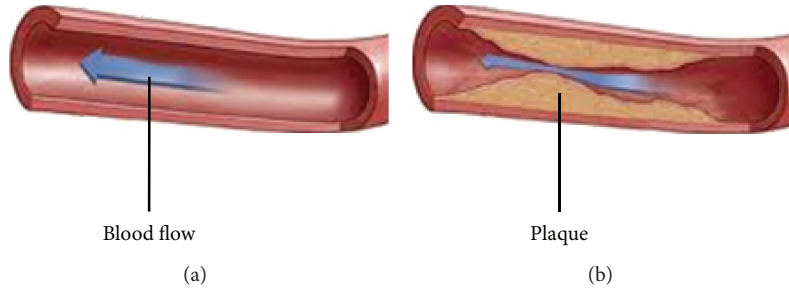


FIGURE 10: Artery blood flow. (a) Normal artery; (b) Artery with atherosclerosis.

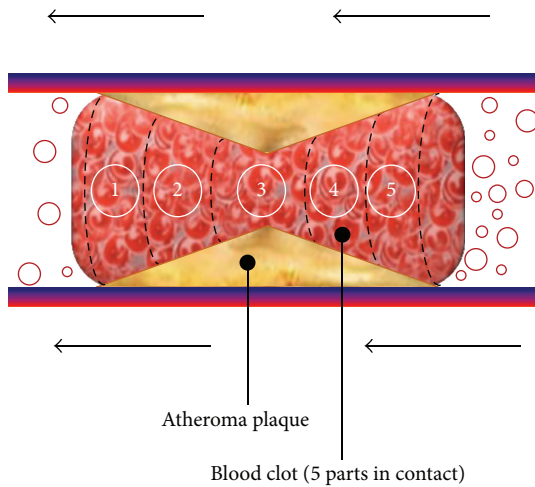


FIGURE 11: Blood clot 5 parts division.

Figure 14 shows the result of implementing the force associated with the previous systolic and diastolic pressure over the 5 partitions model.

4. Bi and Tri-Dimensional Blood Clot Model

The different modifications presented from the initial model obtain a good performance of the blood clot over determined situations, as the results will show. Nevertheless, when the intention of the model is to determine, not when the blood clot begins to move or break, but the detaching process platelet-by-platelet, the presented model is not enough.

To do this, the only option is to amplify the partitions, at least in a second dimension. By doing so, the first line of partitions (as shown in the presented model) would be related to each other (platelet-platelet), with the artery wall (platelet-atheroma) and with the second line of partitions (platelet-platelet); in a similar way, each platelet of the second line would be related to each other and with the third line of partitions, obtaining finally a large amount of related partitions (or platelets).

Nevertheless, the main problem associated with the Bond-Graph technique is concerned with each partition (or platelet), which means one differential equation for each partition or each compliance, it not being possible to approach the problem in the event of excessive increase.

TABLE 1: Parameter values.

Blood density (ρ)	1060 Kg/m ³
Artery diameter	2.5 mm
Blood viscosity (η)	0.0035 Pa·s
K_{union}	1.91 N/m
R_{union}	0.035 N·s/m
Clot length	(1.0–5.0) cm
f_p	0.96
MPA	$5.31 \cdot 10^{-6}$ mm ²
$F_{\text{adhesion.platelet}}$	$32 \cdot 10^{-9}$ N
Occlusion	100%

To do so, the best way would be to use Agent Based Systems, (ABS) [17], which have emerged as one of the most important areas of research and development. An ABS system is one composed of multiple interacting components known as agents that reason logically in a similar way to presented here.

Figure 15 shows a sample made by the authors by using NetLogo software [18]; in this case, it corresponds to 200 partitions, divided into 6 lines. As can be observed, each partition is joined to the closest partitions in a similar way to that presented in this paper.

5. Results

As a final result of the presented Bond-Graph model, the aim of this simulation is to determine the time and pressure required for the extraction of a blood clot. To do this, by varying the values of the pressure source, the movement of the clot and the time required for its extraction are measured, thereby obtaining the optimum minimum pressure. To carry out the model validation, the values of the parameters used in the simulation are listed in Table 1.

The parameters that define almost completely the elastic-plastic behaviour of the clot and its resistance to breaking are the constants “ K_{union} ” and “ R_{union} ” of the spring-damper systems in parallel that are among the partitions of the clot that characterize the clot in the stretch mode, when it undergoes suction but is not yet detached from the wall. To find the value of the “ K_{union} ” parameter, Savushkin [19] analyzes the stiffness of the clot and the breaking strength. We considered that the values are valid, due to the fact that the parameters

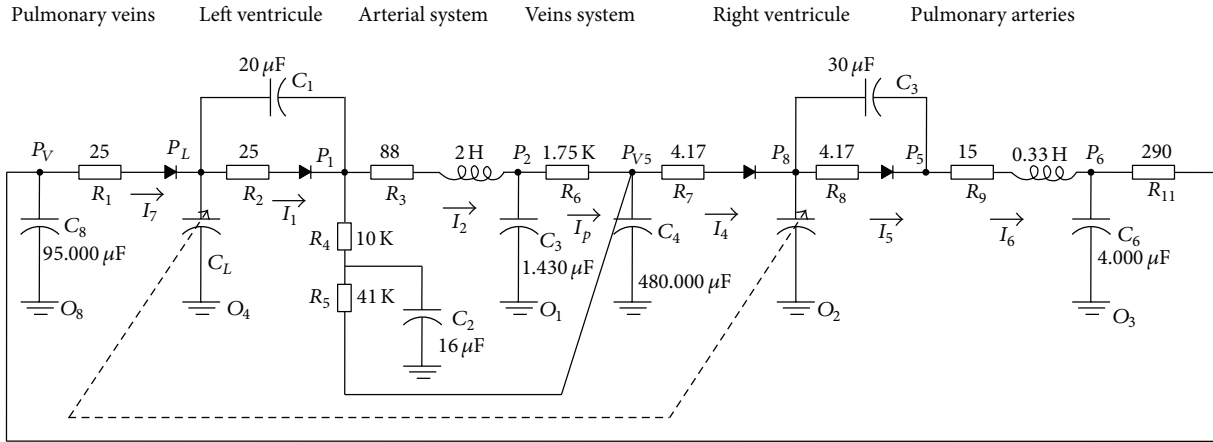


FIGURE 12: Analog circuit for human systemic circulatory system.

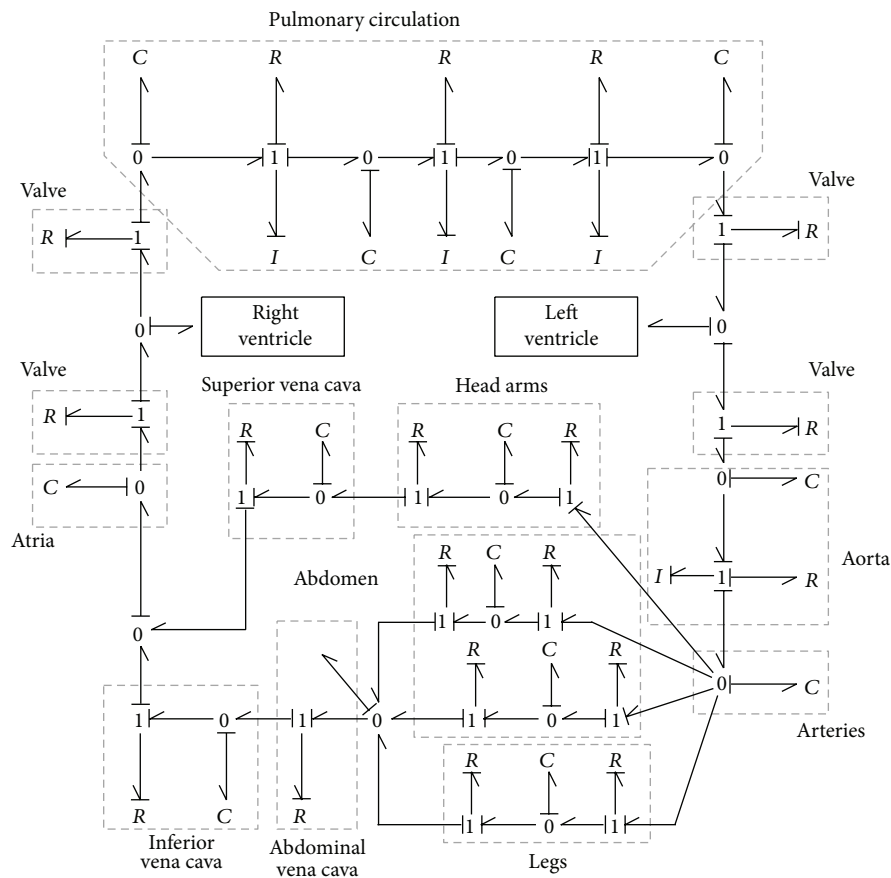


FIGURE 13: Bond Graph model of the circulation.

of the experiments described fall within our range, and therefore we can assume that $K_{union} = 3.41 \pm 1.5 \text{ N/m}$.

Concerning the “ R_{union} ” value, Pennati et al. [20] considers some useful parameters. In that work, values of the viscosity of the blood appear for the clot that they use in their model; taking into account the viscosity of the clot, we can assume that $R_{union} = 0.035 \text{ kg/m}\cdot\text{s}$.

In the model simulated in this section, we take a blood clot of 2.5 mm in diameter and 1.0–5.0 cm in length. The existence of different partitions in the clot makes the extraction progressive with increasing time.

The existence of different clot lengths will affect the mass of the clot being removed (up to 2 gr.) and increase the time taken for clot removal as the value of the clot length increases.

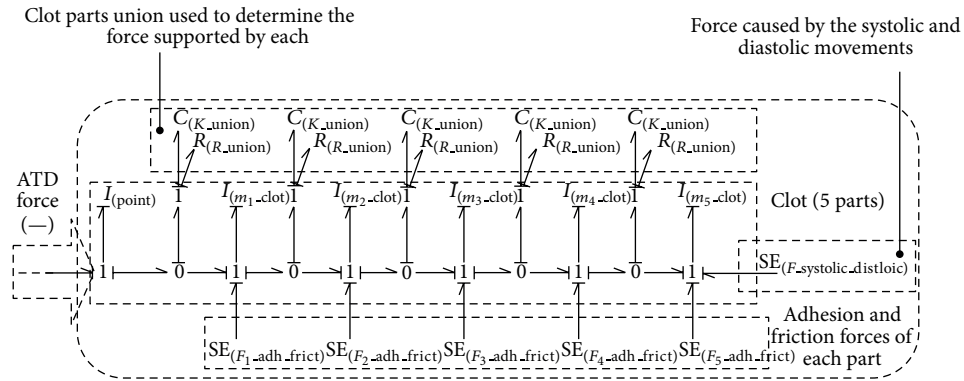


FIGURE 14: The simplest blood clot model by Bond-Graph technique.

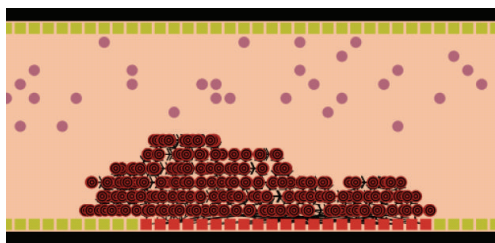


FIGURE 15: ABS blood clot model (200 agents).

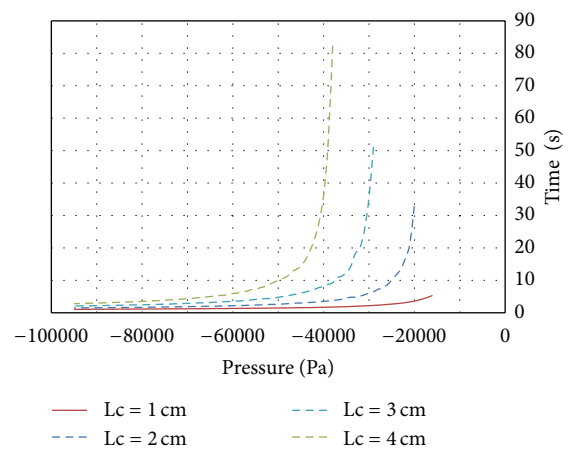


FIGURE 17: Required depression versus time.

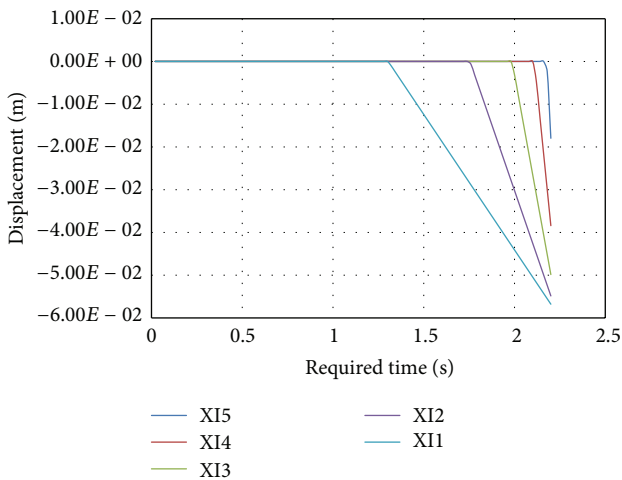


FIGURE 16: Movement of each blood clot part.

It has been found, that the greater the rigidity of the clot, the shorter the extraction time. This factor is also related to the viscosity and composition of the clot that will vary in each case. Therefore, for this study we have determined the critical values possible, making the assumption that there are 96% platelets in the clot, which yields a fairly high bond strength, which gives us an idea of the maximum pressure needed.

Figure 16 shows the movement of each blood clot taking into account the increasing value of the suction pressure in the first second. Once the force over one partition is greater than the adhesion force in it between blood clot and artery, the adhesion is broken and clot movement begins. In addition, it is possible to look at the velocity when one section

is detached and this is higher since all the force is applied over lesser partitions.

The usefulness of the presented model is concerned with the time the blood clot takes to move a concrete distance (e.g., 2-3 mm), which is the distance that is maintained during the extraction to the TAD device. In Figure 17, we can observe the different times to extract a blood clot in a 100% occlusion case, with a diameter of $D = 2.5$ mm and for different lengths such as 1.0–5.0 cm, respectively; these results have been compared with those obtained by using the GP at the laboratory [5] and it contains very similar results.

As we can see, the lower the length the lower the time needed to extract the clot, because we have less adherence force and less inertia due to the mass. We have applied it to the extraction of a 5.0 cm length but there is a danger of rupture prior to complete clot removal, which would mean the failure of the process, due to the fact that the force supported by the blood clot is higher than the rupture force (more length means more adherence).

6. Conclusions

We have studied the formation, composition, and shape of different blood clots in different cases, trying to find some general parameters that could define their behaviour reliably.

In particular, we have studied the influence of composition, form, and some parameters that directly affect the adhesive force that holds the clot against the arterial wall. The most significant inclusion in the model, and therefore the one that provides greater reliability to the model, has been the change in the approach regarding the internal structure of the clot and its adherence to the wall.

It is necessary to say that, for the exact modelling of the laboratory experiment, the different parameters should have been obtained over the existing blood clot, not from the literature.

Many previous studies analyze similar models by using Finite Element Analysis, where it is often necessary to reproduce the full situation which usually requires a lot of computer simulation time. Nevertheless, there is not any model developed by using the Bond Graph technique.

Apart from demonstrating that the technique is very useful to represent the different simulation conditions, making it possible to incorporate different parameters in a very effective straightforward manner, the very simple model obtained in the presented work will let future researchers obtain the differential equation system, without the need of complex models by using Finite Element Analysis or Agent-Based Systems techniques.

Acknowledgment

The authors would like to thank Dr. Gillian Pearce, inventor of the GP device, which has been the TAD device taken as reference to simulate and test the different Bond-Graph models presented.

References

- [1] "Stroke association website," <http://www.stroke.org.uk>.
- [2] J. P. Broderick, "Endovascular therapy for acute ischemic stroke," *Stroke*, vol. 40, no. 3, supplement, pp. S103–S106, 2009.
- [3] L. Thomassen and S. J. Bakke, "Endovascular reperfusion therapy in acute ischaemic stroke," *Acta Neurologica Scandinavica*, vol. 115, no. 187, pp. 22–29, 2007.
- [4] P. M. Rothwell, M. Eliasziw, S. A. Gutnikov, C. P. Warlow, and H. J. M. Barnett, "Endarterectomy for symptomatic carotid stenosis in relation to clinical subgroups and timing of surgery," *The Lancet*, vol. 363, no. 9413, pp. 915–924, 2004.
- [5] G. Pearce, J. H. Patrick, and F. Jaegle, "The design, implementation and testing of a new revolutionary device for the treatment of blood clots in the arterial system," in *Proceedings of the 9th International Conference on Computer Modelling and Simulation*, pp. 6–9, Oxford, UK, 2006.
- [6] G. Pearce, R. Andrews, J. H. Patrick, and N. D. Perkinson, "An investigation into the performance of a new clot removal device," in *Proceedings of the European Modelling Symposium*, pp. 58–61, UK Society for Modelling and Simulation, London, UK, 2006.
- [7] G. Pearce and N. D. Perkinson, "Biomechanical probe," International Patent Corporate Treatise, WO 2006120464, 2007.
- [8] G. Frenkel, S. Gorohovsky, S. Ini, T. Koltai, and M. Pinchasov, "Polymorphic forms of tegaserod maleate," European Patent, EP 1893195 (A2), 2008.
- [9] G. Pearce and N. D. Perkinson, "Biomechanical probe," Japanese Patent, JP2008539924 (A), 2008.
- [10] G. Pearce and N. D. Perkinson, "Biomechanical probe," Chinese Patent, CN101208049 (A), 2008.
- [11] D. C. Karnopp, D. L. Margolis, and R. C. Rosenberg, *System Dynamics: A Unified Approach*, John Wiley & Sons, New York, NY, USA, 2nd edition, 1990.
- [12] G. Romero, I. Higuera, J. F  lez, G. Pearce, and N. D. Perkinson, "Modelling and simulation of a thrombectomy probe applied to the middle cerebral artery by using the bond graph technique," in *Proceedings of the 9th International Conference on Bond Graph Modeling and Simulation*, pp. 172–179, Orlando, Fla, USA, 2010.
- [13] S. Shiozaki, K. I. Ishikawa, and S. Takagi, "Numerical study on platelet adhesion to vessel walls using the Kinetic Monte Carlo Method," *Journal of Biomechanical Science and Engineering*, vol. 7, no. 2, pp. 275–283, 2012.
- [14] C. J. Flannery, *Thrombus formation under high shear in arterial stenotic flow [Ph.D. thesis]*, Georgia Institute of Technology, Atlanta, Ga, USA, 2005.
- [15] A. Noordergraaf, *Circulatory Systems Dynamics*, Academic Press, New York, NY, USA, 1978.
- [16] V. Le Rolle, A. I. Hernandez, P. Y. Richard, J. Buisson, and G. Carrault, "A bond graph model of the cardiovascular system," *Acta Biotheoretica*, vol. 53, no. 4, pp. 295–312, 2005.
- [17] "Agent-based model," Wikipedia website, http://en.wikipedia.org/wiki/Agent-based_model.
- [18] "NetLogo software website," <http://ccl.northwestern.edu/netlogo/>.
- [19] A. V. Savushkin, "Clots of blood plasma," *Journal of Engineering Physics and Thermophysics*, vol. 76, no. 3, pp. 645–647, 2003.
- [20] G. Pennati, R. Balossino, G. Dubini, and F. Migliavacca, "Numerical simulation of thrombus aspiration in two realistic models of catheter tips," *Artificial Organs*, vol. 34, no. 4, pp. 301–310, 2010.

Research Article

Use of Computational Fluid Dynamics to Estimate Hemodynamic Effects of Respiration on Hypoplastic Left Heart Syndrome Surgery: Total Cavopulmonary Connection Treatments

Jinlong Liu,¹ Yi Qian,² Qi Sun,¹ Jinfen Liu,¹ and Mitsuo Umezu³

¹ Department of Cardiothoracic Surgery, Shanghai Children's Medical Centre, Shanghai Jiao Tong University School of Medicine, 1678 Dongfang Road, Shanghai 200127, China

² Australian School of Advanced Medicine, 2 Technology Place, Macquarie University, North Ryde, Sydney, NSW 2109, Australia

³ ASMeW Lab, Centre for Advanced Biomedical Sciences, TWIns, Waseda University, 2-2 Wakamatsucho, Shinjuku, Tokyo 162-8480, Japan

Correspondence should be addressed to Yi Qian; yi.qian@mq.edu.au

Received 29 July 2013; Accepted 6 November 2013

Academic Editors: S. Jahandideh, P. Kok, and A. Zaravinos

Copyright © 2013 Jinlong Liu et al. This is an open access article distributed under the Creative Commons Attribution License, which permits unrestricted use, distribution, and reproduction in any medium, provided the original work is properly cited.

Total cavopulmonary connection (TCPC), a typical kind of Fontan procedure, is commonly used in the treatment of a functional single ventricle. The palliative cardiothoracic procedure is performed by connecting the superior vena cava and the inferior vena cava to the pulmonary arteries. Due to the difficulty of direct study *in vivo*, in this paper, computational fluid dynamics (CFD) was introduced to estimate the outcomes of patient-specific TCPC configuration. We mainly focused on the influence of blood pulsation and respiration. Fast Fourier transforms method was employed to separate the measured flow conditions into the rate of breath and heart beat. Blood flow performance around the TCPC connection was investigated by analyzing the results of time-varying energy losses, blood flow distribution rate, local pressure, and wall shear stress distributions. It was found that the value of energy loss including the influence of respiration was 1.5 times higher than the value of energy loss disregarding respiratory influences. The results indicated that the hemodynamic outcomes of TCPC treatment are obviously influenced by respiration. The influence of respiration plays an important role in estimating the results of TCPC treatment and thus should be included as one of the important conditions of computational haemodynamic analysis.

1. Introduction

Fontan procedure was designed to treat complex congenital heart diseases (CHD) for patients with single ventricles, such as those suffering from tricuspid atresia and hypoplastic left heart syndrome (HLHS), which cannot be treated by biventricular repair [1]. During this kind of procedure, both the superior vena cava (SVC) and the inferior vena cava (IVC) are connected to the pulmonary arteries, thus allowing venous blood to flow directly from the body to the lungs via the pulmonary artery, bypassing the right ventricle. After Fontan and Baudet [2] introduced a nonanatomic correction of tricuspid atresia through innovative surgical approach in 1971,

the original “Fontan” procedure has been modified into two main types of procedures—intracardiac (LT) lateral tunnel Fontan and extracardiac conduit (ECC) Fontan over the past 40 years.

Although survival rate after Fontan procedures has improved over the years, a number of unresolved questions continue to surround management and treatment [3]. Despite advancement in surgical techniques and medical therapies, pediatric cardiologists are still challenged by discussions regarding initial decision relative to treatment and long-term prognosis [4–6]. This is partly due to limited data available before and after the conduction of these therapies. Currently, many researchers and surgeons have been working to

obtain such data for the improvement of the treatment of Fontan-type procedures based on the results of numerical investigations. These numerical techniques allow us to examine the effects of the geometry at the Fontan connection area and assess blood flow characteristics and energy loss (EL) associated with a given surgical design [7–11]. Numerous research papers have been published on the study of the Fontan procedure and its modifications, particularly, the total cavopulmonary connection (TCPC) procedure, such as Bove et al. [7], Migliavacca et al. [8], and Orlando et al. [9]. Meanwhile, many articles focused on the hemodynamic analysis of TCPC procedure. Sievers et al. [10] illustrated that the turbulence at the anastomosis of connection area was the reason for energy dissipation. Whitehead et al. [11] studied the power loss of TCPC connection area at exercise and the interaction between power loss and varying flow distribution to each lung under exercise conditions. However, most of these previous studies concentrated on the certain ratio of flow distribution within pulmonary arteries and the rate of EL during instantaneous rest or exercise. The physiological effects of blood flow pulsation and respiration were not considered. Previous clinical studies such as those of Rosenthal et al. [12], Pedersen et al. [13], and Hjortdal et al. [14] have indicated that pulmonary blood flow was obviously effected from breathing pressure. In recent years, some hemodynamic researchers began to investigate the effects of influence from blood flow pulsation and respiration, such as Marsden et al. [15, 16] and Itatani et al. [17], whereas little detailed information is available on numerical analysis to directly disclose the influence of respiration on hemodynamic characteristics in published works and papers. Marsden et al. [15] reported that respiration significantly affected Fontan flow rates and pressure. As a matter of fact, their article placed great emphasis on the analysis of respiration effects on the inflow at the SVC and IVC through the use of a quadratic polynomial form as respiration model. There was little investigation of the effect of respiration on pressure distribution at the inlets and outlets. In addition, although their studies have investigated the results of pressure decline through steady simulation with catheter-measured clinical data, the results were unable to provide useful boundary condition for CFD simulation to estimate the influence of respiration in independent patients. Itatani et al. [17] conducted the investigation of optimal conduit size of the ECC Fontan procedure by using basic geometry model. Although the influence of respiration was introduced into the simulation, constant pressure condition was applied at bilateral pulmonary arteries during expiratory phase, and pressure drop is assumed to be constant during inspiratory phase. The conditions have not precisely demonstrated the physiological effects from respiration. Marsden et al. [16] reported that they applied the coupled multidomain method with a lumped parameter three-element Windkessel model [18] at the outlets to investigate the influence of respiration. On the other hand, Stergiopoulos et al. [19] and Segers et al. [20] have proved that the lumped parameter three-element Windkessel model overestimated the total arterial compliance and underestimated the characteristic impedance. The pulse pressure was predicted to be too high, and diastolic pressure wave was abnormal. Westerhof et al.

[21] certified that the inflection point and the augmentation of pressure wave were not represented well by this model.

In the present research, we introduced the system of computational hemodynamic analysis, developed for first-stage HLHS surgery, Norwood procedure [22], to obtain the blood flow data at the TCPC connection area in detail, taking the influence of blood pulsation and respiration into account. The CFD methodology was applied to analyze the blood flow based on a patient-specific configuration acquired by magnetic resonance imaging (MRI), with physiologically realistic flow conditions measured in vivo through the utilization of ultrasound measurement in real time with electrocardiogram (ECG) at the SVC and IVC. Pressure conditions were obtained through the use of an intracardiac catheter with pressure sensors at the left pulmonary artery (LPA) and right pulmonary artery (RPA). We employed the method of fast Fourier transforms (FFT) to separate the measured blood flow through the different frequency of breaths and heart beats. We then compared the calculated results obtained imposing inflow boundary conditions for two cases: one considering both cardiac and respiratory pulsatility and the other considering only cardiac pulsatility. The results showed significant differences in EL, pressure, wall shear stress (WSS), and velocity magnitude. The aims of this study were to explore important issues of respiration effects on the hemodynamic analysis of TCPC procedure and to develop a method to improve the hemodynamic study of TCPC procedure by CFD technology.

2. Materials and Methods

2.1. Subject Selection and Clinical Information. In this study, the geometry of TCPC connection was extracted from a six-year-old female patient, who had been diagnosed with pulmonary atresia, ventricular septal defect, atrial septal defect, patent ductus arteriosus, and dextrocardia at birth. She underwent a Hemi-Fontan procedure at the age of two. During the intracardiac Fontan procedure, at four years of age, the IVC was connected to the RPA by an intracardiac lateral tunnel, and a 3 mm diameter fenestration was made on the lateral tunnel. With the consent of the parents and the approval of the local institutional review board and the regional research ethics committee, our patient-specific associated studies were approved.

MRI and ultrasound were performed on the patient when she returned to the hospital for a follow-up medical examination. MRI and ultrasound results showed that the lateral tunnel fenestration made during the Fontan procedure had closed spontaneously. A series of continuous 4 mm thick MRI images were acquired on a 1.5 Tesla Signa Hispeed Scanner (GE Medical System, General Electric, USA) with a 256×192 pixel field of view to define the anatomies of Fontan connections. Moreover, the time-dependent velocity profiles of patient-specific physiological blood flow at the left innominate vein (LIV), right innominate vein (RIV), and IVC were obtained in real time through ultrasound measurement in with ECG. Pressure boundary conditions were measured in vivo real time through the use of an intracardiac catheter with pressure sensors. All data is depicted in Figure 1.

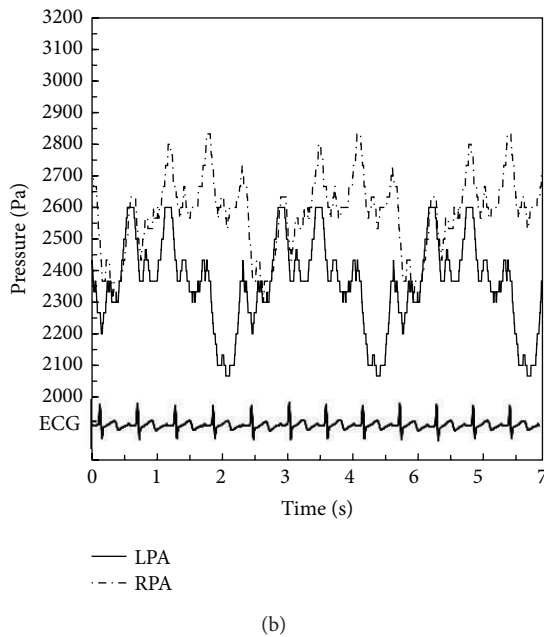
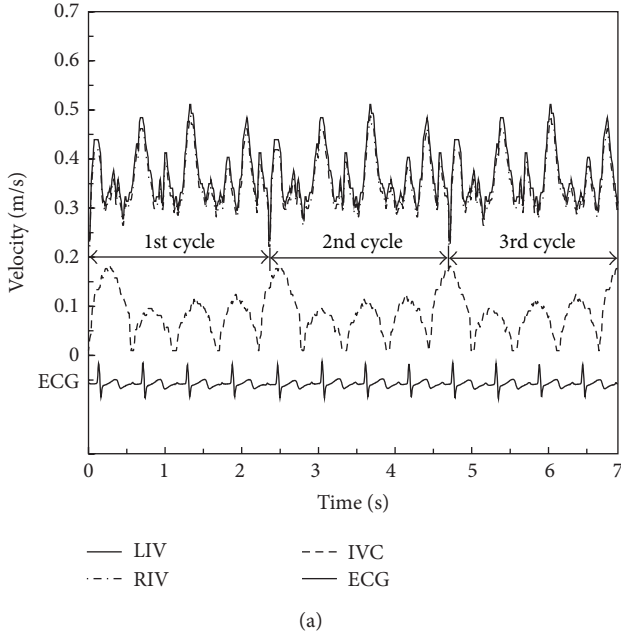


FIGURE 1: Clinical data as boundary conditions taking respiration into account. (a) Velocity data as inlet boundary conditions at the IVC, LIV, and RIV. (b) Pressure data as outlet boundary conditions at the LPA and RPA (IVC: inferior vena cava; LIV: left innominate vein; RIV: right innominate vein; LPA: left pulmonary artery; RPA: right pulmonary artery; ECG: electrocardiogram).

2.2. Model Reconstruction and Clinical Data Processing. Eighteen slices of cross-sectional fast imaging employing steady-state acquisition (FIESTA) sequence MRI images were used for patient-specific three-dimensional reconstruction of the vessels through commercial software Mimics 12.0. The accuracy of the reconstructed model had been checked against the geometry with an exacted measurement carried out by the original DICOM MRI slice files. A nonshrinking

smoothing technique was employed to generate the numerical model for CFD simulation [23]. The geometry after smoothing is shown in Figure 2.

The velocity result files at LIV, RIV, and IVC, acquired through ultrasound measurement, were stored in ASCII format as boundary conditions for the CFD simulation. The velocity results contained the respiratory cycle data. We used the FFT methodology to separate the interaction of respiration by the different frequency between breath and heart beat through the use of commercial software MATLAB 7. Consequently, the present study could be conducted under the following conditions: (I) pulsatile flow without considering the influence of respiration and (II) pulsatile flow with the influence of respiration. Detailed information of blood velocity after FFT separation is displayed in Figure 3. One cycle of breath includes four heart pulsatile circulations.

2.3. Governing Equations. The flow simulation was based on the Navier-Stokes (N-S) momentum equation and continuity equation defined as follows:

$$\begin{aligned} \frac{\partial}{\partial t} (\rho u_i) + \frac{\partial}{\partial x_j} (\rho u_i u_j) \\ = -\frac{\partial p}{\partial x_i} + \frac{\partial}{\partial x_j} \left[\mu \left(\frac{\partial u_i}{\partial x_j} + \frac{\partial u_j}{\partial x_i} \right) \right] + f_i, \quad (1) \\ \frac{\partial \rho}{\partial t} + \frac{\partial}{\partial x_j} (\rho u_j) = 0, \end{aligned}$$

where $i, j = 1, 2, 3, x_1, x_2, x_3$ represent coordinate axes, u_i, u_j , and p are the velocity vectors and the pressure at any point in the flow domain, ρ and μ are blood density and viscosity, and t is time. The term f_i expresses the action of body forces.

Due to the relatively large sizes of the vessels compared to individual blood cells [24] and the great shear stress typical within larger arteries [25], the blood was assumed to be a Newtonian fluid with a constant density ($\rho = 1060 \text{ kg/m}^3$) and viscosity ($\mu = 4.0 \text{ mPas}$) [26–28], while the body forces were omitted. Therefore, the N-S equations are turned into the following form:

$$\begin{aligned} \rho \frac{\partial U}{\partial t} + \rho (U \cdot \nabla) U - \mu \nabla^2 U + \nabla p = 0, \quad (2) \\ \nabla \cdot U = 0, \end{aligned}$$

where $U = U(u_1, u_2, u)$ is the velocity vector.

The Reynolds number (Re), the ratio of the inertial forces to the viscous forces in the flow, is defined by

$$\text{Re} = \frac{\rho U D}{\mu}, \quad (3)$$

where D is the characteristic length.

In this TCPC case, time-averaged velocity was 0.3419 m/s with maximum Re number of 802.53 at Condition I. At Condition II, considering the influence of respiration, the maximum Re was lower than 1000, which was calculated at

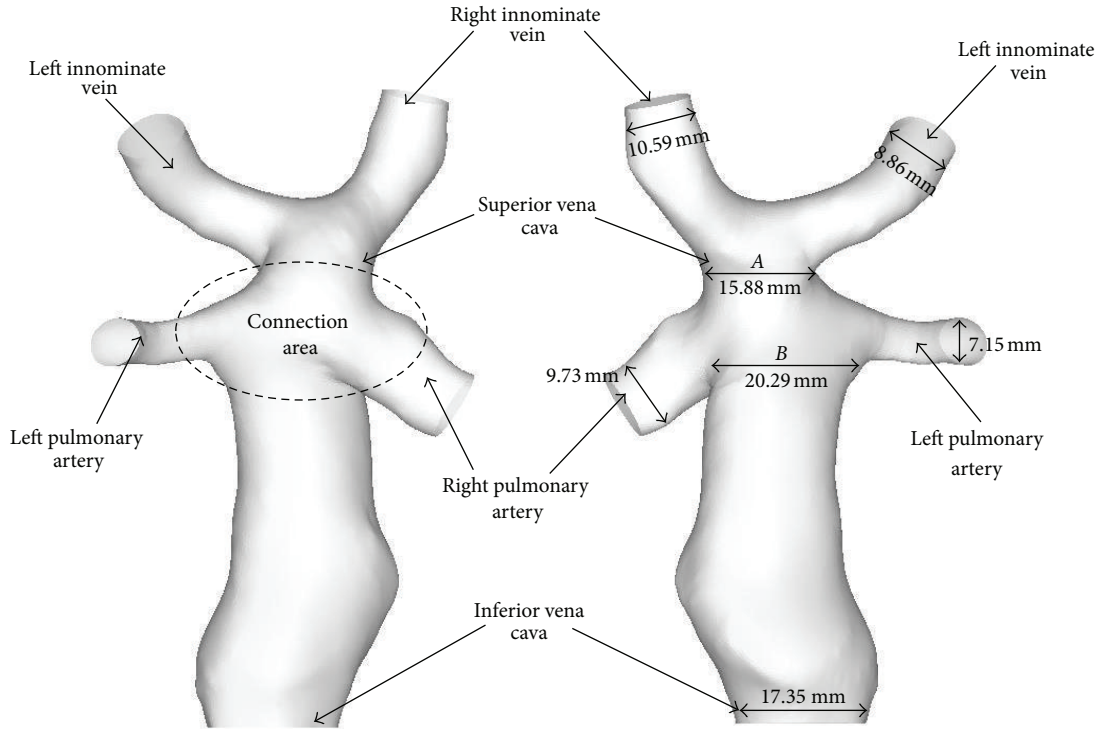


FIGURE 2: The patient-specific three-dimensional reconstructed configuration after surface smoothing.

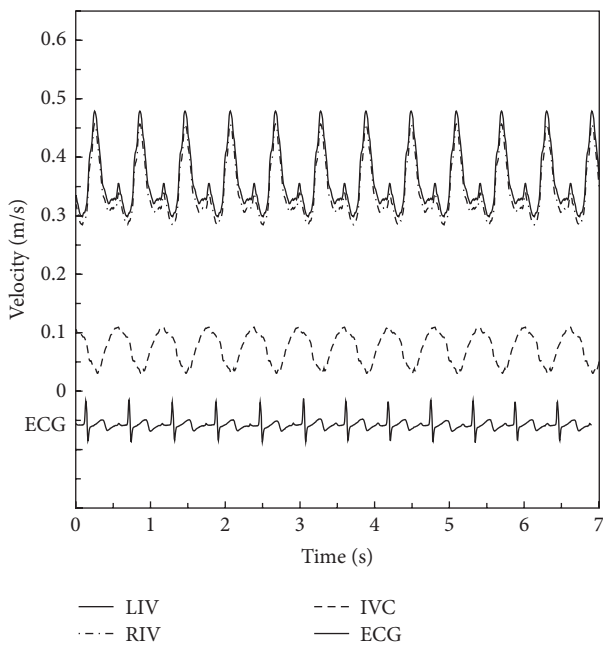


FIGURE 3: Velocity data as inlet boundary conditions only including cardiac pulsatility (IVC: inferior vena cava; LIV: left innominate vein; RIV: right innominate vein; ECG: electrocardiogram).

the peak of the velocity wave at Condition II. Therefore, the flow is able to be described as a laminar flow at both conditions of this study. From the clinical viewpoint, the intracardiac lateral tunnel reduced atrial enlargement due to the

decreasing of right atrial surface space. De Leval et al. [29] and Mavroudis and Backer [30] investigated that the flow passing through the baffle was laminar flow, which improved the hemodynamic performance of the Fontan circuit flow and reduced the EL within the dilated right atrium.

2.4. Mesh Generation. The grid-generation software ANSYS-ICEM 12.1 was utilized to discretize the computational domain. In order to accurately measure WSS at near-wall regions, the body-fitted prism layers were generated near the vessel walls to improve the resolution of the relevant scales in fluid motion. There were five layers generated with an average nodal space, increasing by a ratio of 1.2. The distance from the first layer to the vessel surface was fixed at 0.02 mm. From the centre of the vessels to the prism inner layer, tetrahedral grids in varying sizes were utilized. To verify the reliability, grid independence of the WSS [31] was checked by calculation with finer meshes, where the maximum cell size was decreased to 0.2 mm, with no consequent change occurring in the results of WSS. The generated meshes are shown in Figure 4.

Considering that the quality of CFD results was highly dependent on grid resolution and boundary conditions, a series of grid-dependent validations were performed by extending the domain length at inlets and outlets. As shown in Figure 5, when the grid number at the research domain was around 400,000, the EL started to converge into a constant. Therefore, accurately reliable results could be obtained with a total of 563,601 finite elements and 239,521 nodes, as utilized in the current study.

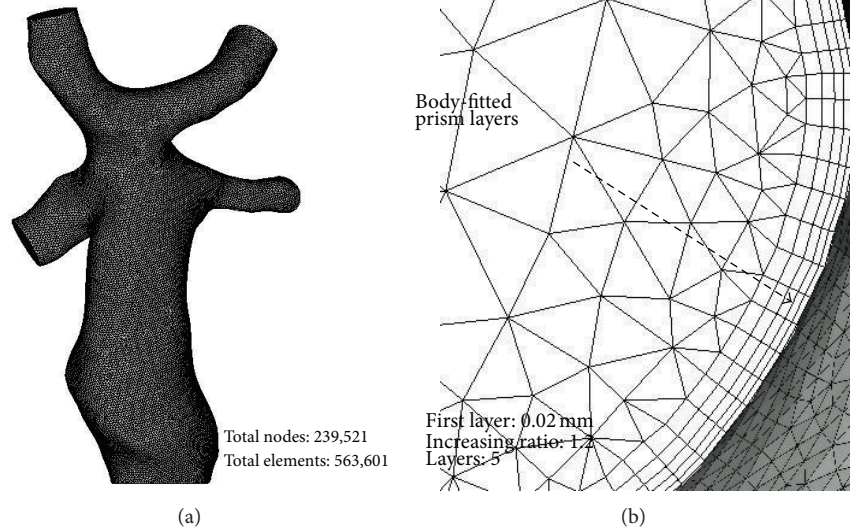


FIGURE 4: Mesh information. (a) Calculation domain with grids. (b) Body-fitted prism layers.

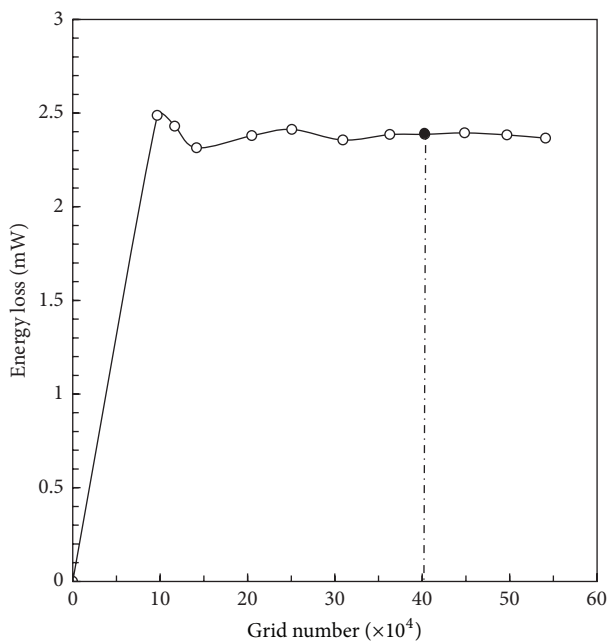


FIGURE 5: Results of grid independent verification.

2.5. Boundary Conditions and Calculation. According to the research of Migliavacca et al. [32], the different velocity profiles adopted at the inlets only have minor effects on blood distribution into the lungs in the TCPC simulation. Though there were slight differences, the volume flow curves calculated under zero pressure at the outlets practically coincided with the curves from in vivo measurements. Thus, the pulsatile velocities shown in Figure 3 were applied as the inlet boundary conditions (BCs), and a zero pressure condition was used at the outlets in the simulation of Condition I. Different boundary conditions were utilized in the simulation of Condition II. The time-dependent velocities and pressure

displayed in Figure 1 were used as the inlet BC and outlet BC. For these simulations, we assumed the rigidity of vessel wall surfaces.

The finite volume solver package ANSYS-FLUENT 6.3 was employed to solve the fluid equations. The N-S equations were solved by the transient solution method, and the Adams-Bashford method was applied for the second-order transient solution of the time-dependent N-S equations. The terms of pressure and momentum in the equations were discretized using a second-order upwinding scheme, and the convergence criteria were to reduce the residuals of continuity and momentum equations to 10⁻⁵. A subroutine based on the C programming language was written in order to create a user-defined function for the Fluent code to impose time-dependent velocities as the inlet BCs and pressure as the outlet BCs. The vessels were assumed as rigid and no-slip surfaces at both Conditions. In order to obtain a periodic solution, six heart cycles for Condition I and three times of breath (12 heart beats) for Condition II were carried out in total, respectively. To obtain accuracy, calculation time step was set to 0.0001 seconds according to the calculation of the Courant number, defined as follows:

$$C_r = \bar{u} \frac{\Delta t}{\Delta l}, \quad (4)$$

where \bar{u} is average velocity, Δt is maximum time step size, and Δl is dimension of grid cell. In total, 36,000 and 68,000 steps were calculated for Condition I and Condition II, with the calculation time set to nine days and eighteen days, respectively. All of the computations were performed on a workstation with a Windows XP operation system. The workstation was equipped by double CPUs: Intel (R) Pentium III Xeon (R) 3.0 GHz processors, with 16.0 GB RAM memory, and a 64-bit Windows XP operation system.

2.6. Flow Distribution Ratio and Energy Loss. To evaluate the effects of respiration on hemodynamics, quantitative indexes

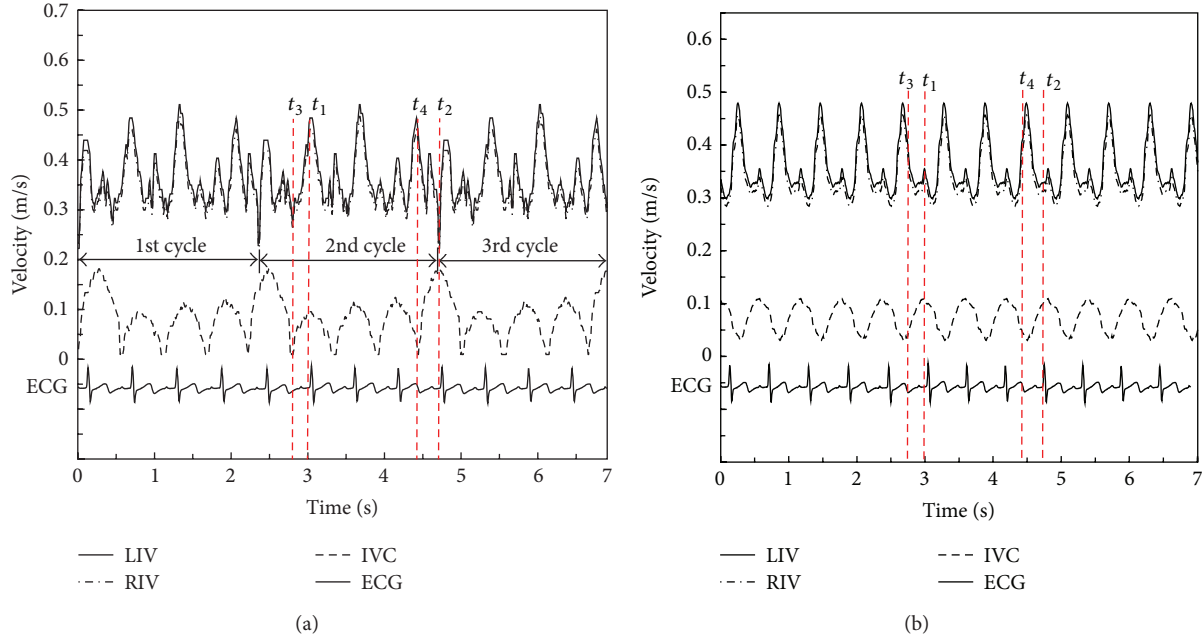


FIGURE 6: Four selected time steps for hemodynamic comparison (t_1 , t_2 , t_3 , and t_4). (a) Inlet velocity conditions taking respiration into account. (b) Inlet velocity conditions only including cardiac pulsatility (IVC: inferior vena cava; LIV: left innominate vein; RIV: right innominate vein; LPA: left pulmonary artery; RPA: right pulmonary artery; ECG: electrocardiogram).

were defined, including the flow distribution ratio (FR) and control volume energy loss (EL). The FR used to evaluate the outcomes of TCPC procedure on the balance of blood distribution between the LPA and RPA is given by

$$FR = \frac{Q_{LPA}}{Q_{inlet}} \times 100\%, \quad (5)$$

where Q_{LPA} is the flow in the left pulmonary artery and Q_{inlet} is the sum of the IVC, LIV, and RIV inlet flows.

The control volume (CV) EL, also named control volume power loss, is defined by

$$EL = \sum_t \left[\sum_i \left(P_i + \frac{1}{2} \rho U_i^2 + \rho \frac{\partial \Phi_i}{\partial t} \right) Q_i - \sum_o \left(P_o + \frac{1}{2} \rho U_o^2 + \rho \frac{\partial \Phi_o}{\partial t} \right) Q_o \right], \quad (6)$$

where i is element number at inlet and o is element number at outlet. Inlet boundaries include the IVC, LIV, and RIV, while the outlet boundaries are the LPA and RPA. $\partial \Phi / \partial t$ denotes the partial derivative of the velocity potential Φ with respect to time t , $U = |\nabla \Phi|$ is blood velocity, and P and Q define static pressure and volume flow rate, respectively.

3. Results

We selected four different time steps (t_1 , t_2 , t_3 , and t_4) to compare the hemodynamic characteristics between the two conditions. The detailed information of the four time steps is

TABLE 1: The definition of four selected time steps at Figure 6(a).

Time step	Velocity information	
	IVC	LIV and RIV
t_1	Peak	Peak
t_2	Peak	Bottom
t_3	Bottom	Bottom
t_4	Bottom	Peak

given in Table 1. The boundary conditions at these steps are shown in Figure 6.

In order to compare the difference of pressure distribution between two boundary conditions, the relative pressure, which was calculated by using boundary Condition II, was reduced to the same level of boundary Condition I (minimum diastolic pressure at PLPA = 0). The modified pressure results were shown in Figure 7. Due to our interest in relative pressure, the pressure modification did not influence the results of EL calculation. The pressure was much higher at Condition II than that at Condition I at t_1 , t_3 , and t_4 while being lower at t_2 . The influence of respiration was believed to be significant for pressure distribution. We also found relatively lower pressure zones at the entrances of LPA and RPA, with the size of these zones altered with each subsequent time step.

WSS is displayed in Figure 8. We observed relatively higher WSS distribution in three zones on the configuration at both conditions: the SVC connection area, the RIV, and the RPA. Examining the geometry, the distorted spatial configuration of vessels created in the surgery might be one of the main reasons. The highest value of WSS was found at

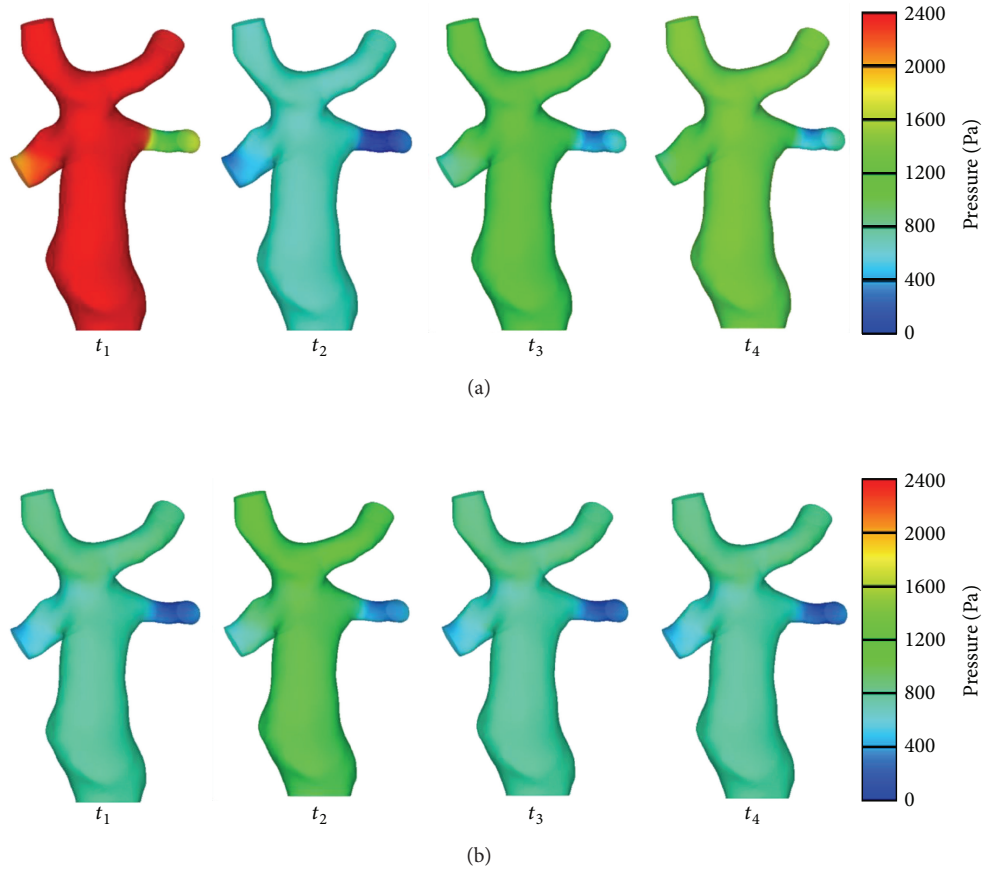


FIGURE 7: Pressure distribution (Condition II (a) and Condition I (b)).

the LPA at Condition II. It indicated that greater energy was lost at this location. Also, the size and location of these high-WSS zones changed instantaneously with the four time steps. Because a close relationship exists between WSS and velocity gradient ($\tau_{\text{wall}} = -\mu \partial U_x / \partial y|_{y=0}$, where τ_{wall} represents WSS, μ is blood viscosity, $\partial U_x / \partial y$ is velocity gradient, U_x is velocity of the fluid near the boundary, and y is the height above the boundary), the velocity gradient was believed to have diversified at these zones with each subsequent time step. On the other hand, we found that a relatively low WSS existed at the SVC at Condition II and that the lower value most likely weakened the influence of blood flow on endothelial layer function at this zone. Thus, the influence of respiration should be counted as one of the important factors in the calculation of the results, and this influence may create minor oscillations of WSS at Condition II.

Figure 9 depicts the streamlines at each time step. High-speed zones distributed at the LPA and RPA at both conditions. The highest value of velocity was found at the LPA at Condition II, meaning that respiration affected the pulmonary blood flow through this increase of velocity. At the confluent location, two flows from LIV and RIV were blended, and a low-speed area was observed at both Condition I and Condition II. Moreover, a relatively lower velocity was found in the confluent area at Condition II. This implied that

greater EL was generated when the two flows encountered and passed through the SVC connection area. An unstable blended flow occurred at the connection area between the IVC and SVC.

Time-dependent EL and time-averaged EL were calculated as shown in Figure 10. The EL was lower at Condition II. The maximum value of time-dependent EL was approximately 0.04725 W at Condition II, lower than that at Condition I, 0.05581 W. Furthermore, the time-averaged value of EL at Condition II was approximately 1.5 times lower than that at Condition I. This implied that the blood flow could obtain energy from respiration to complement losses caused by flow, confirming the conclusion of the previous study that spontaneous breathing provided additional energy for blood flow [33, 34]. More specifically, the maximum value of this difference was around 0.05 W. Unlike the regular curve shape at Condition I, the curve of EL fluctuated at Condition II during the whole breath cycle. A big wave followed some small waves. It indicated that inspiration and expiration had different influence on EL. When the patient inspired, the maximum value of EL appeared. From the time-dependent EL, we found some evidence of the influence of respiration on EL. Detailed analysis will be part of future work on the investigation of the time-dependent EL during both inspiration and expiration. This will likely become one of the

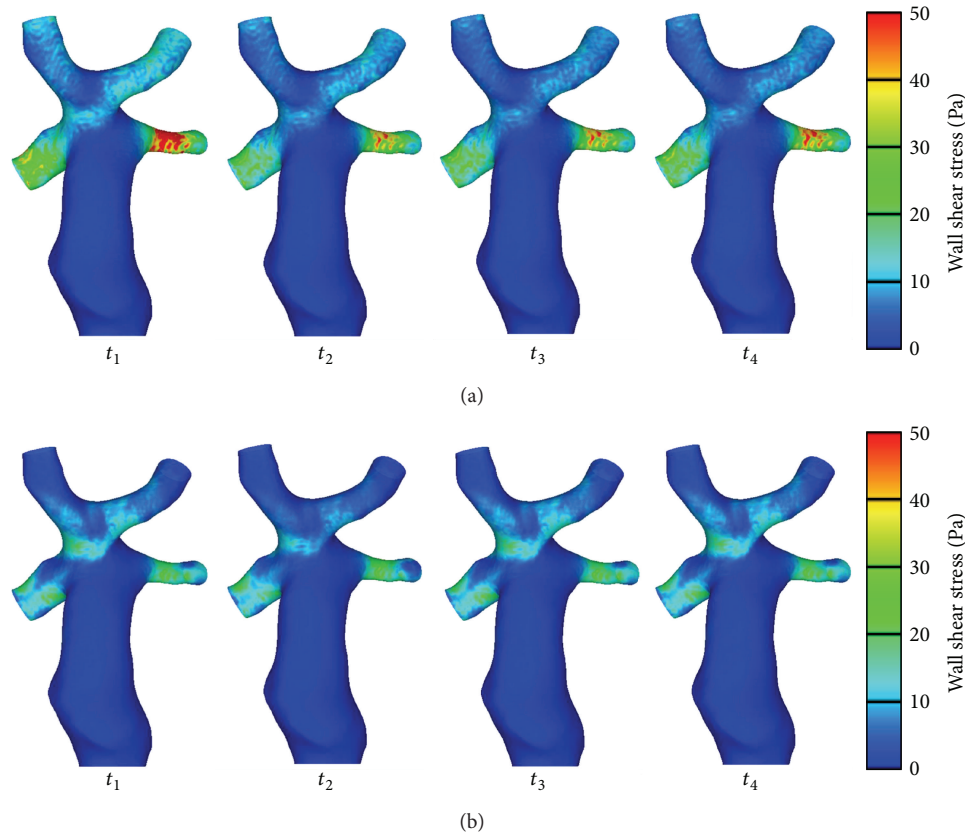


FIGURE 8: Results of wall shear stress (Condition II (a) and Condition I (b)).

methods for the patient's clinical examination, through the calculation of real-time EL in blood flow, with the influence of respiration.

Figure 11 describes the percentages of flow ratio distributed at the LPA. The temporal value of the proportion at the LPA was different at each subsequent time step, at both conditions. The instantaneous value of the percentage varied between 29% and 33% at Condition II in one heart cycle, while the value at Condition I ranged from 28.9% to 31.5%. However, the time-averaged value of FR at both conditions was almost the same, around 30%. There was approximately only a 0.6% difference between both values. The results revealed that respiration was not the main influence on the results of the mass flow distribution and that the time-averaged ratio of mass flow distribution between the LPA and RPA was close to 3 : 7 in this patient-specific case.

4. Discussion

Because the TCPC connection area was located in the thoracic cavity and was connected to the lungs through pulmonary arteries, the effect of respiration may have had a great influence on the hemodynamic features in the anastomotic region. In the present study, the computational hemodynamic analysis methodology was used to analyze the characteristics of local blood flow by evaluating the influence of respiration in pulsatile simulation. The accuracy of computation

methodology on pulsatile simulation has been discussed in our previous work [22].

Patient-specific pressure data was used as boundary conditions to estimate the hemodynamic influence of respiration. Although we noted that lumped parameter methods have been reported in some cardiovascular hemodynamic literatures, they were still short in evidence for the confirmation of its accuracy *in vivo*. The method cannot model higher spatial-resolution aspects without introducing sufficient elements [35]. Further validation is still required to confirm its suitability to reflect actual patient-specific hemodynamic situations, particularly in regards to congenital heart disease patients. A series of patient follow-up studies are being continuously performed in our hospitals. We believe that these *in vivo* data may be available to validate boundary conditions, including the lumped model, in the future.

Local pressure, WSS, streamlines, EL, and FR at the region of TCPC anastomosis were analyzed by calculations at Condition I and Condition II. The results showed that the regional flow patterns within the connection area, which was related to the distribution of local pressure, WSS, and streamlines, differed from those calculated when the influence of respiration was not taken into account, particularly for the size of low-speed areas and local vortical flow. The spatial conformation of the LIV, created in surgery, led the blood to flow directly into the anterior part of the SVC and then into the RPA. Blood flow from the RIV directed to the posterior

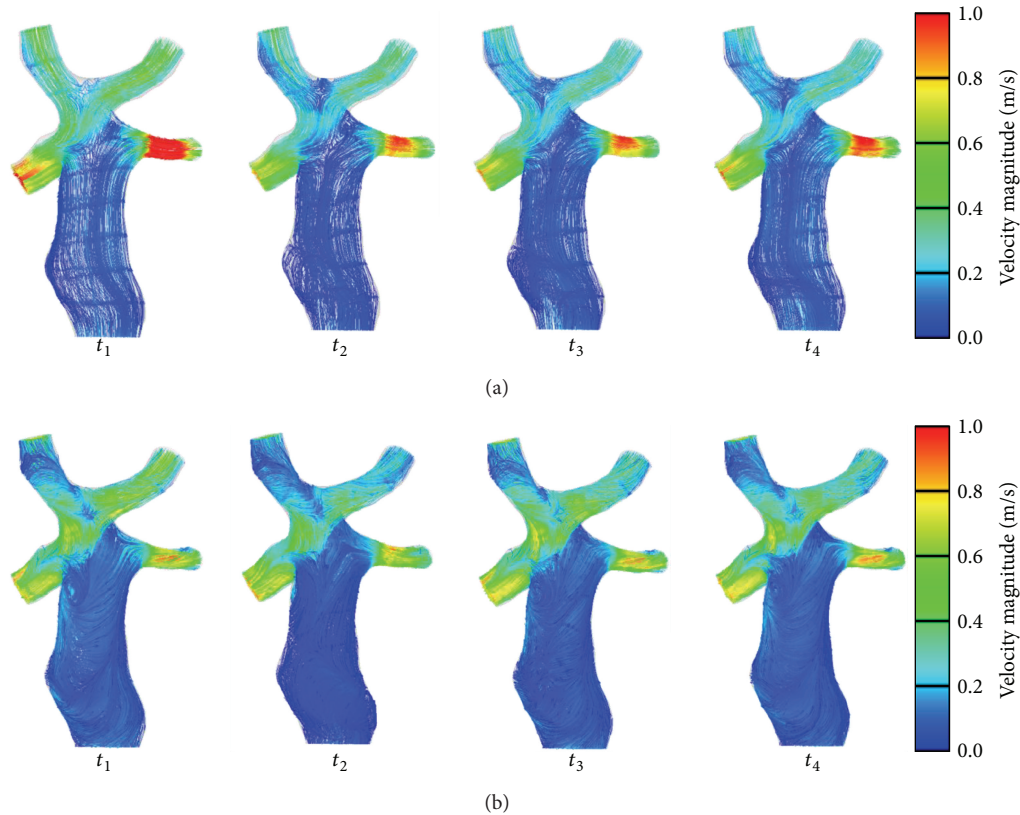


FIGURE 9: Results of streamlines (Condition II (a) and Condition I (b)).

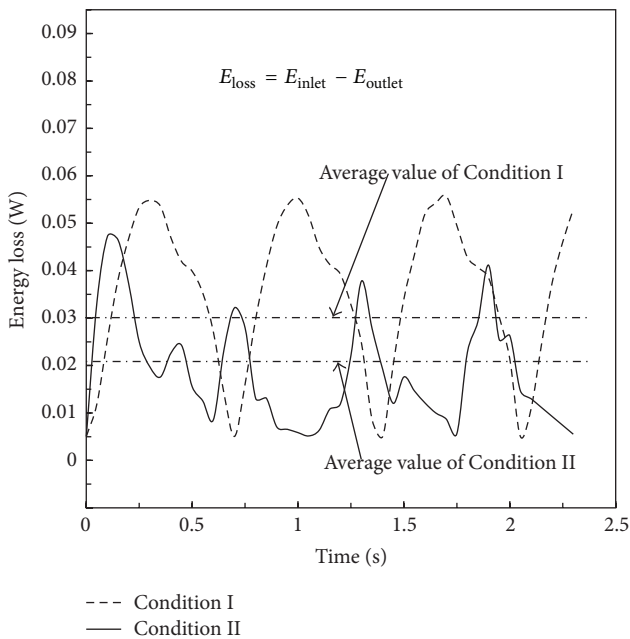


FIGURE 10: Results of energy loss at Condition I and Condition II.

part of SVC and split into the LPA and the RPA. The flow from the IVC interacted with that from the LIV and RIV and then directed into the LPA and RPA. A low-velocity flow

region existed at the LIV-RIV bifurcation, and EL occurred as a result in the area. Moreover, due to the different frequencies between breath and heart beat, the unstable blood flow was shown to be delayed slightly at the IVC at Condition II. This could be explained by the delaying of the peak value at the inlet when respiration was taken into account. Respiration changed the pulsatile periodicity of blood flow. Meanwhile, the intensity of vortical flow at the IVC domain was slightly decreased. The salient part generated in the surgery near the entrance of IVC should be the reason as to why a low-speed area and flow recirculation existed in this region.

We believe that WSS must be discussed at instantaneous conditions. The specific times, selected in this study to compare instantaneous WSS, followed usual cardiovascular applications: systolic peak and diastolic bottom (see Table 1). Furthermore, it is well known that WSS is a vector value. Thus, time-averaged WSS may result in a loss of significance due to alternations of the WSS between positive and negative values.

At conditions of high WSS, the WSS may influence the development of vessels following the TCPC Fontan procedure. The properties of the vessels must be taken into consideration when analysing local hemodynamics. On one hand, WSS also affects normal cardiovascular growth through gene expression [36] and activates blood-forming stem cells [37]. The long-term effects of WSS, on the other hand, include vascular remodeling and endothelial damage. By detailed

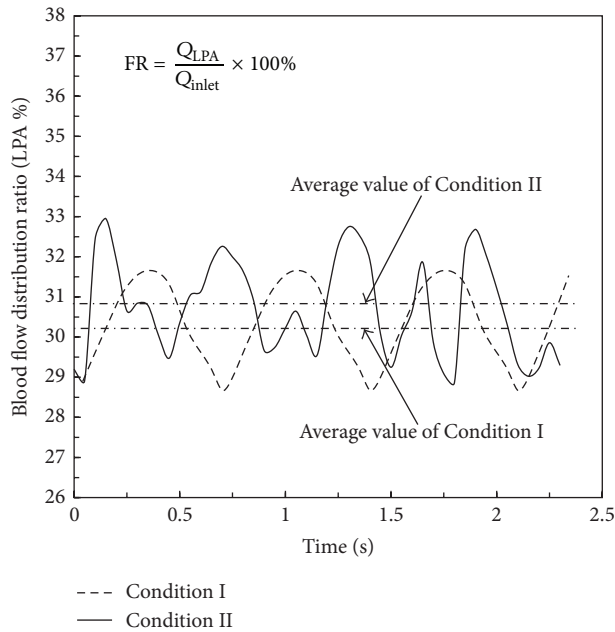


FIGURE 11: Results of flow distribution ratio at Condition I and Condition II at LPA (FR: flow distribution ratio; LPA: left pulmonary artery).

examination of WSS between the two conditions at instantaneous time points, we found that respiration can weaken the effect of WSS on vessel walls. These results indicated that WSS may be overestimated if the calculation fails to consider the influence of respiration in hemodynamic analysis.

In Figure 10, the values of both time-dependent EL and time-averaged EL at Condition II were lower than those at Condition I. One of the possible reasons was that respiration could deliver energy through the transmission of pressure waves. Furthermore, with the influence of respiration, the unstable flow in the confluence region was attenuated, and the direct head-to-head collision of the blood flow from the LIV, RIV, and IVC was decreased. Therefore, relatively low EL was displayed at Condition II, as shown in Figure 10.

The EL was used as an effective indicator in many papers to evaluate the efficiency of the operative designs. In this study, we applied EL to reveal the efficiency of the TCPC connection. When unfavorable vessel connections result in flow separation and collision, EL may exhibit sharp increases. Furthermore, we should emphasize that the EL was calculated at a single pulse. If it was assembled accordingly to days or years, the EL will be of nonnegligible number for the newborn patient. It can be utilized as an indicator to evaluate the outcomes of surgically created Fontan circulation. From a hemodynamic point of view, energy loss fully describes the hemodynamic severity, as well as any impacts on the pumping ventricle. High energy loss thus impacts the pumping ventricle which, together with the peripheral vasculature, adapts itself to work harder to overcome the added drag so as to meet the functions of the circulatory system. Thus, this almost certainly results in chronic heart failure as a secondary

disease [38]. Therefore, EL is a vital factor in the estimation and evaluation of hemodynamic characteristics.

Time-dependent effects of respiration on the FR are shown in Figure 11. Compared with the average value of FR at the two conditions at the LPA, no noticeable difference occurred when the influence of respiration was taken into account. It could be concluded that respiration had little effect on the FR in the patient-specific TCPC study. Whether the influence is universal or not, more patient-specific data is required for examination in future studies. Currently, estimation of FR enables to evaluate the balance of blood flow distribution after Fontan procedure so as to enhance clinical diagnosis for the long-term patient's following therapies.

The important issue of this study was essential for future correlative studies in the design of Fontan-type procedures. The influence of respiration should be considered, especially in the analysis of local hemodynamic characteristics. To estimate quantitative analysis more accurately and make regional flow features approach the realistic conditions, we advocated that the influence of respiration should better be included in numerical simulations.

There are most likely two limitations of the present study which should be considered. Firstly, this study used the rigid vessel model in the calculation of both conditions. Therefore, the interaction of respiration and vessel compliance was not taken into account. Although recent studies illustrated that the method of fluid-structure interaction (FSI) scheme was available [39], the complexity of clinical measurements of vessel properties and the lack of well-established validation methods for FSI simulation are still problems required to be solved in future work. Secondly, the present study was a single patient-specific research. More cases should be investigated in the following studies.

5. Conclusion

Based on the present study, the conclusion could be drawn that the local hemodynamic characteristics at the TCPC connection area were greatly influenced by respiration, including the distribution of static pressure, WSS, and streamlines. Respiration is one of the important physiological factors contributing to the weakening of the effect of WSS on vessel walls and the offset of EL caused by blood flow. However, there was no obvious difference in the time-averaged distribution ratio of blood flow to pulmonary arteries when the influence of respiration was considered. Furthermore, the effects of respiration should better be considered in the correlative studies for the purpose of physiological patient-specific TCPC investigation. Numerical analyses based on in-depth examinations of the physiological flow conditions of patients are required in order to evaluate the outcomes of the Fontan therapy. Considering the results of the current study, greater emphasis should be placed on the influence of respiration during the numerical simulation of TCPC Fontan-type procedures.

In future studies, alongside continual study of the issues mentioned above, our work will also concentrate on the analysis of the influence of respiration and vessel compliance. The method of obtaining this clinical data will be the crucial point in the investigation.

Appendix

Notation

- μ : Dynamic viscosity
 ρ : Density
 τ_{wall} : Wall shear stress
 ΔI : Dimension of grid cell
 Δt : Maximum of time step size
 f_i : Body forces
 i, j : Coordinate axes
 t : Time
 \bar{u} : Time-averaged velocity
 u_i, u_j : Velocity vectors
 C_r : Courant number
 D : Characteristic length
 EL : Energy loss
 FR : Flow distribution ratio
 P : Pressure
 Q : Volume flow rate
 Re : Reynolds number
 U : Velocity vector
 WSS : Wall shear stress.

Acknowledgments

This study has been supported by the Japanese Ministry of Education, Culture, Sports, Science and Technology (MEXT) (no. A09314800; P.I.: Yi Qian), the National Natural Science Foundation of China (no. 81070133; P.I.: Jinfen Liu and no. 81100117; P.I.: Qi Sun), and China Postdoctoral Science Foundation (no. 2013M530200; P.I.: Jinlong Liu).

References

- [1] M. R. De Leval, "The Fontan circulation: what have we learned? what to expect?" *Pediatric Cardiology*, vol. 19, no. 4, pp. 316–320, 1998.
- [2] F. Fontan and E. Baudet, "Surgical repair of tricuspid atresia," *Thorax*, vol. 26, no. 3, pp. 240–248, 1971.
- [3] D. Sedmera, A. C. Cook, G. Shirali, and T. C. McQuinn, "Current issues and perspectives in hypoplasia of the left heart," *Cardiology in the Young*, vol. 15, no. 1, pp. 56–72, 2005.
- [4] H. P. Gutgesell, "What if it were your child?" *American Journal of Cardiology*, vol. 89, no. 7, p. 856, 2002.
- [5] A. A. Kon, L. Ackerson, and B. Lo, "Choices physicians would make if they were the parents of a child with hypoplastic left heart syndrome," *American Journal of Cardiology*, vol. 91, no. 12, pp. 1506–1509, 2003.
- [6] R.-K. Chang, A. Y. Chen, and T. S. Klitzner, "Clinical management of infants with hypoplastic left heart syndrome in the United States, 1988–1997," *Pediatrics*, vol. 110, no. 2 I, pp. 292–298, 2002.
- [7] E. L. Bove, M. R. De Leval, F. Migliavacca, G. Guadagni, and G. Dubini, "Computational fluid dynamics in the evaluation of hemodynamic performance of cavopulmonary connections after the Norwood procedure for hypoplastic left heart syndrome," *Journal of Thoracic and Cardiovascular Surgery*, vol. 126, no. 4, pp. 1040–1047, 2003.
- [8] F. Migliavacca, M. R. De Leval, G. Dubini, and R. Pietrabissa, "A computational pulsatile model of the bidirectional cavopulmonary anastomosis: the influence of pulmonary forward flow," *Journal of Biomechanical Engineering*, vol. 118, no. 4, pp. 520–528, 1996.
- [9] W. Orlando, R. Shandas, and C. DeGroof, "Efficiency differences in computational simulations of the total cavo-pulmonary circulation with and without compliant vessel walls," *Computer Methods and Programs in Biomedicine*, vol. 81, no. 3, pp. 220–227, 2006.
- [10] H.-H. Sievers, A. Gerdes, J. Kunze, and G. Pfister, "Superior hydrodynamics of a modified cavopulmonary connection for the Norwood operation," *Annals of Thoracic Surgery*, vol. 65, no. 6, pp. 1741–1745, 1998.
- [11] K. K. Whitehead, K. Pekkan, H. D. Kitajima, S. M. Paridon, A. P. Yoganathan, and M. A. Fogel, "Nonlinear power loss during exercise in single-ventricle patients after the Fontan: insights from computational fluid dynamics," *Circulation*, vol. 116, no. 11, pp. 1165–1171, 2007.
- [12] M. Rosenthal, A. Bush, J. Deanfield, and A. Redington, "Comparison of cardiopulmonary adaptation during exercise in children after the atriopulmonary and total cavopulmonary connection Fontan procedures," *Circulation*, vol. 91, no. 2, pp. 372–378, 1995.
- [13] E. M. Pedersen, E. V. Stenbøg, T. Fründ et al., "Flow during exercise in the total cavopulmonary connection measured by magnetic resonance velocity mapping," *Heart*, vol. 87, no. 6, pp. 554–558, 2002.
- [14] V. E. Hjortdal, K. Emmertsen, E. Stenbøg et al., "Effects of exercise and respiration on blood flow in total cavopulmonary connection: a real-time magnetic resonance flow study," *Circulation*, vol. 108, no. 10, pp. 1227–1231, 2003.
- [15] A. L. Marsden, I. E. Vignon-Clementel, F. P. Chan, J. A. Feinstein, and C. A. Taylor, "Effects of exercise and respiration on hemodynamic efficiency in CFD simulations of the total cavopulmonary connection," *Annals of Biomedical Engineering*, vol. 35, no. 2, pp. 250–263, 2007.
- [16] A. L. Marsden, V. M. Reddy, S. C. Shadden, F. P. Chan, C. A. Taylor, and J. A. Feinstein, "A new multiparameter approach to computational simulation for Fontan assessment and redesign," *Congenital Heart Disease*, vol. 5, no. 2, pp. 104–117, 2010.
- [17] K. Itatani, K. Miyaji, T. Tomoyasu et al., "Optimal conduit size of the extracardiac Fontan operation based on energy loss and flow stagnation," *Annals of Thoracic Surgery*, vol. 88, no. 2, pp. 565–572, 2009.
- [18] N. Westerhof, G. Elzinga, and P. Sipkema, "An artificial arterial system for pumping hearts," *Journal of applied physiology*, vol. 31, no. 5, pp. 776–781, 1971.
- [19] N. Stergiopoulos, B. E. Westerhof, and N. Westerhof, "Total arterial inertance as the fourth element of the windkessel model," *American Journal of Physiology—Heart and Circulatory Physiology*, vol. 276, no. 1, pp. H81–H88, 1999.
- [20] P. Segers, E. R. Rietzschel, M. L. De Buyzere et al., "Three- and four-element windkessel models: assessment of their fitting performance in a large cohort of healthy middle-aged individuals,"

- Proceedings of the Institution of Mechanical Engineers, Part H*, vol. 222, no. 4, pp. 417–428, 2008.
- [21] N. Westerhof, J.-W. Lankhaar, and B. E. Westerhof, “The arterial windkessel,” *Medical and Biological Engineering and Computing*, vol. 47, no. 2, pp. 131–141, 2009.
- [22] Y. Qian, J. L. Liu, K. Itatani, K. Miyaji, and M. Umezu, “Computational hemodynamic analysis in congenital heart disease: simulation of the norwood procedure,” *Annals of Biomedical Engineering*, vol. 38, no. 7, pp. 2302–2313, 2010.
- [23] G. Taubin, “Signal processing approach to fair surface design,” in *Proceedings of the 22nd Association for Computing Machinery Annual Conference on Computer Graphics and Interactive Techniques*, pp. 351–358, Los Angeles, Calif, USA, August 1995.
- [24] D. A. McDonald, *Blood Flow in the Arteries*, Edward Arnold, London, UK, 1974.
- [25] Y. C. Fung, *Biomechanics: Mechanical Properties of Living Tissues*, Springer, New York, NY, USA, 1981.
- [26] O. Linderkamp, P. Y. K. Wu, and H. J. Meiselman, “Deformability of density separated red blood cells in normal newborn infants and adults,” *Pediatric Research*, vol. 16, no. 11, pp. 964–968, 1982.
- [27] J. A. Long, A. Ündar, K. B. Manning, and S. Deutsch, “Viscoelasticity of pediatric blood and its implications for the testing of a pulsatile pediatric blood pump,” *ASAIO Journal*, vol. 51, no. 5, pp. 563–566, 2005.
- [28] T. F. Mackintosh and C. H. M. Walker, “Blood viscosity in the newborn,” *Archives of Disease in Childhood*, vol. 48, no. 7, pp. 547–553, 1973.
- [29] M. R. De Leval, P. Kilner, M. Gewillig, and C. Bull, “Total cavopulmonary connection: a logical alternative to atriopulmonary connection for complex Fontan operations. Experimental studies and early clinical experience,” *Journal of Thoracic and Cardiovascular Surgery*, vol. 96, no. 5, pp. 682–695, 1988.
- [30] C. Mavroudis and C. L. Backer, *Pediatric Cardiac Surgery*, Mosby, St. Louis, Mo, USA, 3rd edition, 2003.
- [31] S. Prakash and C. R. Ethier, “Requirements for mesh resolution in 3D computational hemodynamics,” *Journal of Biomechanical Engineering*, vol. 123, no. 2, pp. 134–144, 2001.
- [32] F. Migliavacca, P. J. Kilner, G. Pennati et al., “Computational fluid dynamic and magnetic resonance analyses of flow distribution between the lungs after total cavopulmonary connection,” *IEEE Transactions on Biomedical Engineering*, vol. 46, no. 4, pp. 393–399, 1999.
- [33] A. N. Redington, D. Penny, and E. A. Shinebourne, “Pulmonary blood flow after total cavopulmonary shunt,” *British Heart Journal*, vol. 65, no. 4, pp. 213–217, 1991.
- [34] D. J. Penny and A. N. Redington, “Doppler echocardiographic evaluation of pulmonary blood flow after the Fontan operation: the role of the lungs,” *British Heart Journal*, vol. 66, no. 5, pp. 372–374, 1991.
- [35] L. Waite, *Biofluid Mechanics in Cardiovascular Systems*, McGraw-Hill, New York, NY, USA, 2006.
- [36] R. E. Poelmann, A. C. Gittenberger-de Groot, and B. P. Hierck, “The development of the heart and microcirculation: role of shear stress,” *Medical and Biological Engineering and Computing*, vol. 46, no. 5, pp. 479–484, 2008.
- [37] L. Adamo, O. Naveiras, P. L. Wenzel et al., “Biomechanical forces promote embryonic haematopoiesis,” *Nature*, vol. 459, no. 7250, pp. 1131–1135, 2009.
- [38] L. P. Dasi, K. Pekkan, D. De Zelicourt et al., “Hemodynamic energy dissipation in the cardiovascular system: generalized theoretical analysis on disease states,” *Annals of Biomedical Engineering*, vol. 37, no. 4, pp. 661–673, 2009.
- [39] Y. Bazilevs, M.-C. Hsu, D. J. Benson, S. Sankaran, and A. L. Marsden, “Computational fluid-structure interaction: methods and application to a total cavopulmonary connection,” *Computational Mechanics*, vol. 45, no. 1, pp. 77–89, 2009.

Research Article

Preliminary Computational Hemodynamics Study of Double Aortic Aneurysms under Multistage Surgical Procedures: An Idealised Model Study

Yosuke Otsuki,¹ Nhat Bui Minh,² Hiroshi Ohtake,³ Go Watanabe,³ and Teruo Matsuzawa⁴

¹ School of Information Science, Japan Advanced Institute of Science and Technology, 1-1 Asahidai, Nomi, Ishikawa 923-1211, Japan

² Department of Simulation Analysis, Fujitsu Systems East, 1415 Tsuruga Midori, Nagano 380-0813, Japan

³ Department of General and Cardiothoracic Surgery, Graduate School of Medical Science, 13-1 Takara, Kanazawa 920-1192, Japan

⁴ Research Center for Simulation Science, Japan Advanced Institute of Science and Technology, 1-1 Asahidai, Nomi, Ishikawa 923-1211, Japan

Correspondence should be addressed to Yosuke Otsuki; yosuke_otsuki@jaist.ac.jp

Received 2 August 2013; Accepted 19 September 2013

Academic Editors: H.-C. Han, M. Ohta, and A. Qiao

Copyright © 2013 Yosuke Otsuki et al. This is an open access article distributed under the Creative Commons Attribution License, which permits unrestricted use, distribution, and reproduction in any medium, provided the original work is properly cited.

Double aortic aneurysm (DAA) falls under the category of multiple aortic aneurysms. Repair is generally done through staged surgery due to low invasiveness. In this approach, one aneurysm is cured per operation. Therefore, two operations are required for DAA. However, post-first-surgery rupture cases have been reported. Although the problems involved with managing staged surgery have been discussed for more than 30 years, investigation from a hemodynamic perspective has not been attempted. Hence, this is the first computational fluid dynamics approach to the DAA problem. Three idealized geometries were prepared: presurgery, thoracic aortic aneurysm (TAA) cured, and abdominal aortic aneurysm (AAA) cured. By applying identical boundary conditions for flow rate and pressure, the Navier-Stokes equation and continuity equations were solved under the Newtonian fluid assumption. Average pressure in TAA was increased by AAA repair. On the other hand, average pressure in AAA was decreased after TAA repair. Average wall shear stress was decreased at the peak in post-first-surgery models. However, the wave profile of TAA average wall shear stress was changed in the late systole phase after AAA repair. Since the average wall shear stress in the post-first-surgery models decreased and pressure at TAA after AAA repair increased, the TAA might be treated first to prevent rupture.

1. Introduction

An aortic aneurysm is abnormal dilatation on the aortic wall. The formation and growth process are not fully understood although some fundamental biological evidence has been identified [1]. Lasheras stated that repeatedly applied shear force stiffens the aortic wall by changing the biomechanical reaction and when the aneurysm wall strength can no longer tolerate the mechanical load, it ruptures. Moreover, he also mentioned that atherosclerotic plaque was responsible for the growth since it was found in the majority of aneurysms. The death rate due to rupture is high; according to Shek, it reaches 85% if an abdominal aortic aneurysm (AAA) is left untreated [2]. The size of an aneurysm is closely related to

the rupture risk. Choke et al. demonstrated the relationship between the size of AAA and the annual risk of rupture [3]. From their research, the rupture risk increased as the aneurysm diameter increased. Population-based research shows that aneurysms are frequently formed at the aortic arch and abdominal wall [4].

To cure an aneurysm, stent-graft implantation or artificial graft replacement is the common surgical procedure. Since the first procedure is less invasive, it is frequently used. Frauenfelder et al. illustrated the reduction in AAA pressure by stent-graft implantation through their fluid structure interaction model and validation experiment [5].

If more than one aortic aneurysm is found, the condition is called multiple aortic aneurysms (MAA). Crawford and

Cohen reported that 191 of 1510 (12.6%) aneurysm patients were diagnosed as MAA [4]. Yamanaka et al. also reported that 153 of 1750 (8.74%) aneurysm patients had MAA [6]. Two surgical approaches are used for treating MAA: staged surgical treatment or simultaneous surgery. The former repairs each aneurysm by a single operation after a certain recovery period; the latter treats all aneurysms by a single operation. Crawford and Cohen suggested that simultaneous surgery should be used to prevent death due to rupture of the second aneurysm during the recovery period [4]. However, the staged method is generally used because of its high surviving rate [7]. The problem with the staged approach is the management difficulty between operations: rupture of residual aneurysms during this period has been reported. Yamazaki et al. reported TAA rupture after successful AAA stent graft implantation [8] and Ohnishi et al. also reported similar cases [9]. Crawford and Cohen explained that post-operation early death is caused by the second aneurysm rupturing [4]. Normally, surgery priority is determined based on the size of aneurysm and other surgical indications. The indication size is five centimeters in diameter for AAA and six centimeters for TAA. This is a reasonable approach since the size of aneurysm is closely related to the rupture risk. However, Kanamitsu and Yamada explained that AAA repair is generally prioritized since the surgery of TAA alone is high risk [10].

MAA-specific problems can be categorized as follows. First, it is not clear whether TAA or AAA repair should be prioritized. Second, the timing of surgery is determined solely by the size of aneurysm. To clarify these points, computational fluid dynamics was used.

Thanks to the development of diagnostic equipment, information taken from patients can be analyzed before surgery. Blood flow velocity can be measured using magnetic resonance imaging or ultrasound devices. However, crucial information such as pressure and wall shear stress cannot be sampled by these methods. The computational approach enables these variables to be obtained, and *in vivo* conditions can be simulated. From the perspective of hemodynamics, a number of experimental and computational studies for single aneurysms have been conducted. Since aneurysms are found in thoracic and abdominal parts, previous works focused on TAA or AAA [5, 11]. However, there are no reports on MAA.

Hence, the present research had two objectives. The first was to investigate the change in flow pattern, wall shear stress, and pressure distribution after the treatment of AAA and TAA, respectively. The second was to identify, based on these results, the lowest risk-staged surgery for treatment of double aortic aneurysms (DAA). DAA, which has two aneurysms, is the simplest type of MAA. To clarify these factors, three idealized aorta models were prepared.

The models represented the untreated condition before surgery (DAA model), TAA removed condition after the first surgery (AAA cured model), and AAA repaired geometry after the first surgery (TAA cured model). Next, flow was simulated using two pairs of boundary conditions. Then, the results from the postsurgery geometries were compared with the result from the presurgery model.

2. Methods

As discussed, changes in wall shear stress and pressure distribution are considered to be important factors for aneurysms. Therefore, two cases of boundary conditions were used in the present study. The first case was the fixed flow rate boundary condition. Since wall shear stress is a function of only velocity and coordinates, if the inlet flow rate is fixed, a change in wall shear stress is attributed to the geometrical difference under incompressible and the fluid assumption. The second case was the pressure difference boundary condition.

In this method, to investigate the effect of time-dependent pressure inlet and outlet pressure profiles were used. In both cases, calculation was repeated five times.

2.1. Geometry Construction. The model geometries are shown in Figure 1. For the TAA and AAA cured models, the repaired model aneurysm section was straight, assuming stent-graft insertion. The geometries and computation mesh were created using Gambit 2.3.6 (ANSYS Inc.). The aneurysm diameter of 0.055 m (5.5 cm) was determined by Greenhalgh et al. [12] as the surgery criterion for AAA. The aorta diameter of 0.02 m (2 cm) and straight pipe length were determined by Gao et al. [13]. However, an extra length of 0.1 m (10 cm) was added to the inlet. The arch diameter of 0.13 m (13 cm) was determined by the double aortic aneurysm geometry reconstructed from computed tomography data. At the intersection edge of the straight model artery and the aneurysm, a fillet of 0.005 m (0.5 cm) was applied. All aortic branches were ignored. The locations of the aneurysms were determined in the aortic arch and abdominal part according to Crawford and Cohen [4]. A tetrahedron mesh was created using Gambit. The mesh characteristic size was set to 0.001 m (0.1 cm). The number of elements was 80103, 71748, and 69342 for the DAA, TAA cured, and AAA cured model, respectively.

2.2. Computational Fluid Dynamics (CFD). For the simulation, the commercial CFD package Fluent 14.5 (ANSYS Inc.) was used. The Navier-Stokes and continuity equations were discretized by the finite volume method assuming Newtonian laminar flow and were solved. For density and viscosity, 1050 kg m^{-3} and $0.0035 \text{ N m}^{-1} \text{ s}^{-1}$ were assigned.

2.3. Boundary Condition. As explained earlier, the fixed flow rate and fixed pressure boundary conditions were simulated to observe changes in wall shear stress and pressure after the first surgery.

Therefore, two pairs of boundary conditions were prepared. First, the inflow rate profile was obtained from Tse et al. [14], and the pressure profile from Olfusen et al. [15] was used for wall shear stress analysis. The pressure curve at the inlet was sampled and then was used as the boundary condition for the fixed pressure calculation. The pressure was sampled at the centre of the inlet. The spatial variation on the inlet cross-section was negligible. The flow rate and pressure curve are shown in Figures 2 and 3, respectively. The calculated pressure wave profile at the inlet and the outlet pressure profile are shown in Figure 4. To sample inlet pressure curve,

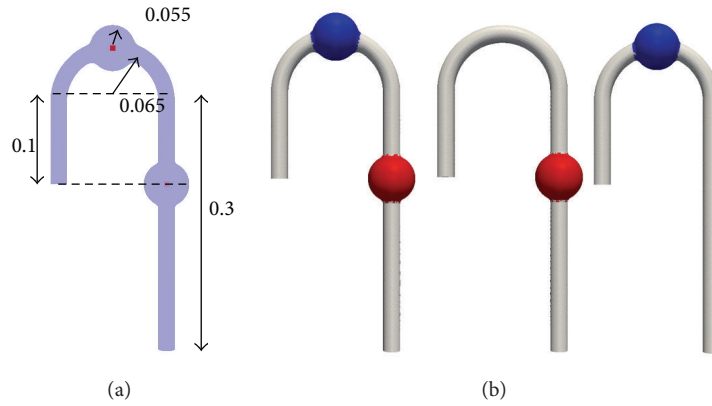


FIGURE 1: DAA (left), TAA cured (centre), and AAA cured (right) geometries, red: abdominal aortic aneurysm, blue: thoracic aortic aneurysm. Inlet: left, outlet: right, all dimensions in meter.

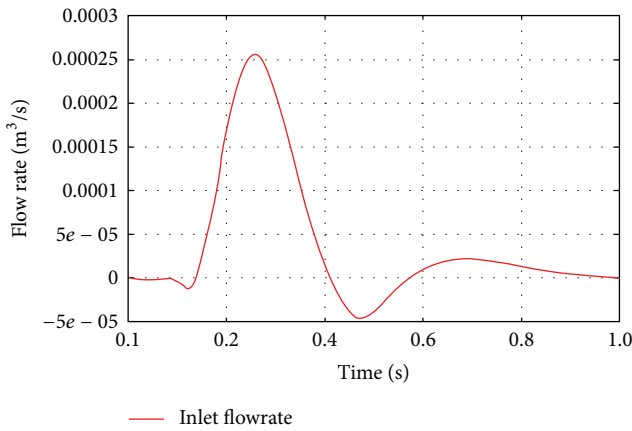


FIGURE 2: Inlet flow rate profile for flow rate fixed simulation.

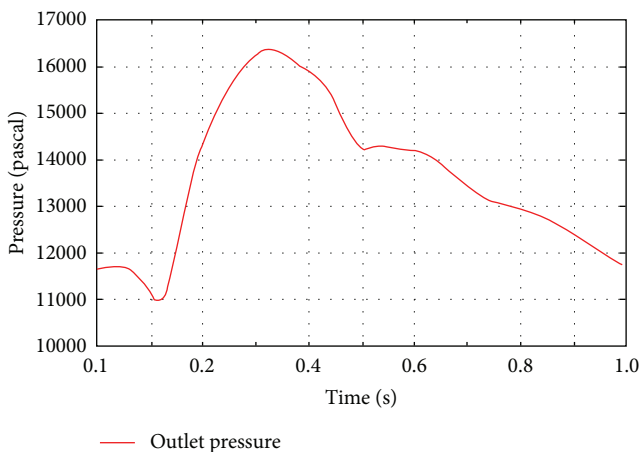


FIGURE 3: Outlet pressure profile.

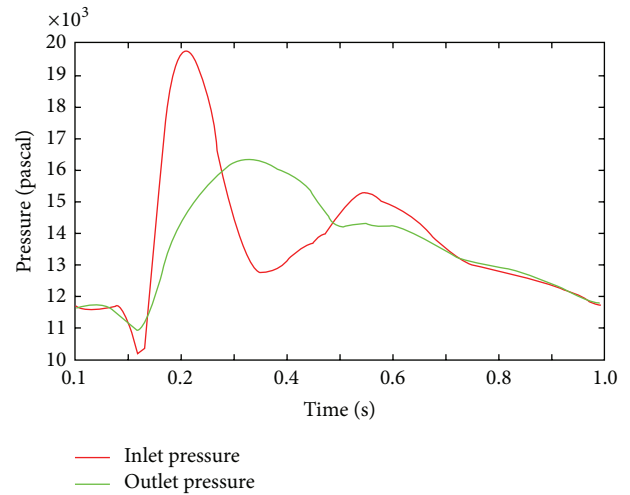


FIGURE 4: Calculated inlet pressure profile (red) and outlet profile (green) for pressure fixed simulation.

3. Result

The velocity vector and wall shear stress from the fixed flow rate model boundary condition and the pressure sampled from the fixed pressure difference boundary condition are shown. For the flow pattern analysis, the results from the fixed flow rate and fixed pressure boundary conditions will be presented. For the analysis of wall shear stress, the results were taken from the fixed flow rate case, and for the analysis of pressure, the pressure difference boundary condition results were used. The average Reynolds number was 925 and the maximum Reynolds number was 4880 according to the flow rate profile and the geometry. The calculation result was taken from the fifth cycle ($t = 4.0-5.0$ s).

the DAA model was used. In Figure 4, the red line indicates the calculated pressure and the green line represents the outlet pressure. These curves were uniformly applied at the inlet and outlet planes.

3.1. Velocity. In the early and late systole phases, vortices were created in TAA and AAA. When the flow accelerated, vortices disappeared. The velocity magnitude was smaller in an aneurysm than in the straight artery section. Figure 5

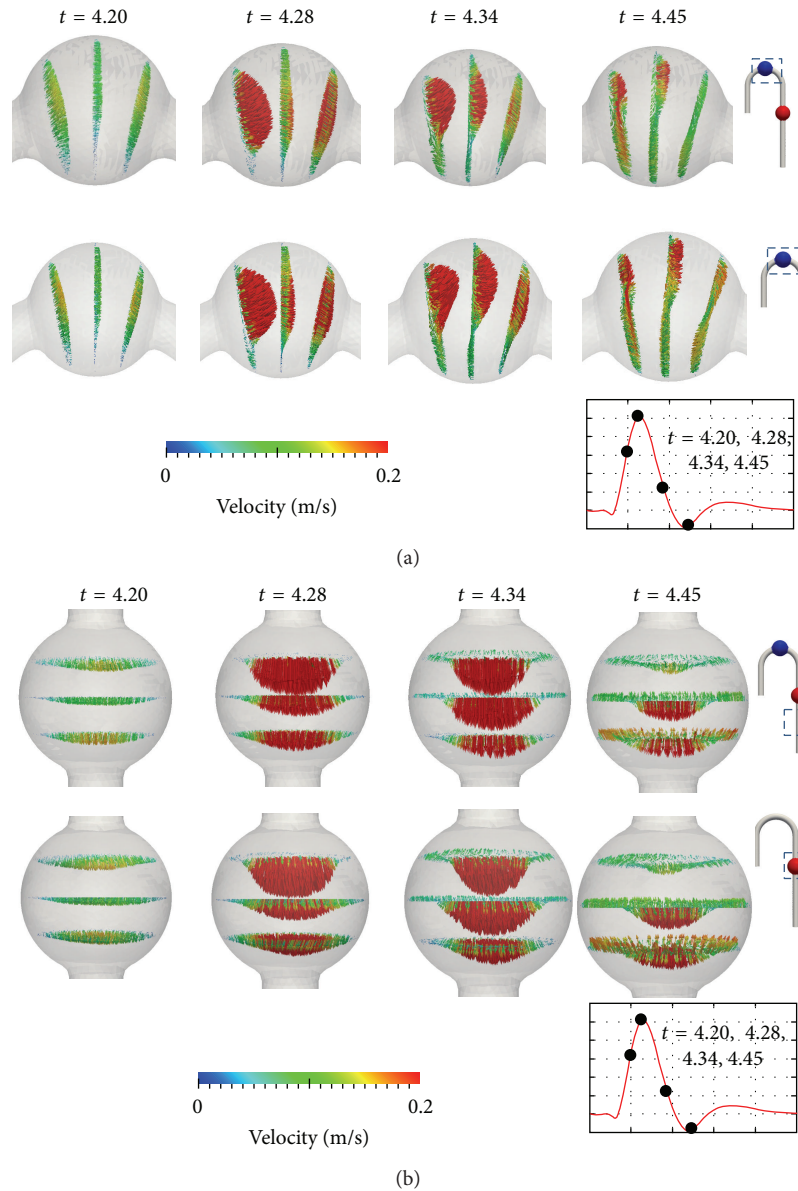


FIGURE 5: Velocity vector in aneurysms: (a) TAA in DAA model versus TAA in AAA cured model, (b) AAA in DAA model versus TAA cured model.

plots the velocity vector in aneurysms. The figure uses the fixed flow rate boundary condition to demonstrate the relationship with the distribution of wall shear stress. The colour of the vector illustrates the magnitude of velocity. The images were taken at $t = 4.20, 4.28, 3.34,$ and 4.45 s. These represent early systole, peak, late systole, and backflow phases. For the TAA flow pattern in the DAA and AAA cured models, there was no vortex during the acceleration. In the early and the late systole phase, vortices were created in TAA and AAA. When the flow accelerated, vortices disappeared. In aneurysm, the velocity magnitude was slower than the straight tube section. As shown in Figure 5(a), there is no backflow or vortex at $t = 4.28$ s. As the velocity decreased, a clockwise vortex was formed in TAA. At this time step, the flow entered the aneurysm from the outer aortic arch

($t = 4.34$ s in Figure 5(a)). A small backflow was initiated on the inner aortic arch wall, and the backflow velocity magnitude gradually increased after the peak. As shown in Figure 5(a), the circulation velocity magnitude at this time step was larger in the AAA cured model than in the DAA model. For AAA flow in the DAA and TAA cured models, almost symmetrical vortices were found for most time steps. Figure 5 shows that, at $t = 4.34$ s, flow faster than 0.2 m s^{-1} was more concentrated at the central path in the DAA model than in the TAA cured model. At $t = 4.34$ and 4.45 s, backflow near the wall can be observed in both the AAA in DAA and in TAA cured models. However, the symmetry was temporarily destroyed at the initial backflow, which can be confirmed from the velocity vector plot at $t = 4.45$ s in the TAA cured model.

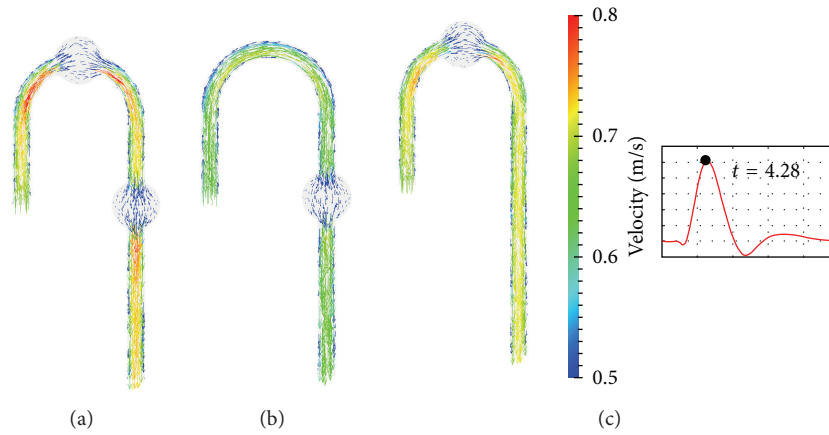


FIGURE 6: Peak velocity on DAA, TAA cured, and AAA cured middle plane DAA (a), TAA cured (b), and AAA cured (c).

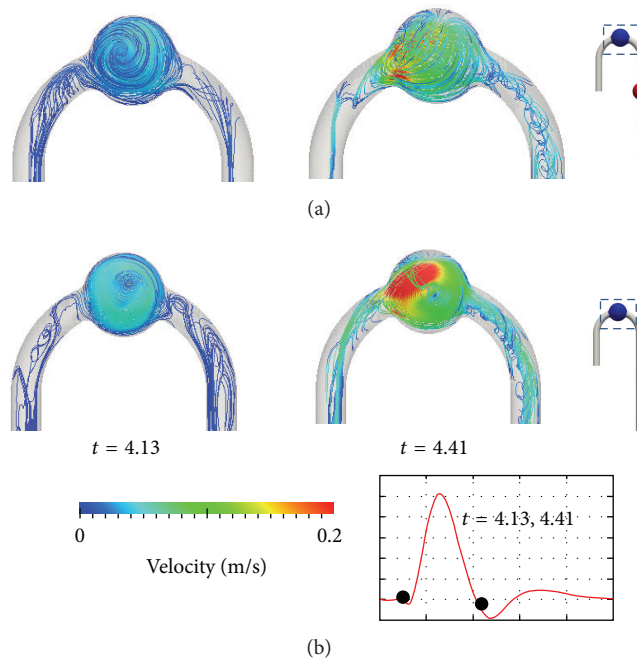


FIGURE 7: Helical flow at ascending and descending aorta $t = 4.13$ and $t = 4.41$ second: (a) DAA, (b) TAA cured (right).

To observe the geometrical effects on the flow, the velocity vector plot on the middle planes of the model is illustrated in Figure 6. The figure was taken at the velocity peak $t = 4.28$ s. The colour illustrates the magnitude of velocity. The flow velocity magnitude in the cured models was clearly slower than in the DAA model. The slowest flow speed was found in the AAA cured model. The TAA cured model had the second largest velocity magnitude at the peak. However, at the mid-to-late systole phase, the velocity magnitude in the TAA cured and AAA cured models increased, and a larger increase was found in the TAA model. Fast flow was found at the inner wall of the aortic arch for all models. The velocity magnitude of the AAA cured model was the smallest in this section. Figure 7 depicts helical flow by streamline plots; color illustrates the magnitude of velocity. At both $t = 4.13$ and

4.41 s, fast circulation flow was found in TAA. At $t = 4.41$ s, there was a difference of over 0.2 m s^{-1} in the region near the inlet. Helical flow was observed at the ascending and descending aorta, which is a known characteristic for the aortic arch flow [16].

Furthermore, the flow was observed several time steps before the acceleration of velocity.

3.2. Pressure. Average pressure was calculated to evaluate rupture risk. Pressure was sampled from the colored area in Figure 1. The number of sampling points was 4468 and 4548 for TAA and AAA in the DAA model, respectively. For the AAA cured and TAA cured models, the number was 5060 and 4818 points, respectively. The aneurysm sections had identical surface area. However, because of the difference in sampling

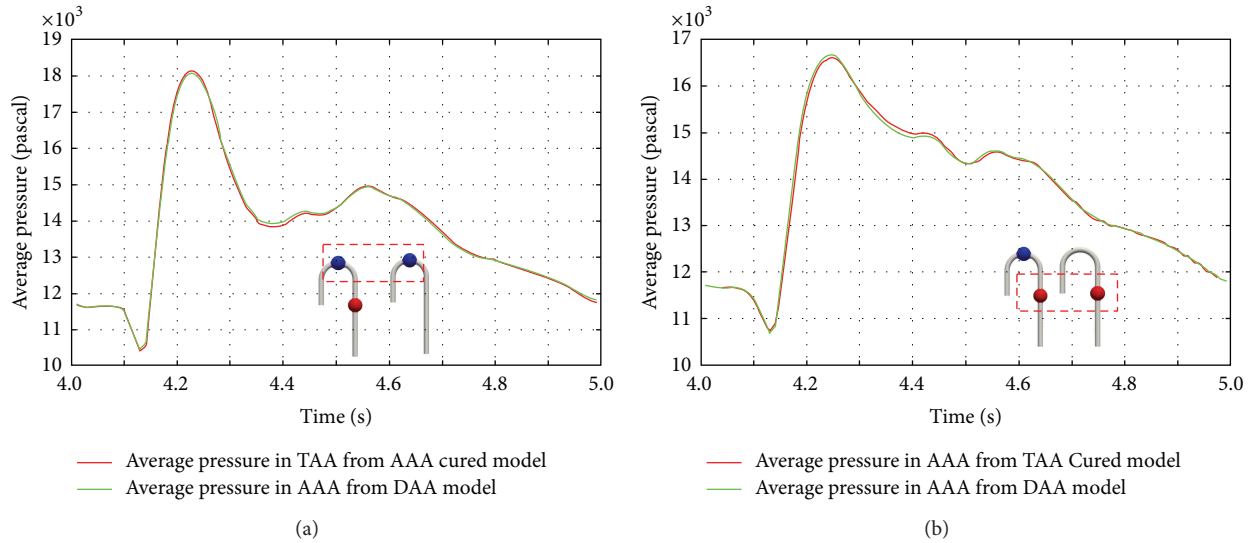


FIGURE 8: Pre- and post-first-surgery average pressure change in aneurysms: (a) average pressure comparison in TAA, (b) average pressure comparison in AAA.

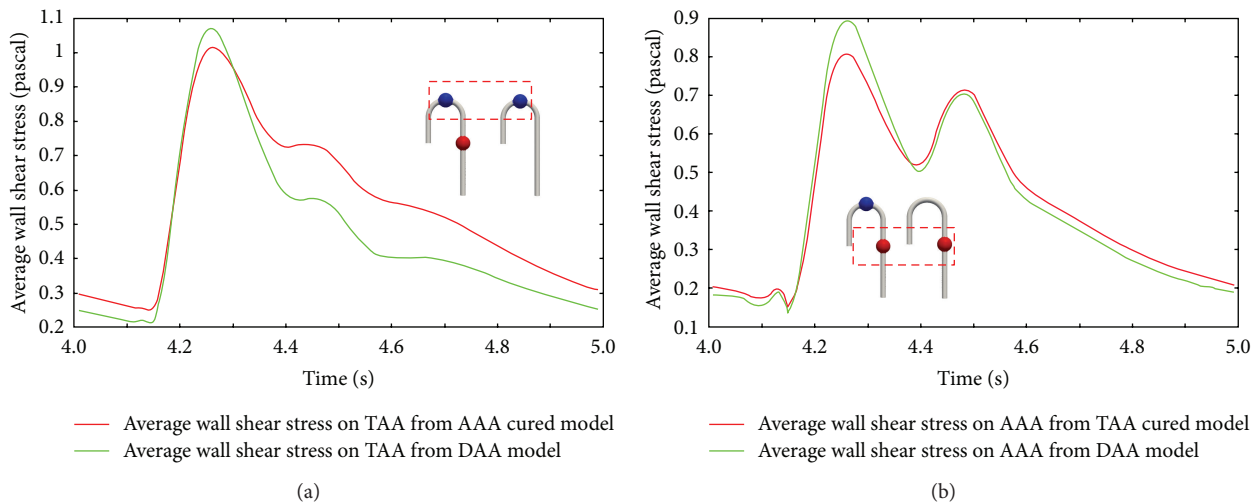


FIGURE 9: Average wall shear stress per cycle: (a) average wall shear stress comparison in TAA, (b) average wall shear stress comparison in AAA green line. Presurgery double aneurysms, red line: post surgery TAA cured or AAA cured.

node number averaging was required. The change in average pressure in the aneurysm sections is illustrated in Figure 8. In the figure, the red line represents average pressure from DAA mode and the green line illustrates that from AAA model (a)/TAA model (b). A comparison of pre- and postsurgery TAA pressure in Figure 8 indicates that the average pressure increases at $t = 4.23$ s in the AAA cured geometry. Moreover, at $t = 4.38$ s, the TAA pressure in the AAA cured model decreased. Therefore, the magnitude of the pressure wave increased after AAA repair. On the other hand, in the TAA cured model, the AAA pressure decreased at $t = 4.25$ s. Another notable change was between $t = 4.3$ and 4.4 s, when the average pressure in the AAA cured model was smaller than that in the DAA model. The quantitative difference after repair was as follows. For TAA, the increase in pressure was

measured to be about 0.8% at the average pressure peak. For AAA, the decrease in pressure was about 0.8% at the average pressure peak. However, the largest pressure change was found at the slope just after the average pressure peak. A decrease of about 1.0% was found from TAA in the AAA cured model, and the figure from AAA in the TAA cured model showed an increase of 1.0%.

3.3. Wall Shear Distribution. Wall shear distribution contours were taken from the fixed flow rate simulation. Figure 9 shows the average wall shear stress on the TAA surface. The green line represents the average wall shear stress taken from the DAA model, and the red line demonstrates that from the AAA cured model. The sampling sections are coloured in Figure 1. From Figure 9, a comparison between the DAA and

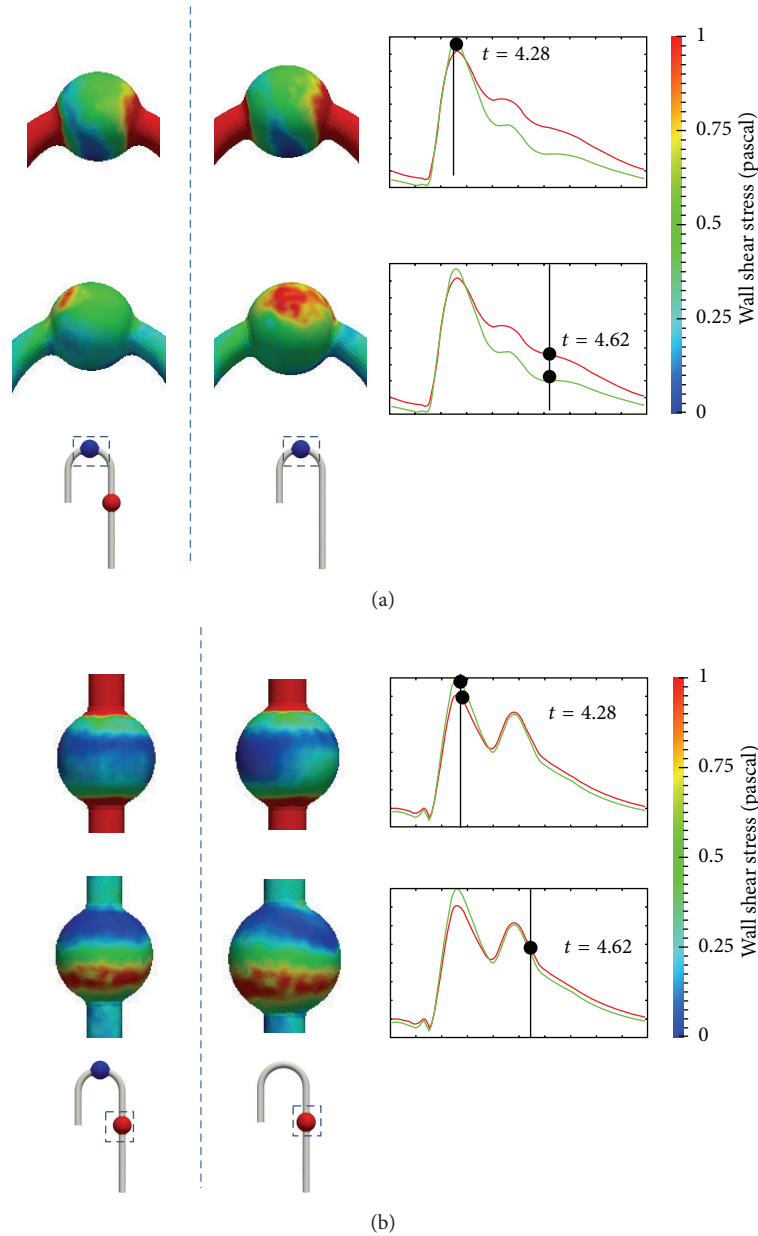


FIGURE 10: Wall shear stress contour comparison: (a) TAA, (b) AAA.

AAA cured models shows a drop in average wall shear stress in the AAA cured model at the peak of $t = 4.28$ s. In contrast, average wall shear stress increased after the peak. Similarly, regarding AAA in the DAA and TAA cured models, the average wall shear stress decreased at the peak but increased in the mid-to-late systole phases. By comparing the average wall shear stress taken from TAA and AAA, a larger increase in wall shear stress was found in TAA in the AAA cured model.

Furthermore, the late systole wave profile implies that the wall shear stress wave profile differed from that of DAA. Figure 10 compares the wall shear stress contours at $t = 4.28$ and $t = 4.62$ s. The colour in the figure represents the magnitude of wall shear stress. A comparison of the

distribution of TAA wall shear stress from the DAA and AAA cured models reveals a notable difference in the wall shear stress pattern. From TAA in the AAA cured model, a region of wall shear stress of over 1.0 Pa was found in the late systole phase at $t = 4.62$ s. The location was on the wall surface of the inner aortic arch. The wall shear stress of the inner aortic arch was similar in magnitude to that from DAA. The wall shear stress region from the DAA model was around 0.5 Pa. In addition, from the DAA and AAA cured models, a low stress point was found near the TAA center. This location was identical to the center of the vortex. The point movement path is illustrated in Figure 11.

In the AAA wall shear stress distribution, a change in wall shear stress distribution of the posterior side was found

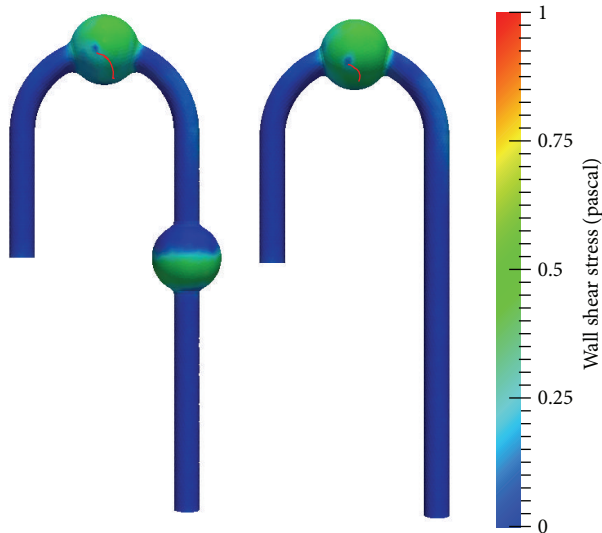


FIGURE 11: Low wall shear stress point movement path (red line), left: DAA, right: AAA cured.

although the difference between the DAA and TAA cured models was small. A comparison of AAA in the DAA and TAA cured models reveals that the symmetry of wall shear distribution was lost after TAA repair. At most time steps, the wall shear stress of the posterior side was not equivalent to that of the anterior side in the TAA cured model. At the late systole phase, both the DAA and TAA cured wall shear distributions show a low wall shear stress area from the inlet to the middle of the aneurysm. The region moved downstream during the midsystole phase.

4. Discussion

Figure 6 shows that the velocity magnitude in the aneurysm cured models was slower than that in the DAA model at the peak. This is a reasonable result since shear stress is a function of the first derivative of velocity with respect to the distance from the wall, and the viscosity was assumed to be constant in this simulation. If an aneurysm that has a larger diameter than the mother vessel is removed, the distance to the wall must be reduced. In other words, the removal of the aneurysm increases the resistive force. The increase in velocity magnitude in the mid-to-late systole phase was considered to be the cause of the increase in wall shear stress. Figure 5 at $t = 4.45$ s demonstrates the loss of symmetry after TAA repair. It is considered that the vortex in TAA acted as a mixer or diffuser. In AAA in TAA cured model, the convective effect became larger and the flow symmetry was destroyed.

A comparison of the average aneurysm pressure revealed an increase in pressure at TAA in the AAA cured model. Moreover, the magnitude of the TAA pressure wave increased over the cycle. The authors believe that this may lead to post-surgery TAA failure since an aneurysm rupture is considered to be due to mechanical failure. If this assumption is correct,

an increase in pressure peak has the largest possibility of rupture.

A comparison of average wall shear stress in TAA and AAA showed a decrease in the peak and an increase in the late systole phase. A notable change was found at TAA in the AAA cured model, and the increase in average wall shear stress was larger than that at AAA in the TAA cured model. An increase in velocity magnitude after the velocity peak in the TAA and AAA cured models was also confirmed. Moreover, the mid-to-late systole average wall shear stress wave profile changed at TAA in the AAA cured model. From a biomechanics perspective, it is known that the receptor reaction is triggered by a change in wall shear stress distribution and causes solidification of the vessel. Therefore, TAA in the AAA cured model is considered to be a larger risk than AAA in the TAA cured model. A comparison between Figures 5 and 10 demonstrates that the high wall shear stress region matches the region of larger velocity magnitude. For example, when the flow decelerated, the region of larger velocity magnitude moved to the outer aortic arch wall. Regarding the spatial gradient of wall shear stress in TAA, the wall shear stress of the inner aortic arch was smaller than that of the outer aortic arch for all time steps.

Furthermore, from Figure 11, the low wall shear stress area was found in the center of TAA from the DAA and AAA cured models. The point moved and joined the inner small wall shear stress region just before the acceleration of flow. Since the small shear stress region is closely linked with the accumulation of thrombus [17], this process may work negatively.

Thrombus collected at the center of TAA and moved toward the inner arch wall area and accumulation started there. In addition, Boussel et al. reported the correlation between small wall shear stress area and aneurysm growth [18]. Therefore, for the long term, attention should be paid to the section. In AAA, the wall shear stress near the inlet was smaller than that near the outlet, and the anterior side wall had slightly larger wall shear stress than the posterior side wall. The difference between wall shear stress in the anterior and posterior walls was smaller than that in the inlet and outlet walls. As discussed, the pressure and wall shear stress results suggest an increase in rupture risk in TAA after treatment of AAA, although it is difficult to predict and specify which of the two will trigger this.

There are some limitations in this work. The distribution of inlet velocity was assumed to be uniform, but it is asymmetric in reality. Renner et al. [19] pointed out this problem through simulation from three boundary configurations. In their work, MRI-captured actual velocity distribution, uniform distribution, and parabolic distribution were used to investigate the change in wall shear stress distribution.

To simplify the simulation and to clearly observe the difference in poststent implanted condition, the geometries were assumed to be rigid. If an elastic model is used, a wave shift might be found by fluid and structure coupling effects.

Furthermore, the sizes of TAA and AAA were assumed to be identical to simplify the problem. However, the volume, shape, and location of the geometries differ for each patient.

Moreover, the poststent implanted condition was modelled by straight tube. In reality, the surface of the artery is covered by fabric and metal mesh. Therefore, disturbance of the flow cannot be eradicated as demonstrated in this model study.

5. Conclusion

To investigate the postsurgery rupture of double aortic aneurysms, changes in pressure and wall shear distribution were investigated under fixed flow rate and pressure difference boundary conditions. The average pressure sampling results revealed that pressure increased at TAA after AAA repair. In contrast, AAA pressure dropped in the TAA cured model. The average wall shear stress demonstrated a decrease at the peak. However, an increase in wall shear stress was found in the late systole phase. In addition, a larger increase was found at TAA in the AAA cured model than that at AAA in the TAA cured model. The calculated average wall shear stress curve differed from the curve for TAA in the DAA model. Since aneurysm rupture is considered to be a mechanical failure, it is reasonable to estimate that rupture is triggered when the maximum load is applied to the structure. Therefore, an increase in average pressure may be one cause of rupture.

Moreover, the increase and change in average wall shear stress curve for TAA in the AAA cured model are also considered to be a cause of rupture in the long term since a change in wall shear stress waveform triggers a biomechanical reaction and solidifies the artery. A less flexible artery is easily damaged. Hence, both the calculated pressure and wall shear stress suggest that the risk of TAA rupture is increased after AAA treatment. Moreover, since AAA pressure decreased and there was a significant difference in the average wall shear stress after TAA repair, TAA treatment should be prioritised.

Acknowledgment

This work was partly supported by Grants-in-Aid for Scientific Research, Scientific Research (C) (General), ID 24591871 from Japan Society for the Promotion of Science.

References

- [1] J. C. Lasheras, "The biomechanics of arterial aneurysms," *Annual Review of Fluid Mechanics*, vol. 39, pp. 293–319, 2007.
- [2] L. T. T. Shek, *Computational fluid dynamics (CFD) evaluation of non-planar stent graft configurations in endvascular aneurysm repair (EVAR)* [Ph.D. thesis], Institution of Biomaterial and Biomedical Engineering, University of Toronto, 2011.
- [3] E. Choke, G. Cockerill, W. R. W. Wilson et al., "A review of biological factors implicated in abdominal aortic aneurysm rupture," *European Journal of Vascular and Endovascular Surgery*, vol. 30, no. 3, pp. 227–244, 2005.
- [4] E. S. Crawford and E. S. Cohen, "Aortic aneurysm: a multifocal disease," *Archives of Surgery*, vol. 117, no. 11, pp. 1393–1400, 1982.
- [5] T. Frauenfelder, M. Lotfey, T. Boehm, and S. Wildermuth, "Computational fluid dynamics: hemodynamic changes in abdominal aortic aneurysm after stent-graft implantation," *CardioVascular and Interventional Radiology*, vol. 29, no. 4, pp. 613–623, 2006.
- [6] J. Yamanaka, Y. Okita, S. Takamoto, M. Ando, T. Morota, and R. Matsukawa, "Problem in staged operation for multiple thoracic and abdominal aortic aneurysms," *Japan Journal of Vascular Surgery*, vol. 7, pp. 503–506, 1998.
- [7] P. Gloviczki, P. Pairolero, T. Welch et al., "Multiple aortic aneurysms: the results of surgical management," *Journal of Vascular Surgery*, vol. 11, no. 1, pp. 19–28, 1990.
- [8] Y. Yamazaki, H. Kanazawa, M. Ueno et al., "Aortic arch replacement performed in emergency in a short-term after grafting for abdominal aortic aneurysm," *Kyobu Geka*, vol. 50, no. 12, pp. 1032–1036, 1997.
- [9] H. Ohnishi, H. Ohteki, K. Furukawa, Y. Takeda, and Y. Narita, "Surgical treatment of multiple aortic aneurysm," *Kyobu Geka*, vol. 52, no. 13, pp. 1069–1072, 1999.
- [10] H. Kanamitsu and Y. Yamada, "A case of double in ammatory aneurysms in the thoracic and abdominal aorta repaired simultaneously," *Annals of Vascular Diseases*, vol. 3, no. 1, pp. 81–83, 2010.
- [11] M. Midulla, R. Moreno, A. Baali et al., "Haemodynamic imaging of thoracic stent-graft by computational fluid dynamics (CFD): presentation of a patient-specific method combining magnetic resonance imaging and numerical simulations," *European Radiology*, vol. 22, pp. 2094–2102, 2012.
- [12] R. M. Greenhalgh, L. C. Brown, G. P. Kwong, and J. T. Powell, "Comparison of endvascular aneurysm repair with open repair in patient with abdominal aortic aneurysm (EVAR trial 1), 30-day operative mortality results: randomised controlled trial," *The Lancet*, vol. 364, pp. 843–848, 2004.
- [13] F. Gao, M. Watanabe, and T. Matsuzawa, "Stress analysis in a layered aortic arch model under pulsatile blood flow," *BioMedical Engineering*, vol. 5, article 25, pp. 1–11, 2006.
- [14] K. M. Tse, P. Chiu, H. P. Lee, and P. Ho, "Investigation of hemodynamics in the development of dissecting aneurysm within patient-specific dissecting aneurysmal aortas using computational fluid dynamics (CFD) simulations," *Journal of Biomechanics*, vol. 44, no. 5, pp. 827–836, 2011.
- [15] M. S. Olfusen, C. S. Peskin, W. Y. Kim, E. M. Pedersen, A. Nadim, and J. Larsen, "Numerical simulation and experimental validation of blood flow in arteries with structured-tree outflow conditions," *Annals of Biomedical Engineering*, vol. 28, no. 11, pp. 1281–1299, 2000.
- [16] P. J. Kilner, G. Z. Yang, R. H. Mohiaddin, D. N. Firmin, and D. B. Longmore, "Helical and retrograde secondary flow patterns in the aortic arch studied by three-directional magnetic resonance velocity mapping," *Circulation*, vol. 88, no. 5, pp. 2235–2247, 1993.
- [17] A. Harloff, A. Nussebaumer, S. Bauer et al., "In vivo assessment of wall shear stress in the atherosclerotic aorta using flow-sensitive 4D MRI," *Magnetic Resonance in Medicine*, vol. 63, no. 6, pp. 1529–1536, 2010.
- [18] L. Bousset, V. Rayz, C. McCulloch et al., "Aneurysm growth occurs at region of low wall shear stress: patient-specific correlation of hemodynamics and growth in a longitudinal study," *Stroke*, vol. 39, no. 11, pp. 2997–3002, 2008.
- [19] J. Renner, D. Loyd, T. Länne, and M. Karlsson, "Is a flat inlet profile sufficient for WSS estimation in the aortic arch?" *WSEAS Transactions on Fluid Mechanics*, vol. 4, no. 4, pp. 148–160, 2009.

Research Article

Transient Hemodynamic Changes upon Changing a BCPA into a TCPC in Staged Fontan Operation: A Computational Model Study

Fuyou Liang,¹ Hideaki Senzaki,² Zhaofang Yin,³ Yuqi Fan,³
Koichi Sughimoto,⁴ and Hao Liu^{1,5}

¹ SJTU-CU International Cooperative Research Center, School of Naval Architecture, Ocean and Civil Engineering, Shanghai Jiao Tong University, 800 Dongchuan Road, Shanghai 200240, China

² Department of Pediatrics and Pediatric Cardiology, Saitama Medical Center, Saitama Medical University, Staff Office Building 101, 1981 Kamoda, Kawagoe, Saitama 3508550, Japan

³ Department of Cardiology, Shanghai Ninth People's Hospital, Shanghai Jiao Tong University School of Medicine, 639 Zhizaoju Road, Shanghai 200011, China

⁴ Department of Cardiac Surgery, Royal Children's Hospital, 50 Flemington Road, Parkville Victoria, Melbourne, VIC 3052, Australia

⁵ Graduate School of Engineering, Chiba University, 1-33 Inage, Chiba 2638522, Japan

Correspondence should be addressed to Fuyou Liang; fuyouliang@sjtu.edu.cn

Received 2 August 2013; Accepted 19 September 2013

Academic Editors: M. Ohta and A. Qiao

Copyright © 2013 Fuyou Liang et al. This is an open access article distributed under the Creative Commons Attribution License, which permits unrestricted use, distribution, and reproduction in any medium, provided the original work is properly cited.

The clinical benefits of the Fontan operation in treating single-ventricle defects have been well documented. However, perioperative mortality or morbidity remains a critical problem. The purpose of the present study was to identify the cardiovascular factors that dominate the transient hemodynamic changes upon the change of a bidirectional cavopulmonary (Glenn) anastomosis (BCPA) into a total cavopulmonary connection (TCPC). For this purpose, two computational models were constructed to represent, respectively, a single-ventricle circulation with a BCPA and that with a TCPC. A series of model-based simulations were carried out to quantify the perioperative hemodynamic changes under various cardiovascular conditions. Obtained results indicated that the presence of a low pulmonary vascular resistance and/or a low lower-body vascular resistance is beneficial to the increase in transpulmonary flow upon the BCPA to TCPC change. Moreover, it was found that ventricular diastolic dysfunction and mitral valve regurgitation, despite being well-known risk factors for poor postoperative outcomes, do not cause a considerable perioperative reduction in transpulmonary flow. The findings may help physicians to assess the perioperative risk of the TCPC surgery based on preoperative measurement of cardiovascular function.

1. Introduction

The Fontan operation is a surgical procedure performed in patients with complex congenital heart disease that cannot be treated by a biventricular repair [1]. Since the first proposal in 1971 [2], the operation has been undergoing modifications, such as introduction of staged operation strategy, refinement in pre- and post-Fontan management, and optimization of cavopulmonary connection configuration [1]. These modifications have contributed significantly to a continuous improvement of clinical outcomes in the past decades.

For example, the long-term (>10 years) survival rate has been increased from 60–70% (before 1985) to 80–90% [3–5]. Moreover, the technical advancements have enabled the extension of the operation to high-risk patients [6].

Despite the overall favorable clinical manifestations, the operation remains to be further improved, particularly in the perioperative stage. A follow-up study revealed that perioperative mortality accounted for 68.4% of all deaths [5]. Another study showed that the rate of early death in high-risk patients reached over 10%, due primarily to low cardiac output syndrome [6]. Population-based studies have allowed

identification of many factors associated with poor clinical outcomes, such as low ventricular ejection fraction [7], high pulmonary vascular resistance [8, 9], atrioventricular valve regurgitation [6, 8], and ventricular diastolic dysfunction [10, 11]. The hemodynamic effect of a specific factor is, however, difficult to be quantified by clinical measurements because under in vivo conditions multiple factors always interact to determine the overall hemodynamic conditions in the cardiovascular system. At this point, computational modeling of the cardiovascular system may offer a useful complementary tool for clinical studies. In the literature, computational models have been widely used to provide quantitative insights into hemodynamic phenomena of interest [12–14], including those related to the Fontan operation [15–18].

In the present study, we developed a set of computational models to account for the hemodynamic characteristics of a single-ventricle circulation in different stages of Fontan operation: (1) in the second stage with a bidirectional cavopulmonary (Glenn) anastomosis (BCPA) and (2) in the final stage with a total cavopulmonary connection (TCPC). The models were used to quantify the transient changes in hemodynamic variables, such as central venous pressure and oxygenated flow (i.e., flow through the pulmonary circulation) upon the change of a BCPA into a TCPC. In particular, we carried out a series of simulations under various cardiovascular conditions, with the aim of identifying the cardiovascular factors that dominate perioperative hemodynamic changes.

2. Materials and Methods

2.1. Model Development. A single-ventricular circulation with a BCPA was firstly modeled using the lumped parameter modeling method. In the model, the pulmonary circulation was divided into the left and right parts, with each part being further divided into three serially arranged compartments that represent the arterial, capillary, and venous vascular portions, respectively (see Figure 1(a)). The systemic vascular system was divided into aorta, vena cava, and two parallel-arranged upper-body (including the head and the upper limbs) and lower-body (including the splanchnic organs and the lower limbs) subsystems. The properties of each vascular portion were accounted for by three parameters (namely, resistance (R), compliance (C), and inertance (L)) that represent the viscous resistance, wall deformability, and blood inertia of the vascular portion, respectively. Governing equations were obtained by imposing mass and momentum conservation along the flow pathway. Taking blood flows in the vicinity of the lower-body capillary bed as an example, the mass conservation equation reads

$$\frac{dP_{\text{cap},l}}{dt} = \frac{Q_{\text{art},l} - Q_{\text{cap},l}}{C_{\text{cap},l}}, \quad (1)$$

and the momentum conservation equation is

$$\frac{dQ_{\text{cap},l}}{dt} = \frac{P_{\text{cap},l} - Q_{\text{cap},l}R_{\text{cap},l} - P_{\text{ven},l}}{L_{\text{cap},l}}. \quad (2)$$

Here, $P_{\text{cap},l}$ and $P_{\text{ven},l}$ refer, respectively, to the blood pressure in the lower-body capillary bed and the veins; $C_{\text{cap},l}$, $R_{\text{cap},l}$, and $L_{\text{cap},l}$ represent, respectively, the compliance, viscous resistance, and blood inertance of the lower-body capillary bed; $Q_{\text{cap},l}$ and $Q_{\text{art},l}$ denote the blood flow rates through the lower-body capillary bed and the upstream arteriolar bed, respectively.

According to the typical anatomy of a single-ventricle heart, the heart was herein modeled to include three chambers, namely, the right atrium, the left atrium, and the left ventricle (the left ventricle is herein taken as the functional ventricle). Moreover, there is an atrial septal defect (ASD) located between the right and left atria. The pumping action of each cardiac chamber was described by a time-varying elastance that has been widely used in previous studies [19–22]:

$$E(t) = E_s e(t) + E_d, \quad (3)$$

where E_s is the maximum value of the active elastance; E_d is the baseline stiffness of the cardiac chamber. For the left ventricle, E_s and E_d reflect the systolic and diastolic functions, respectively. $e(t)$ is a normalized time-varying function of the active elastance; for the left ventricle, it is written as [22]

$$e_{lv}(t) = \begin{cases} 0.5 \left[1 - \cos\left(\frac{\pi t}{T_{\text{vcp}}}\right) \right], & 0 \leq t \leq T_{\text{vcp}}, \\ 0.5 \left\{ 1 + \cos\left[\frac{\pi(t - T_{\text{vcp}})}{T_{\text{vrp}}}\right] \right\}, & T_{\text{vcp}} < t \leq T_{\text{vcp}} + T_{\text{vrp}}, \\ 0, & T_{\text{vcp}} + T_{\text{vrp}} < t \leq T_0. \end{cases} \quad (4)$$

Here, T_0 is the duration of a cardiac cycle; T_{vcp} and T_{vrp} refer, respectively, to the durations of ventricular contraction and relaxation. The modeled elastance curve of the left ventricle under resting conditions (heart rate = 75 beats/min) is compared with in vivo data [23] in Figure 2.

With the elastance being defined, blood pressure (P_{cc}) in each cardiac chamber can be related to chamber volume (V_{cc}) by [19–22]

$$P_{\text{cc}}(t) = E(t)(V_{\text{cc}} - V_{\text{cc},0}) + S_{\text{cc}} \frac{dV_{\text{cc}}}{dt}, \quad (5)$$

where $V_{\text{cc},0}$ refers to the unstressed volume, herein taken to be zero, and S_{cc} is the viscoelasticity coefficient of the cardiac wall.

The hemodynamic effects of cardiac valves were modeled by means of relating the pressure gradient across the valves to the transvalve flow rates [19, 22]. Taking the mitral valve as an example,

$$\Delta P_{\text{mv}} = R_{\text{mv}} Q_{\text{mv}} + B_{\text{mv}} Q_{\text{mv}} |Q_{\text{mv}}| + L_{\text{mv}} \frac{dQ_{\text{mv}}}{dt}, \quad (6)$$

where ΔP_{mv} and Q_{mv} represent the transvalve pressure drop and flow rate, respectively. R_{mv} , B_{mv} , and L_{mv} refer,

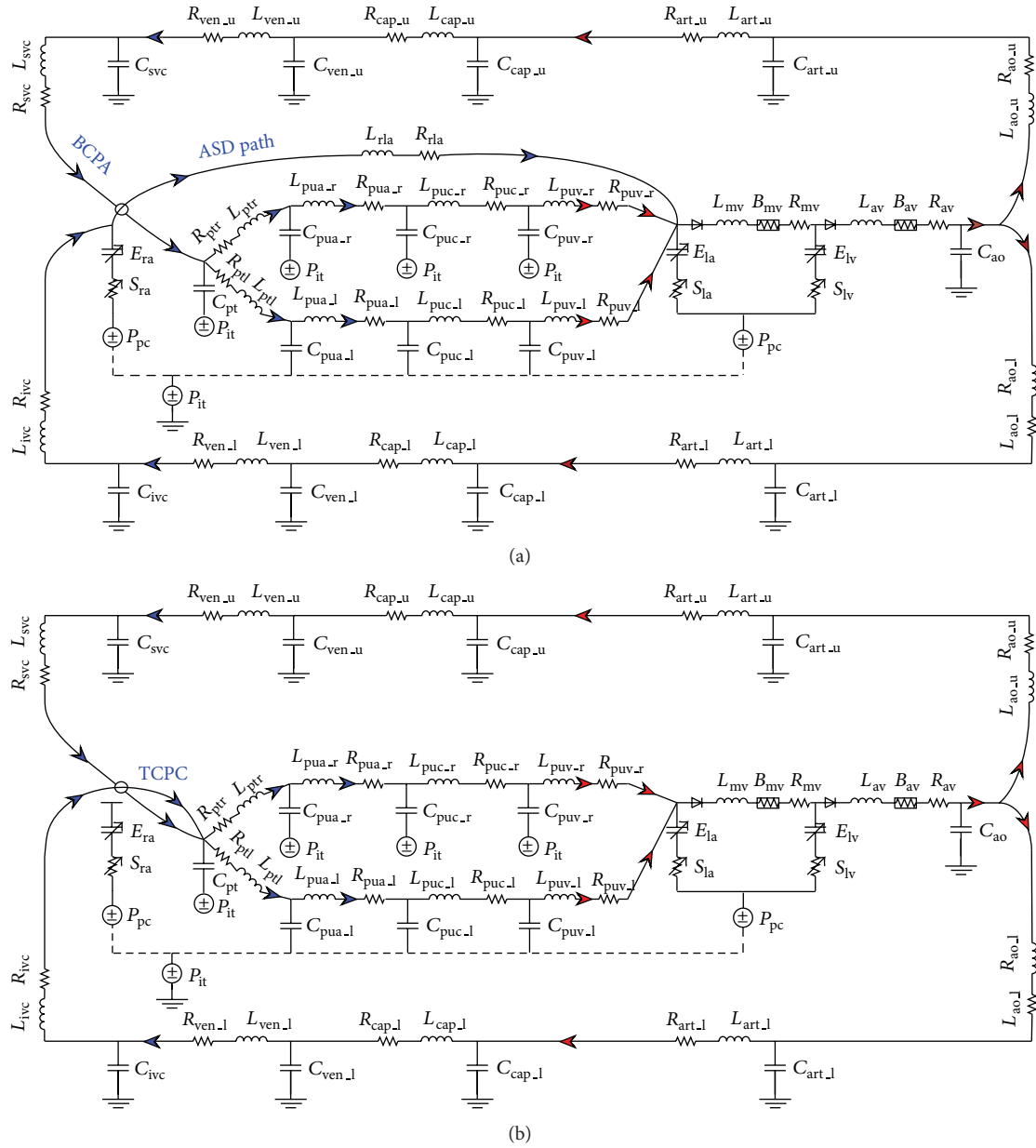


FIGURE 1: Electric analogies of the single-ventricle circulations with a BCPA (a) and a TCPC (b). The arrows indicate the direction of blood flow.

respectively, to the transvalve viscous resistance, Bernoulli's resistance, and blood inductance when the mitral valve is opened.

A normal mitral valve will close when atrial pressure goes below the ventricular pressure and, at the same time, transmitral flow approaches zero, thus effectively preventing the occurrence of reversed flow directed from the left ventricle toward the left atrium. However, such a role may be weakened when pathological changes develop in the leaflets of the mitral valve. A typical phenomenon associated with mitral valve abnormalities is flow regurgitation in systole. To model the phenomenon, we calculated the mitral valve Bernoulli's resistance ($B_{mv,reg}$) and inductance ($L_{mv,reg}$) upon the occurrence of flow regurgitation based on the effective

area of flow regurgitation (A_{reg}) and the dimension of the left atrium:

$$B_{mv,reg} = 0.5\rho\left(\frac{1}{A_{reg}} - \frac{1}{A_{la}}\right)^2, \tag{7}$$

$$L_{mv,reg} = 2\pi\rho\sqrt{\frac{1}{A_{reg}} - \frac{1}{A_{la}}},$$

where ρ is the density of blood; A_{la} is the nominal area of the left atrium calculated from its volume by assuming a spherical shape.

In this way, a mitral valve with regurgitation operates in two modes: (1) the normal mode where the transvalve

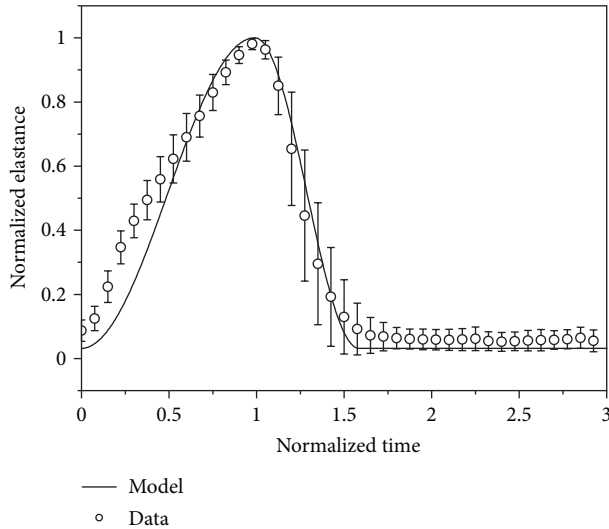


FIGURE 2: Modeled elastance curve ($E(t)$) of the left ventricle compared with in vivo data (mean \pm SD) under resting conditions (heart rate = 75 beats/min). Here, the elastance is normalized by its peak value and time is normalized by the time interval from the beginning of ventricular contraction to the arrival of the peak elastance.

forward flow is computed using the normal valve parameters and (2) the regurgitation mode in which case the atrium to ventricle retrograde flow is computed using the valve parameters derived from (7).

The governing equations consisted mainly of the ordinary differential equations formulated at the R , L , and C components and nonlinear equations that describe cardiac chamber dynamics and cardiac valve function. The equation system was solved using a fourth-order Runge-Kutta method. For more details, the reader is invited to refer to our previous studies [20, 21].

2.2. Parameter Assignment. The parameters used in the models were assigned to reproduce the typical hemodynamic characteristics of a child aged 3-4 years with the weight and height being 17 Kg and 105 cm, respectively. The total vascular compliance (C_{sys}) and pulmonary vascular compliance (C_{pul}) were set as a function of body weight by $C_{sys} = 2.1 * \text{weight}$ [24] and $C_{pul} = 0.408 * \text{weight}$, respectively [25]. For other model parameters, such as systemic/pulmonary vascular resistances and cardiac elastances, although most of them are derivable from previous studies [26–28], there are significant discrepancies among the values used in different studies. Therefore, the model parameters were reassessed in the present study. To this aim, preliminary parameter estimation from a validated adult model [20, 21] was firstly performed based on the weight and body surface area according to the general scaling laws [29]. Subsequently, the parameter values were refined via a parameter optimization procedure [30] aimed to match model-simulated hemodynamic variables with the available in vivo data [18, 31–33]. The assigned parameter values are summarized in Table 1, which were used both in the BCPA circulation model and in the TCPC circulation model. The simulated results for the BCPA

circulation under resting conditions (cardiac duration = 0.67 s) are compared with clinical data in Table 2. It is observed that all the model-simulated hemodynamic values fall within the ranges of the measured data.

2.3. Simulation Conditions. Model parameters corresponding to the major risk factors identified in clinical studies were studied regarding their effects on the hemodynamic consequence of changing a BCPA into a TCPC. The parameters studied include the pulmonary vascular resistance (R_{pul}), the arteriolar resistance of the lower body ($R_{art,1}$), and the ventricular maximum active elastance (E_{slv}) in systole and baseline passive elastance (E_{div}) in diastole. In each set of simulation, a parameter varied from 50% to 250% of its default value in an interval of 10%. It is noted that, when a parameter varied, the other three parameters were held at their default values (as given in Table 1). Moreover, the effects of mitral valve regurgitation were investigated as well by varying the effective area of flow regurgitation from 0.01 to 0.21 cm^2 . In all the simulations, the cardiac duration (T_0), intrathoracic pressure (P_{it}), and pericardial pressure (P_{pc}) were fixed at 0.67 s, -3.5 mmHg, and 3 mmHg, respectively.

3. Results

3.1. Hemodynamic Changes Associated with the Change of a BCPA to a TCPC. Simulations were firstly performed for the BCPA circulation and the TCPC circulation under the control conditions to investigate the basic hemodynamic phenomena associated with the BCPA to TCPC change. The simulated results for the main hemodynamic variables are reported in Table 2, with the corresponding pressure and flow waveforms being illustrated in Figures 3 and 4, respectively. From the results, the BCPA to TCPC change leads to significant hemodynamic changes over the system, such as a marked increase in inferior vena cava (IVC) pressure and a significant decrease in cardiac output and arterial pressure. In addition, there is a slight increase in transpulmonary flow rate upon the BCPA to TCPC change.

The most pronounced changes in flow/pressure waveforms induced by the BCPA to TCPC change were predicted in the IVC. In the BCPA circulation, the IVC blood flow waveform exhibits a typical biphasic shape featured by the presence of two peaks and considerable retrograde flow as has been observed in in vivo studies [34]. After the TCPC operation, only one peak remains and the retrograde flow disappears. At the same time, the pulsatility of the IVC pressure is significantly reduced.

It should be noted that post-TCPC cardiovascular regulation or adaptation has not been considered in the present study. As a consequence, the computed post-TCPC cardiac output and arterial pressure are obviously lower than those reported in previous studies [32].

3.2. The Effects of Cardiovascular Properties on the Changes in Pulmonary Flow Rate and Venous Pressure upon the BCPA to TCPC Change. Figure 5 shows the simulated changes in pulmonary flow rate (a) and IVC pressure (b) when the BCPA

TABLE 1: Default parameter values used in the BCPA circulation model under resting conditions.

Heart	$E_{ras} = 0.26$ $T_0 = 0.67$	$E_{rad} = 0.36$ $T_{vcp} = 0.246$	$E_{las} = 0.5$ $T_{vrp} = 0.147$	$E_{lad} = 0.7$ $S_{ra} = P_{ra} * 0.0005$	$E_{lvs} = 6.64$ $S_{la} = P_{la} * 5E - 4$	$E_{lvd} = 0.18$ $S_{lv} = P_{lv} * 5E - 4$
Cardiac valves	$L_{mv} = 1.4E - 3$	$B_{mv} = 8E - 5$	$R_{mv} = 8E - 3$	$L_{av} = 1.4E - 3$	$B_{av} = 1.2E - 4$	$R_{av} = 1.2E - 2$
Pulmonary circulation	$C_{pt} = 0.144$	$L_{pt,l} = 4E - 3$	$R_{pt,l} = 1E - 3$	$L_{pt,r} = 4E - 3$	$R_{pt,r} = 1E - 3$	
	$L_{pua,l} = 6.7E - 3$	$R_{pua,l} = 0.235$	$C_{pua,l} = 0.217$	$L_{puc,l} = 4E - 3$	$R_{puc,l} = 0.173$	$C_{puc,l} = 2.35$
	$L_{puv,l} = 6.7E - 3$	$R_{puv,l} = 0.103$	$C_{puv,l} = 0.97$	$L_{pua,r} = 6.7E - 3$	$R_{pua,r} = 0.235$	$C_{pua,r} = 0.217$
	$L_{puc,r} = 4E - 3$	$R_{puc,r} = 0.173$	$C_{puc,r} = 2.35$	$L_{puv,r} = 6.7E - 3$	$R_{puv,r} = 0.103$	$C_{puv,r} = 0.97$
ASD	$L_{ASD} = 5E - 4$	$R_{ASD} = 1E - 3$				
Aorta	$L_{ao,l} = 3E - 2$	$R_{ao,l} = 6.5E - 2$	$L_{ao,u} = 1.5E - 2$	$R_{ao,u} = 0.15$	$C_{ao} = 0.267$	
Vena cava	$L_{ivc} = 7.5E - 3$	$R_{ivc} = 2E - 2$	$C_{ivc} = 3.95$	$L_{svc} = 3.8E - 3$	$R_{svc} = 6.4E - 2$	$C_{svc} = 0.54$
Systemic circulation	$L_{art,l} = 1.5E - 2$	$R_{art,l} = 4.22$	$C_{art,l} = 0.13$	$L_{cap,l} = 4.5E - 3$	$R_{cap,l} = 0.32$	$C_{cap,l} = 6E - 2$
	$L_{ven,l} = 9E - 3$	$R_{ven,l} = 6.5E - 2$	$C_{ven,l} = 22.0$	$L_{art,u} = 7.5E - 3$	$R_{art,u} = 2.91$	$C_{art,u} = 1.8E - 2$
	$L_{cap,u} = 2.3E - 3$	$R_{cap,u} = 0.75$	$C_{cap,u} = 8.5E - 3$	$L_{ven,u} = 4.5E - 3$	$R_{ven,u} = 0.15$	$C_{ven,u} = 3.0$

Notation of parameters: E : elastance; S : viscoelastic coefficient; T : time; R : resistance; L : inertance; C : compliance; B : Bernoulli's resistance. Please refer to Figure 1 for the locations of the parameters in the model. Units of parameters: E : mmHg·mL⁻¹; S : mmHg·s·mL⁻¹; T : s; R : mmHg·s·mL⁻¹; L : mmHg·s²·mL⁻¹; C : mL·mmHg⁻¹; B : mmHg·s²·mL⁻².

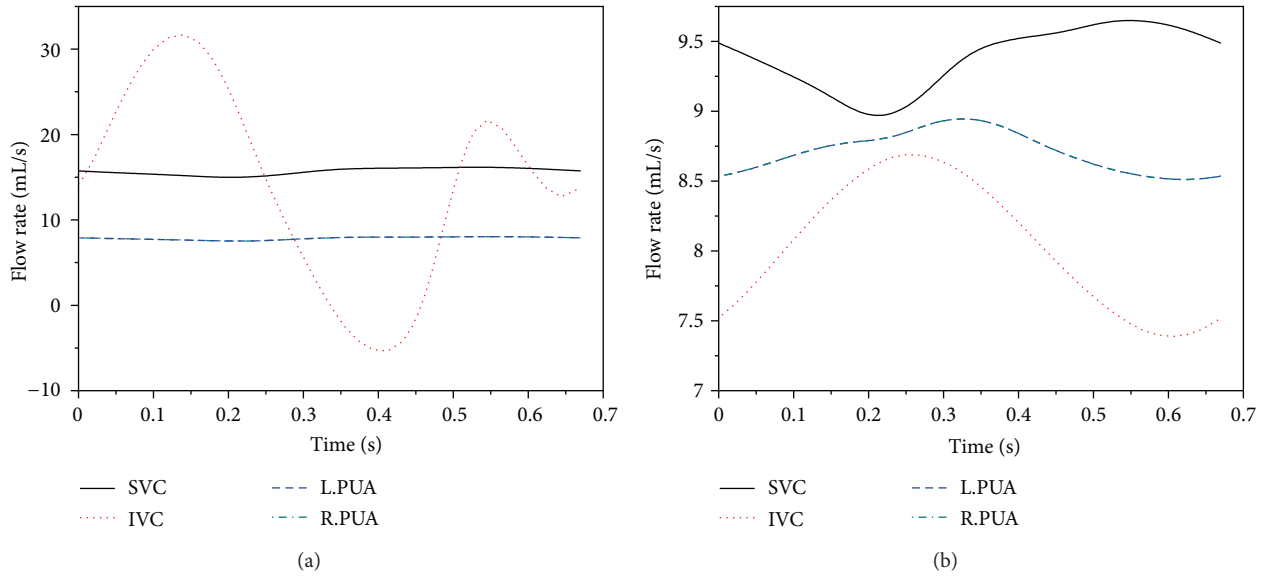


FIGURE 3: Simulated flow waveforms in the vena cava and pulmonary arteries for the BCPA circulation (a) and TCPC circulation (b). SVC: superior vena cava; IVC: inferior vena cava; L.PUA: left pulmonary artery; R.PUA: right pulmonary artery.

is changed into a TCPC under various cardiovascular conditions as described in Section 2.3. Herein, the results are presented in the form of a percentage change in pulmonary flow rate or venous pressure relative to the pre-TCPC value to favor a quantitative comparison among the effects of different parameters. Pulmonary vascular resistance (R_{pul}) and lower-body arteriolar resistance ($R_{art,l}$) are observed to have the most significant influence on the change in transpulmonary flow associated with the TCPC operation. With an extremely high R_{pul} or $R_{art,l}$, pulmonary flow may even decrease after the TCPC operation. Interestingly, with ventricular diastolic dysfunction (herein characterized by increased ventricular chamber stiffness in diastole), the BCPA to TCPC change is accompanied by a larger increase in pulmonary flow.

Relatively, ventricular systolic function only has a mild effect. The change in central venous pressure (herein referring to pressure in the IVC) is determined primarily by pulmonary vascular resistance and ventricular diastolic function, while it is less affected by lower-body arteriolar resistance and ventricular systolic function.

3.3. The Effects of Mitral Valve Regurgitation on the Changes in Pulmonary Flow Rate and Venous Pressure upon the BCPA to TCPC Change. Figure 6 shows the changes in pulmonary flow rate (a) and venous pressure (b) plotted as a function of the severity of mitral valve regurgitation (expressed as the ratio of the retrograde to forward transmitral flow rate over a cardiac cycle). From the results, the presence of mitral valve

TABLE 2: Simulated hemodynamic variables for the BCPA circulation and the TCPC circulation under resting conditions compared with the measured data.

	Glenn (mea.)	Glenn (sim.)	TCPC (sim.)
mP_{svc} (mmHg)	14.0 ± 2.0 [31]; 10.0 [18]	10.0	8.5
mP_{ivc} (mmHg)	5.4 ± 3.2 [32]	5.3	8.0
mP_{pa} (mmHg)	12.3 ± 3.1 [33]; 9.0 [18]	9.0	7.8
mP_{la} (mmHg)	5.0 [18]	5.0	3.4
mP_{art} (mmHg)	72.0 [18]; 73 ± 10 [32]	72.1	45.6
SV (mL)	20.1*	20.1	11.7
EDV (mL)	32.4*	32.5	19.4
EF (%)	62 ± 7 [31]	61.9	60.2
mQ_{pul} (mL/s)	15.6 [18]	15.7	17.4
CO (mL/s)	31.2 ± 7.2 [31]; 28.9 [18]	30.0	17.4

Notation of hemodynamic variables: mP_{svc} , mP_{ivc} , mP_{pa} , mP_{la} , and mP_{art} represent the mean pressure in the superior vena cava, the inferior vena cava, the pulmonary artery, the left atrium, and the systemic arteries, respectively; SV, EDV, and EF refer, respectively, to the stroke volume, the end-diastolic volume, and ejection fraction of the left ventricle; mQ_{pul} denotes the mean blood flow rate through the pulmonary circulation; and CO is cardiac output. The data marked with "*" were derived from CO and EF by assuming a cardiac duration of 0.67 s.

regurgitation tends to improve pulmonary flow, although the degree of improvement is fairly limited (within 3%). Moreover, mitral valve regurgitation attenuates the increase in venous pressure following the BCPA to TCPC change.

4. Discussion

Many risk factors associated with poor clinical outcomes in Fontan operation have been identified in clinical studies [6–11], which typically include high pulmonary vascular resistance, low ventricular ejection fraction, increased ventricular diastolic stiffness, and atrioventricular valve regurgitation. These findings have provided valuable information for refining the management of patients in both the preoperative and postoperative stages. However, it remains unclear how these risk factors influence the transient hemodynamic changes upon the change of a BCPA to a TCPC. The issue has been addressed in the present study using a computational method. The major findings of the study include the following: (1) the change in transpulmonary flow upon the BCPA to TCPC change is determined primarily by the pulmonary vascular resistance, the lower-body arteriolar resistance, and the diastolic function of the left ventricle, while it is less affected by the systolic function of the left ventricle and mitral valve regurgitation and (2) the change in venous pressure is dependent strongly on the pulmonary vascular resistance and the diastolic function of the left ventricle.

The importance of a low pulmonary vascular resistance in improving clinical outcomes in post-TCPC patients has been well documented [8, 9]. The present study provides additional evidence to support the fact that the beneficial role of a low pulmonary vascular resistance is also justifiable at the moment of BCPA to TCPC change in terms of improving the transpulmonary flow and restricting an excessive increase

in central venous pressure. Compared to pulmonary vascular resistance, systemic vascular resistance has been considered as less important for the regulation of cardiac output in post-TCPC patients [35, 36]. Our study, however, demonstrates that the status of the systemic vascular resistance in a BCPA circulation has a considerable influence on perioperative hemodynamic changes upon the BCPA to TCPC change. For example, in the presence of a low lower-body vascular resistance, a larger perioperative increase in transpulmonary flow can be expected, which partly justifies the use of vasodilator drugs in the treatment of single-ventricle patients.

It is interesting to find that diastolic dysfunction of the left ventricle (herein characterized by increased chamber stiffness in diastole) and mitral valve regurgitation enhance the increase in pulmonary flow upon the BCPA to TCPC change. This finding implies that the BCPA to TCPC change may not induce a significant reduction in transpulmonary flow in patients with diastolic dysfunction or mitral valve regurgitation. On the other hand, when the regulation of pulmonary flow after the TCPC operation is concerned, both diastolic dysfunction and mitral valve regurgitation are found to have a significantly adverse effect (see Figure 7). These abnormalities hamper a further increase in pulmonary flow via postoperative compensatory adaptations (e.g., reduction in venous compliance or increase in blood volume), thereby leading to poor long-term clinical outcomes as those which have been confirmed in post-TCPC patients [6–11]. As for ventricular systolic function, although it has little effect on perioperative hemodynamic changes in comparison with diastolic function, it plays a considerable role in regulating transpulmonary flow after the TCPC operation, especially under pathological conditions (see Figure 7(a)).

Although the study has provided some new findings to enrich the current clinical understanding, there are limitations that may influence the clinical application of the findings. A significant limitation may stem from building the models based on *in vivo* data collected from a limited number of patients. Incorporating *in vivo* data obtained from a larger patient group would allow the models to better capture the typical hemodynamic characteristics in the patient cohort. On the other hand, the cardiovascular properties of any single patient may deviate considerably from the population-averaged trends, implying that a comprehensive consideration of the patient-specific cardiovascular conditions is mandatory for a reasonable patient-specific prediction of the hemodynamic changes associated with a surgery. Moreover, under *in vivo* conditions, both short-term compensatory regulation and chronic adaptation are likely to occur after the TCPC operation to maintain arterial pressure and restore cardiac output [37], which would further complicate the roles played by different cardiovascular properties in hemodynamic regulation. These mechanisms, however, have not been incorporated in the present study where the BCPA circulation is converted to a TCPC circulation simply by altering the configuration of the vena cava to pulmonary artery connection without changing the values of other model parameters. As we have mentioned previously, the present study focuses on investigating the transient hemodynamic changes upon the BCPA to TCPC change when the effects

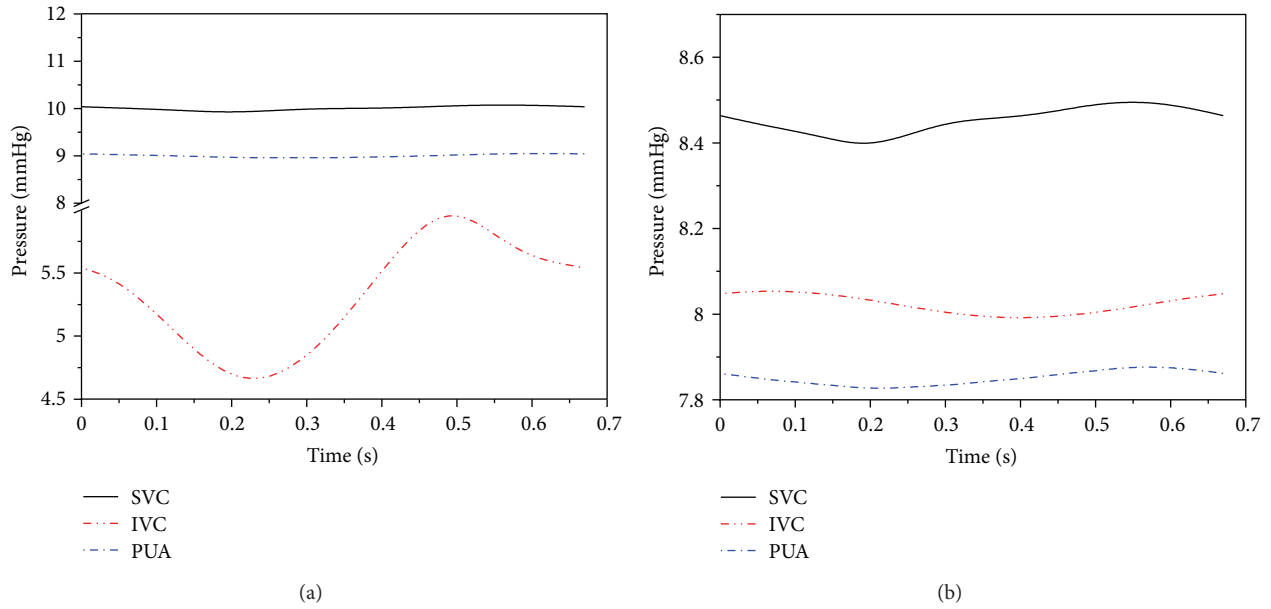


FIGURE 4: Simulated pressure waveforms in the vena cava and pulmonary arteries for the BCPA circulation (a) and TCPC circulation (b).

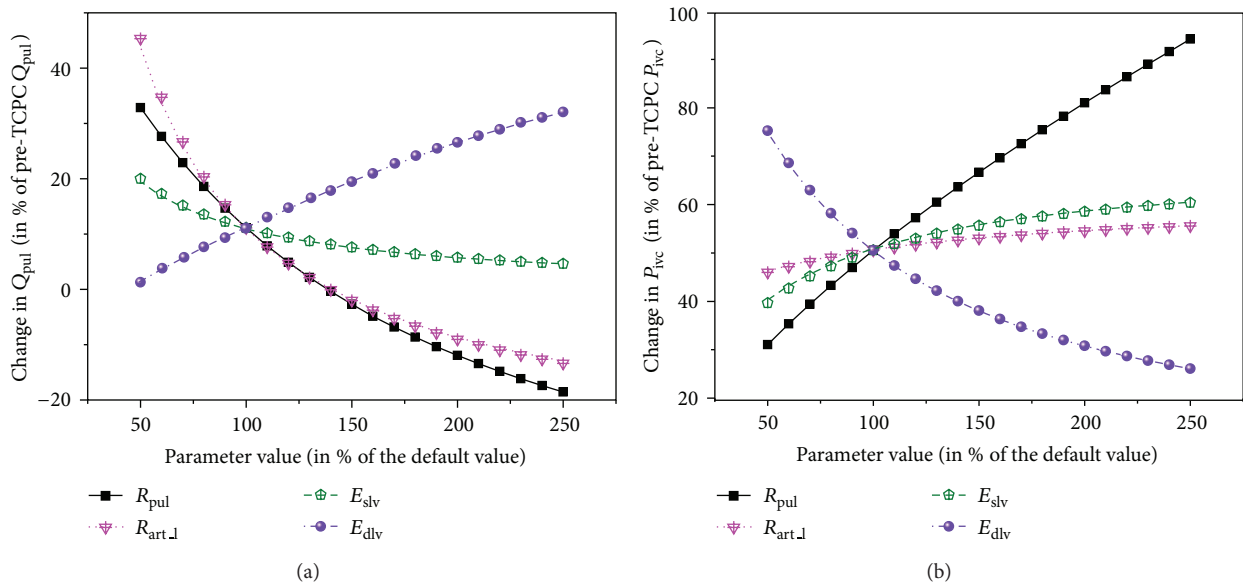


FIGURE 5: Simulated changes in transpulmonary flow rate (Q_{pul} (a)) and venous pressure (P_{ivc} (b)) under various cardiovascular conditions upon the change of a BCPA into a TCPC. The results are expressed as percentage changes relative to the pre-TCPC values. R_{pul} : pulmonary vascular resistance; $R_{art,l}$: lower-body arteriolar resistance; E_{slv} : maximum active elastance of the left ventricle in systole; E_{dlv} : baseline passive elastance of the left ventricle in diastole.

of cardiovascular regulation or adaptation have not appeared. Therefore, the findings of the present study should not be used to interpret the long-term hemodynamic consequence of the TCPC operation.

5. Conclusions

In the present study, computational models were used to quantify the effects of various cardiovascular properties on hemodynamic changes associated with the change of a

BCPA into a TCPC in the Fontan operation. Some new insights have been obtained, which include the following: (1) pulmonary vascular resistance and lower-body vascular resistance are the main determinants of perioperative hemodynamic changes; (2) ventricular diastolic dysfunction and mitral valve regurgitation do not deteriorate perioperative hemodynamic changes, although they significantly impair the capability of the cardiovascular system to further improve pulmonary flow after the operation; and (3) ventricular systolic function has little effect on perioperative hemodynamic changes. These findings may serve as a useful

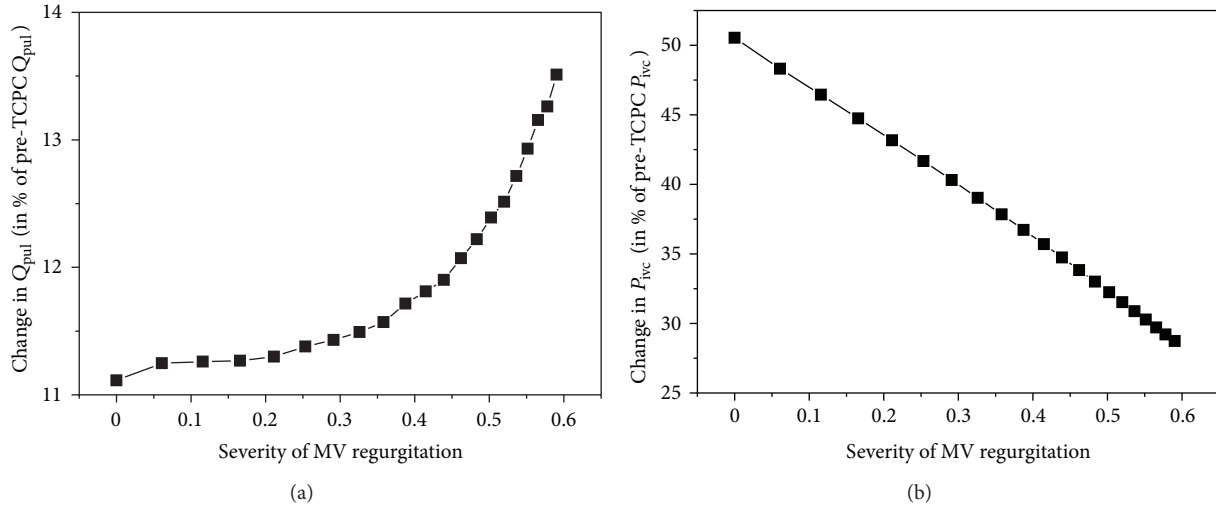


FIGURE 6: Simulated changes in transpulmonary flow rate (Q_{pul}) (a) and venous pressure (P_{ivc}) (b) under various mitral valve (MV) regurgitation conditions upon the change of a BCPA into a TCPC. The results are expressed as percentage changes relative to the pre-TCPC values.

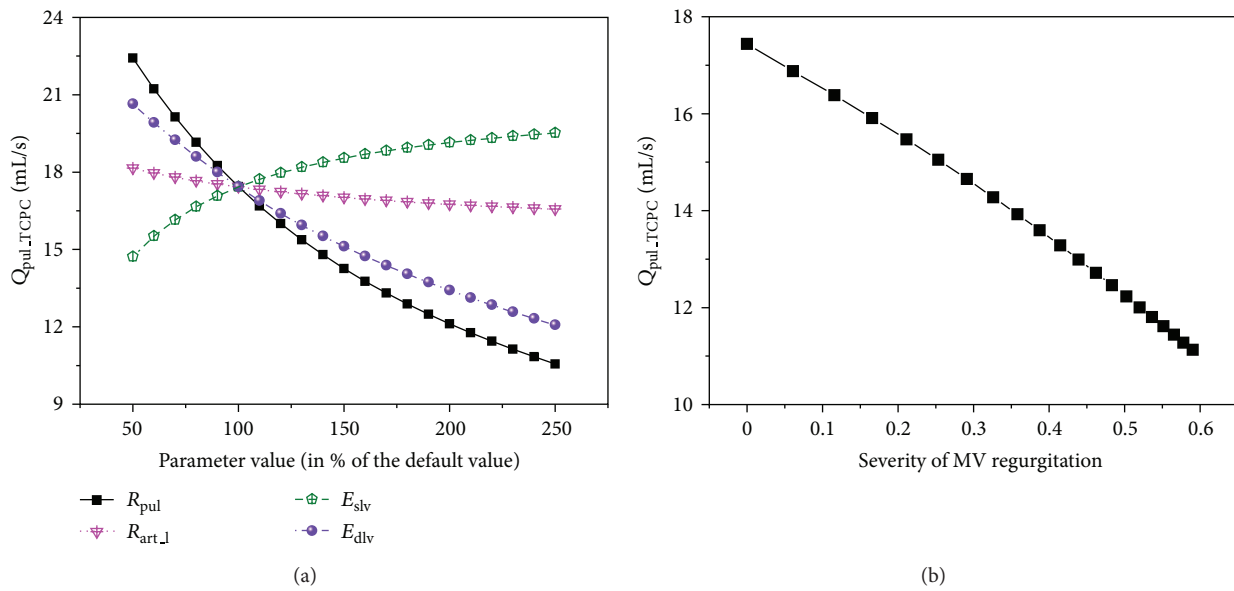


FIGURE 7: Simulated variations in pulmonary flow rate ($Q_{pul.TCPC}$) with cardiovascular properties (a) and the severity of mitral valve regurgitation (b) after the TCPC operation.

theoretical reference for physicians to assess the perioperative risk of the TCPC operation based on preoperative measurement of cardiovascular function.

Conflict of Interests

There is no conflict of interests in this study from any of the authors.

Acknowledgment

This work was supported in part by the SJTU Medical Engineering Cross-Cutting Research Project (YG2012MS24).

References

- [1] W. M. Gersony, "Fontan operation after 3 decades: what we have learned," *Circulation*, vol. 117, no. 1, pp. 13–15, 2008.
- [2] F. Fontan and E. Baudet, "Surgical repair of tricuspid atresia," *Thorax*, vol. 26, no. 3, pp. 240–248, 1971.
- [3] S. Giannico, F. Hammad, A. Amodeo et al., "Clinical outcome of 193 extracardiac Fontan patients: the first 15 years," *Journal of the American College of Cardiology*, vol. 47, no. 10, pp. 2065–2073, 2006.
- [4] H. Ohuchi, K. Kagisaki, A. Miyazaki et al., "Impact of the evolution of the fontan operation on early and late mortality: a single-center experience of 405 patients over 3 decades," *Annals of Thoracic Surgery*, vol. 92, no. 4, pp. 1457–1466, 2011.

- [5] P. Khairy, S. M. Fernandes, J. E. Mayer Jr. et al., "Long-term survival, modes of death, and predictors of mortality in patients with Fontan surgery," *Circulation*, vol. 117, no. 1, pp. 85–92, 2008.
- [6] N. Yoshimura, M. Yamaguchi, Y. Oshima et al., "Risk factors influencing early and late mortality after total cavopulmonary connection," *European Journal of Cardio-Thoracic Surgery*, vol. 20, no. 3, pp. 598–602, 2001.
- [7] Y. Fujii, S. Sano, Y. Kotani et al., "Midterm to long-term outcome of total cavopulmonary connection in high-risk adult candidates," *Annals of Thoracic Surgery*, vol. 87, no. 2, pp. 562–570, 2009.
- [8] H. Uemura, T. Yagihara, Y. Kawashima et al., "What factors affect ventricular performance after a Fontan-type operation?" *The Journal of Thoracic and Cardiovascular Surgery*, vol. 110, no. 2, pp. 405–415, 1995.
- [9] B. Alsoufi, C. Manlihot, A. Awan et al., "Current outcomes of the Glenn bidirectional cavopulmonary connection for single ventricle palliation," *European Journal Cardio-Thoracic Surgery*, vol. 42, no. 1, pp. 42–48, 2012.
- [10] W. L. Border, A. U. Syed, E. C. Michelfelder et al., "Impaired systemic ventricular relaxation affects postoperative short-term outcome in Fontan patients," *The Journal of Thoracic and Cardiovascular Surgery*, vol. 126, no. 6, pp. 1760–1764, 2003.
- [11] C. A. Garofalo, S. E. Cabreriza, T. A. Quinn et al., "Ventricular diastolic stiffness predicts perioperative morbidity and duration of pleural effusions after the fontan operation," *Circulation*, vol. 114, supplement 1, pp. I56–I61, 2006.
- [12] W. Fu, Z. Gu, X. Meng, B. Chu, and A. Qiao, "Numerical simulation of hemodynamics in stented internal carotid aneurysm based on patient-specific model," *Journal of Biomechanics*, vol. 43, no. 7, pp. 1337–1342, 2010.
- [13] J. R. Cebal, M. A. Castro, J. E. Burgess, R. S. Pergolizzi, M. J. Sheridan, and C. M. Putman, "Characterization of cerebral aneurysms for assessing risk of rupture by using patient-specific computational hemodynamics models," *American Journal of Neuroradiology*, vol. 26, no. 10, pp. 2550–2559, 2005.
- [14] Y. Qian, H. Takao, M. Umezu, and Y. Murayama, "Risk analysis of unruptured aneurysms using computational fluid dynamics technology: preliminary results," *American Journal of Neuroradiology*, vol. 32, no. 10, pp. 1948–1955, 2011.
- [15] C. M. Haggerty, D. A. de Zélicourt, M. Restrepo et al., "Comparing pre- and post-operative Fontan hemodynamic simulations: implications for the reliability of surgical planning," *Annals of Biomedical Engineering*, vol. 40, no. 12, pp. 2639–2651, 2012.
- [16] J. Ding, Y. Liu, and F. Wang, "Influence of bypass angles on extracardiac Fontan connections: a numerical study," *International Journal for Numerical Methods in Engineering*, vol. 29, no. 3, pp. 351–362, 2013.
- [17] Y. Qian, J. L. Liu, K. Itatani, K. Miyaji, and M. Umezu, "Computational hemodynamic analysis in congenital heart disease: simulation of the Norwood procedure," *Annals of Biomedical Engineering*, vol. 38, no. 7, pp. 2302–2313, 2010.
- [18] A. Baretta, C. Corsini, W. Yang et al., "Virtual surgeries in patients with congenital heart disease: a multi-scale modelling test case," *Philosophical Transactions of the Royal Society A*, vol. 369, no. 1954, pp. 4316–4330, 2011.
- [19] Y. Sun, M. Beshara, R. J. Lucariello, and S. A. Chiaramida, "A comprehensive model for right-left heart interaction under the influence of pericardium and baroreflex," *American Journal of Physiology—Heart and Circulatory Physiology*, vol. 272, part 2, no. 3, pp. H1499–H1515, 1997.
- [20] F. Liang and H. Liu, "A closed-loop lumped parameter computational model for human cardiovascular system," *JSME International Journal C*, vol. 48, no. 4, pp. 484–493, 2005.
- [21] F. Liang and H. Liu, "Simulation of hemodynamic responses to the Valsalva maneuver: an integrative computational model of the cardiovascular system and the autonomic nervous system," *Journal of Physiological Sciences*, vol. 56, no. 1, pp. 45–65, 2006.
- [22] F. Liang, S. Takagi, R. Himeno, and H. Liu, "Multi-scale modeling of the human cardiovascular system with applications to aortic valvular and arterial stenoses," *Medical and Biological Engineering and Computing*, vol. 47, no. 7, pp. 743–755, 2009.
- [23] H. Senzaki, C. Chen, and D. A. Kass, "Single-beat estimation of end-systolic pressure-volume relation in humans: a new method with the potential for noninvasive application," *Circulation*, vol. 94, no. 10, pp. 2497–2506, 1996.
- [24] K. Van Heusden, J. Gisolf, W. J. Stok, S. Dijkstra, and J. M. Karemaker, "Mathematical modeling of gravitational effects on the circulation: importance of the time course of venous pooling and blood volume changes in the lungs," *American Journal of Physiology—Heart and Circulatory Physiology*, vol. 291, no. 5, pp. H2152–H2165, 2006.
- [25] W. R. Milnor, A. D. Jose, and C. J. McGaff, "Pulmonary vascular volume, resistance, and compliance in man," *Circulation*, vol. 22, pp. 130–137, 1960.
- [26] G. Pennati, F. Migliavacca, G. Dubini, R. Pietrabissa, and M. R. De Leval, "A mathematical model of circulation in the presence of the bidirectional cavopulmonary anastomosis in children with a univentricular heart," *Medical Engineering and Physics*, vol. 19, no. 3, pp. 223–234, 1997.
- [27] K. Laganà, R. Balossino, F. Migliavacca et al., "Multiscale modeling of the cardiovascular system: application to the study of pulmonary and coronary perfusions in the univentricular circulation," *Journal of Biomechanics*, vol. 38, no. 5, pp. 1129–1141, 2005.
- [28] E. Magosso, S. Cavalcanti, and M. Ursino, "Theoretical analysis of rest and exercise hemodynamics in patients with total cavopulmonary connection," *American Journal of Physiology—Heart and Circulatory Physiology*, vol. 282, no. 3, pp. H1018–H1034, 2002.
- [29] J. A. Goodwin, W. L. van Meurs, C. D. S. Sá Couto, J. E. W. Beneken, and S. A. Graves, "A model for educational simulation of infant cardiovascular physiology," *Anesthesia and Analgesia*, vol. 99, no. 6, pp. 1655–1664, 2004.
- [30] K. Sugimoto, F. Liang, Y. Takahara et al., "Assessment of cardiovascular function by combining clinical data with a computational model of the cardiovascular system," *The Journal of Thoracic and Cardiovascular Surgery*, vol. 145, no. 5, pp. 1367–1372, 2013.
- [31] M. Yoshida, M. Yamaguchi, N. Yoshimura, H. Murakami, H. Matsuhisa, and Y. Okita, "Appropriate additional pulmonary blood flow at the bidirectional Glenn procedure is useful for completion of total cavopulmonary connection," *Annals of Thoracic Surgery*, vol. 80, no. 3, pp. 976–981, 2005.
- [32] H. Ohuchi, K. Yasuda, A. Miyazaki et al., "Haemodynamic characteristics before and after the onset of protein losing enteropathy in patients after the Fontan operation," *European Journal Cardio-Thoracic Surgery*, vol. 43, no. 3, pp. e49–e57, 2013.
- [33] Y. Tanoue, A. Sese, Y. Ueno, K. Joh, and T. Hijii, "Bidirectional Glenn procedure improves the mechanical efficiency of a total cavopulmonary connection in high-risk fontan candidates," *Circulation*, vol. 103, no. 17, pp. 2176–2180, 2001.

- [34] T. Hsia, S. Khambadkone, A. N. Redington, F. Migliavacca, J. E. Deanfield, and M. R. De Leval, "Effects of respiration and gravity on infradiaphragmatic venous flow in normal and fontan patients," *Circulation*, vol. 102, supplement 3, no. 19, pp. III148–III153, 2000.
- [35] M. Gewillig, S. C. Brown, B. Eyskens et al., "The Fontan circulation: who controls cardiac output?" *Interactive Cardiovascular and Thoracic Surgery*, vol. 10, no. 3, pp. 428–433, 2010.
- [36] A. A. Kouatli, J. A. Garcia, T. M. Zellers, E. M. Weinstein, and L. Mahony, "Enalapril does not enhance exercise capacity in patients after fontan procedure," *Circulation*, vol. 96, no. 5, pp. 1507–1512, 1997.
- [37] U. S. Krishnan, I. Taneja, M. Gewitz, R. Young, and J. Stewart, "Peripheral vascular adaptation and orthostatic tolerance in fontan physiology," *Circulation*, vol. 120, no. 18, pp. 1775–1783, 2009.

Research Article

Design Optimization of Coronary Stent Based on Finite Element Models

Hongxia Li,¹ Tianshuang Qiu,² Bao Zhu,³ Jinying Wu,¹ and Xicheng Wang¹

¹ State Key Laboratory of Structural Analysis for Industrial Equipment, Department of Engineering Mechanics, Dalian University of Technology, Dalian 116024, China

² Department of Electronic Engineering, Dalian University of Technology, Dalian 116024, China

³ Surface Engineering Laboratory, School of Materials Science and Engineering, Dalian University of Technology, Dalian 116024, China

Correspondence should be addressed to Xicheng Wang; guixum@dlut.edu.cn

Received 24 July 2013; Accepted 2 September 2013

Academic Editors: H.-C. Han, M. Ohta, and A. Qiao

Copyright © 2013 Hongxia Li et al. This is an open access article distributed under the Creative Commons Attribution License, which permits unrestricted use, distribution, and reproduction in any medium, provided the original work is properly cited.

This paper presents an effective optimization method using the Kriging surrogate model combining with modified rectangular grid sampling to reduce the stent dogboning effect in the expansion process. An infilling sampling criterion named expected improvement (EI) is used to balance local and global searches in the optimization iteration. Four commonly used finite element models of stent dilation were used to investigate stent dogboning rate. Thrombosis models of three typical shapes are built to test the effectiveness of optimization results. Numerical results show that two finite element models dilated by pressure applied inside the balloon are available, one of which with the artery and plaque can give an optimal stent with better expansion behavior, while the artery and plaque unincluded model is more efficient and takes a smaller amount of computation.

1. Introduction

Atherosclerosis is one of the most serious forms of cardiovascular disease which is one of the principal causes of mortality. Currently, three of the most common treatments for a narrowed or weakened coronary artery disease are coronary artery bypass grafting, percutaneous transluminal coronary balloon angioplasty, and percutaneous transluminal coronary stenting with the aid of coronary balloon angioplasty. Of these, the coronary stent market increased rapidly because of their high initial success rate, minimal invasive nature, and improved long-term effectiveness compared to coronary artery bypass grafting or coronary balloon angioplasty. When a stent is used, it is collapsed to a small diameter and put over a balloon-tipped tube called a catheter. With the balloon inflating the stent expands, locks in place, and forms a scaffold to hold the artery open and improve blood flow. Although stent technology has been greatly improved since its inception, many problems remain in which related to restenosis (i.e., the artery that was opened begins to become narrowed again within months of the procedure). This phenomenon

is related to both arterial injury and inflammatory response of the wall against the stent struts. Therefore, efforts aiming at reducing the injury caused by stent implantations remain very meaningful.

Previous studies indicated that the dogboning phenomenon (i.e., the ends of a stent opening first during expansion), which is due to nonuniform balloon-stent expansion, has a significant impact on thrombosis and hyperplasia development [1, 2]. This mechanical injury, that is, caused by the warped struts in the stent is often thought to induce an inflammatory response, which results in thrombosis and affects artery restenosis [3–6]. The effects of balloon length and compliance on vascular stent expansion were investigated by Cui et al. [7]. It is also believed that the stent design may affect stent expansion performance, including the dogboning phenomenon. Thus, it is important in stenting to predict and optimize the dogboning effect before manufacturing the stent.

There are many published studies that investigated the mechanical properties of stent expansion. The mechanical properties of balloon-stent system expansion were simulated

by the loading of radial displacement applied on inner surface of balloon [3, 8]. It is a simplified loading which can reduce the amount of computation but not close to the real. In addition, a time-related pressure was applied on the balloon surface to analyze the characteristics of balloon-stent system dilation [4, 5]. This loading is much close to the real situation but the interaction between the stent and the vessel wall was not considered. Moreover, multicontact including plaque/stent, balloon/stent, and plaque/balloon was considered and the radial displacement on balloon was used to dilate the balloon-stent system [6]. Clearly, this FEA model is more complete, but the loading is still simplified. Subsequently, the balloon-stent system dilation in narrowed artery was modeled with the loading mode of a time-related pressure applied on inner surface of balloon [9]. This FEA model with the internal pressure loading is much closer to the real situation, but it takes a lot of computing because of nonlinearities, such as elastoplasticity, large deformation, and multicontact. In the present paper, the four common finite element models of stent expansion mentioned above are used to design optimization for reducing dogboning effect, respectively.

The dogboning rate is an important index for assessing the quality of stent expansion [10]. It is a nonlinear, implicit function of the geometrical parameters and internal pressure loads for the stent, these are typically evaluated by the solution of the finite element method (FEM). Depending on the fidelity of simulation for stent dilation, it can become computationally expensive, limiting structural optimization of the stent. Therefore, it is challenging to reduce the computational cost of predicting the dogboning rate during the optimization process. Consequently, some approximation models are widely used during engineering to construct simplified approximations for the analysis codes, providing a surrogate model of the original code. In the present paper, we use Kriging models as alternatives to traditional second-order polynomial response surfaces for constructing global approximations for stent optimization. The Kriging model [11, 12], a semiparametric approach that does not rely on any specific model structure, is much more flexible than approaches based on parametric behavioral models [13].

In terms of stent optimization, the expansion behaviors of several stents with different given geometries were compared in terms of dogboning, foreshortening, elastic recoil, and so forth. [5]. It is easy to perform and analyze the effective factors, but the obtained “optimal stents” are only better combinations of geometry parameter levels, not the optimal solution in the design space. An adaptive optimization method based on Kriging surrogate model with a “space-filling” sampling strategy named rectangular grid is here proposed to minimize the absolute value of dogboning rate of the stent in expanding process. Kriging surrogate model can build an approximate function relationship between the stent dogboning rate and design variables (the geometrical parameters of the stent), replacing the expensive FEM reanalysis of dogboning rate in the optimization. The adaptive process is implemented by EI function. It can balance local and global search and tend to find the global optimal design.

The optimization iterations are based on the surrogate model for reducing the high computational cost.

2. Materials and Methods

2.1. Finite Element Models. ANSYS finite element package was used to perform the numerical simulations. A typical diamond-shaped coronary stent (shown in Figure 1) was investigated in this study. A balloon with an 11.4 mm length and a 0.12 mm thickness was placed inside the stent. Its outside diameter was equal to the inside diameter of the stent. The stent was not in contact with the plaque at the beginning of the dilatation process. The outside surface of the plaque was adhered to the inner surface of the artery.

Bilinear elastic-plastic, hyperelastic (Mooney-Rivlin) and linear isotropic (nearly incompressible) materials are here assumed for the slotted tube stents, balloon, and tissue (plaque and artery), respectively. All the material properties inputted are based on the data available from previous studies [2, 9].

The four FEA models are here constructed. LRD model (shown in Figure 2(a)) is loaded by a radial displacement applied on the inner surface of balloon to expand the diameters of stent from 2.54 mm to 4.54 mm. This is to allow the stenotic segment to be opened corresponding to the health artery (diameter 4.54 mm in this study). It is discretized by 11815 elements and 10180 nodes, in which the plaque, artery, stent, and balloon consist of 500 solid elements, 330 solid elements, 5103 solid elements, and 600 shell elements, respectively. The contact pairs of balloon/stent, plaque/stent, and balloon/plaque consist of 5282 contact elements. LPV model (shown in Figure 2(b)) is the same as LRD model except the loading method. This model is loaded by a time-related pressure (shown in Figure 3). It should be noted that the pressures are varied with different stent geometries. The binary-search method was used to find the pressures used to dilate the proximal region of the stents (see Figure 1) to the nominal diameter (4.54 mm in this study) after unloading. This was done to allow the stenotic segment to be opened in agreement with a health artery (diameter 4.54 mm in this study) after stent dilation. LPC model (shown in Figure 2(c)) is similar to LPV model except the constant pressure. The last one is SMPV model which has the same loading method as LPV model, but artery and plaque were not considered (shown in Figure 2(d)). It is discretized by 8004 elements and 8444 nodes, in which the stent and balloon consist of 5103 solid elements and 600 shell elements, respectively. Only one contact pair of balloon/stent consists of 2301 contact elements.

The pattern of the transient nonuniform stent expansion based on the four FEA models is shown in Figure 4. Based on LPV, LPC, and SMPV model, the radial displacement in the distal region of the stent is larger than the proximal displacement at the second instant shown in Figures 4(a) and 4(c). However, the radial displacement in the distal region of the stent is closed to the proximal displacement since the third instant is shown in Figures 4(a) and 4(c), corresponding to the final phase of the expansion and unloading. These

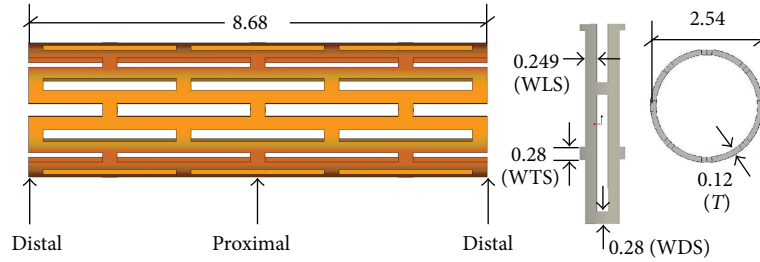


FIGURE 1: Stent model and geometric variables (mm). WLS, WTS and WDS are the width of the struts.

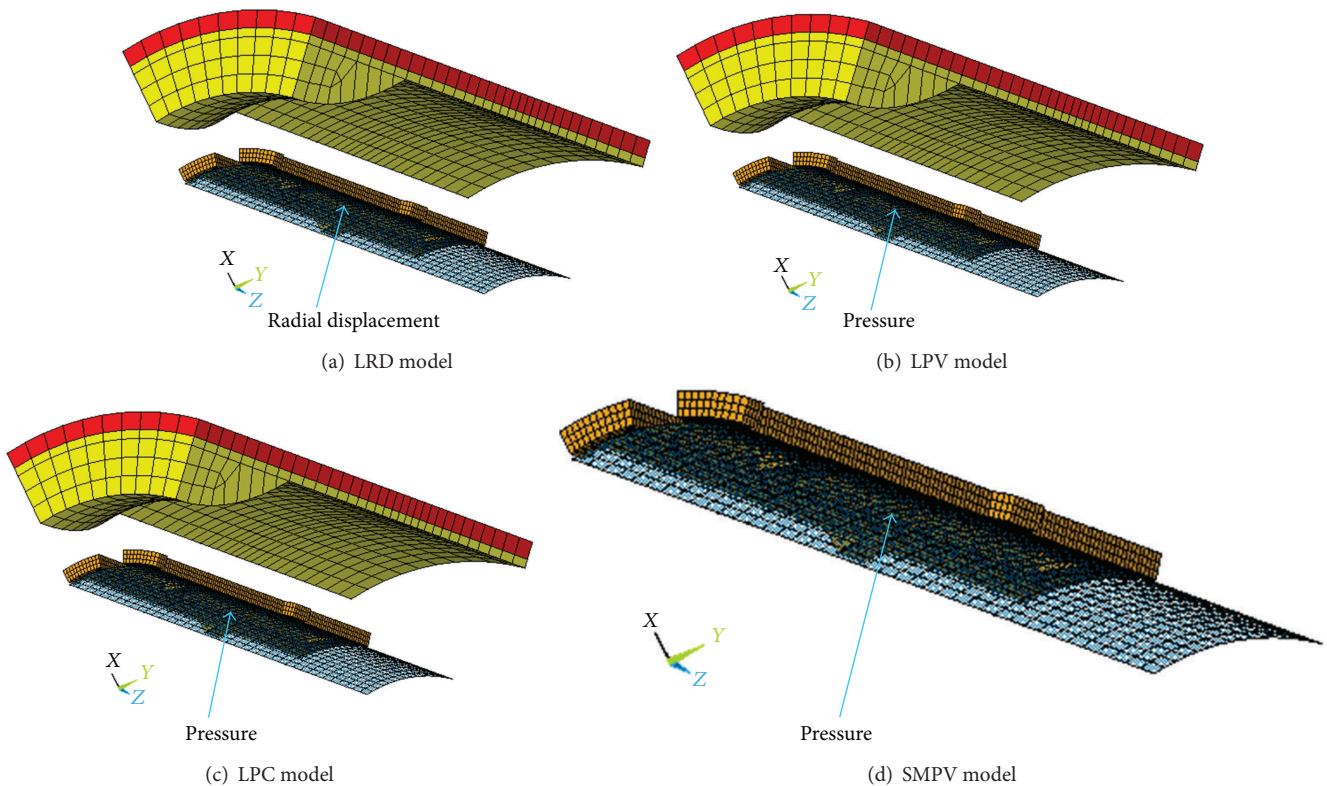


FIGURE 2: FEM models. (a) LRD model: loaded by a radial displacement to expand the diameters of stent from 2.54 mm to 4.54 mm. (b) LPV model: loaded by a pressure to expand the diameters of stent from 2.54 mm to 4.54 mm. (c) LPC model: loaded by a constant pressure. (d) SMPV model: without artery and plaque, loaded by a pressure to expand the diameters of stent from 2.54 mm to 4.54 mm.

results are compared favorably with those reported in the literature [10, 14, 15] while based on LRD model; the radial displacement in the distal region of the stent is almost equal to the radial displacement in the proximal region of the stent because of the constant displacement loaded on the inner surface of balloon (shown in Figure 4(b)).

2.2. Optimization Problem. Generally, the dogboning effect exists throughout the expanding process. It usually reaches its maximum in the beginning of loading [16, 17], but the struts are not in contact with the vessel wall. From 25 ms to 32 ms, the stent approaches an approximately cylindrical

shape (corresponded to regime of the third and fourth instant appeared during the expansion of stent shown in Figures 4(a) and 4(c)), and the dogboning effect is relatively small, but stent radial displacement reaches the maximum, pushing against the artery. The dogboning observed during this period can cause serious transient mechanical injury to vessel wall. The dogboning rate of stent is here defined as

$$\text{Dogboning Rate} = \frac{d_{\text{radial}}^{\text{distal}} - d_{\text{radial}}^{\text{proximal}}}{d_{\text{radial}}^{\text{proximal}}}, \quad (1)$$

where $d_{\text{radial}}^{\text{distal}}$ and $d_{\text{radial}}^{\text{proximal}}$ are the distal and proximal radial displacements of stent, respectively. Because the radial of

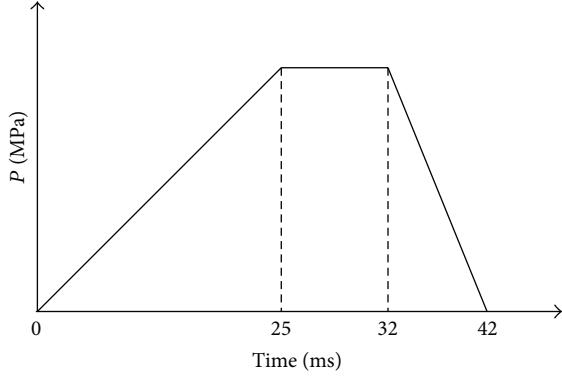


FIGURE 3: Time-related pressure.

stent reaches its maximum at the ending time of loading process (i.e., 32 ms), moreover, the $d_{\text{radial}}^{\text{distal}}$ is very large, which will induce transient mechanical damage to vessel wall, the optimization problem of the coronary stent for expanding process can be defined as follows:

$$\begin{aligned} \text{Min} \quad & f(\mathbf{x}) = \left| \frac{d_{\text{radial}}^{\text{distal}}(\mathbf{x}) - d_{\text{radial}}^{\text{proximal}}(\mathbf{x})}{d_{\text{radial}}^{\text{proximal}}(\mathbf{x})} \right| \\ \text{S.t} \quad & \underline{\mathbf{x}} \leq \mathbf{x} \leq \bar{\mathbf{x}}, \end{aligned} \quad (2)$$

where \mathbf{x} is a vector of design variables, which consists of the geometrical parameters such as WDS, WTS, WLS, and T in Figure 1, $f(\mathbf{x})$ is an objective function, and $d_{\text{radial}}^{\text{distal}}(\mathbf{x})$ and $d_{\text{radial}}^{\text{proximal}}(\mathbf{x})$ are the distal radial displacement and proximal radial displacement of stent at the 32 ms for LPV, LPC, and SMPV models, while for LPD model, they are the distal radial displacement and proximal radial displacement of stent after unloading. $\underline{\mathbf{x}}$ and $\bar{\mathbf{x}}$ are lower and upper limits of the design variables (here $0.22 \leq \text{WDS} \leq 0.34$, $0.22 \leq \text{WTS} \leq 0.34$, $0.2 \leq \text{WLS} \leq 0.3$, $0.1 \leq T \leq 0.14$).

2.3. Kriging Model

2.3.1. Approximation Method. The Kriging model is described as a way of modeling a function as a realization of a stochastic process, so it is named the ‘‘stochastic process model’’, which can be written as

$$\hat{y}(\mathbf{x}^i) = F(\boldsymbol{\beta}, \mathbf{x}^i) + z(\mathbf{x}^i) = \mathbf{f}^T(\mathbf{x}^i) \boldsymbol{\beta} + z(\mathbf{x}^i) \quad (3)$$

in which $\mathbf{x}^i = \{x_1^i, x_2^i, \dots, x_m^i\}$ is the i th sample point with m variables; $\hat{y}(\mathbf{x}^i)$ is an approximate function fitted to n sample points; $\mathbf{f}(\mathbf{x}^i)$ is a linear or nonlinear function of \mathbf{x}^i ; $\boldsymbol{\beta}$ is the regression coefficient vector to be estimated; and $z(\mathbf{x}^i)$ is the stochastic function, with a mean of zero and a variance σ^2 .

The spatial correlation function between stochastic functions is given by

$$\begin{aligned} \text{corr}[z(\mathbf{x}^i), z(\mathbf{x}^j)] &= R(\theta, \mathbf{x}^i, \mathbf{x}^j) \\ &= \prod_{l=1}^m \exp[-\theta(x_l^i - x_l^j)^2], \end{aligned} \quad (4)$$

where $R(\theta, \mathbf{x}^i, \mathbf{x}^j)$ is the Gaussian correlation function with θ , which characterizes the spatial correlation between two samples. Parameters can be estimated by maximizing the likelihood of samples

$$\begin{aligned} \hat{\boldsymbol{\beta}} &= \frac{\mathbf{f}^T R^{-1} \mathbf{y}}{\mathbf{f}^T R^{-1} \mathbf{f}} \\ \hat{\sigma}^2 &= \frac{(\mathbf{y} - \mathbf{f}^T \hat{\boldsymbol{\beta}})^T R^{-1} (\mathbf{y} - \mathbf{f}^T \hat{\boldsymbol{\beta}})}{n} \\ \hat{\theta} &= \min \{ \psi(\theta) \equiv |R|^{1/n_s} \sigma^2 \}, \end{aligned} \quad (5)$$

where $\mathbf{f} = [f_1, f_2, \dots, f_n]$. The estimates $\hat{\boldsymbol{\beta}}$ and $\hat{\sigma}^2$ can then be obtained from (5).

2.3.2. Predictor. The function value $\hat{y}(\mathbf{x}^*)$ at a new point \mathbf{x}^* can be approximately estimated as a linear combination of the response values of sample \mathbf{Y} :

$$\hat{y}(\mathbf{x}^*) = \mathbf{c}^T \mathbf{Y}. \quad (6)$$

The mean squared error (MSE) of this predictor is minimized with unbiased estimation, which gives

$$\hat{y}(\mathbf{x}^*) = \mathbf{f}(\mathbf{x}^*) \hat{\boldsymbol{\beta}} + \mathbf{r}(\mathbf{x}^*)^T \boldsymbol{\gamma}, \quad (7)$$

where

$$\begin{aligned} \boldsymbol{\gamma} &= R^{-1} (\mathbf{Y} - \mathbf{F} \hat{\boldsymbol{\beta}}) \\ \mathbf{r}(\mathbf{x}^*) &= [R(\theta, \mathbf{x}_1, \mathbf{x}^*), \dots, R(\theta, \mathbf{x}_n, \mathbf{x}^*)]. \end{aligned} \quad (8)$$

Thus, we can predict the function value $\hat{y}(\mathbf{x}^*)$ at every new point \mathbf{x}^* by using (7).

As mentioned above, the Kriging model is an interpolation model, and the Kriging predictor is a predictor that minimizes the expected squared prediction error subject to (i) being unbiased and (ii) being a linear function of the observed response values.

2.3.3. Sampling Strategy. A modified Rectangular Grid (MRG) approach was used to provide sample points for building the Kriging model. Defining the range of m input variables as $l_j \leq x_j \leq u_j$, $j = 1, \dots, m$, the number of levels in the j th dimension is q_j . Then, the approach is performed as follows:

(1) Contract the ranges of the variables as

$$l_j \leq x_j \leq \hat{u}_j, \quad \hat{u}_j = u_j - \frac{1}{2} \frac{u_j - l_j}{q_j - 1}, \quad j = 1, \dots, m. \quad (9)$$

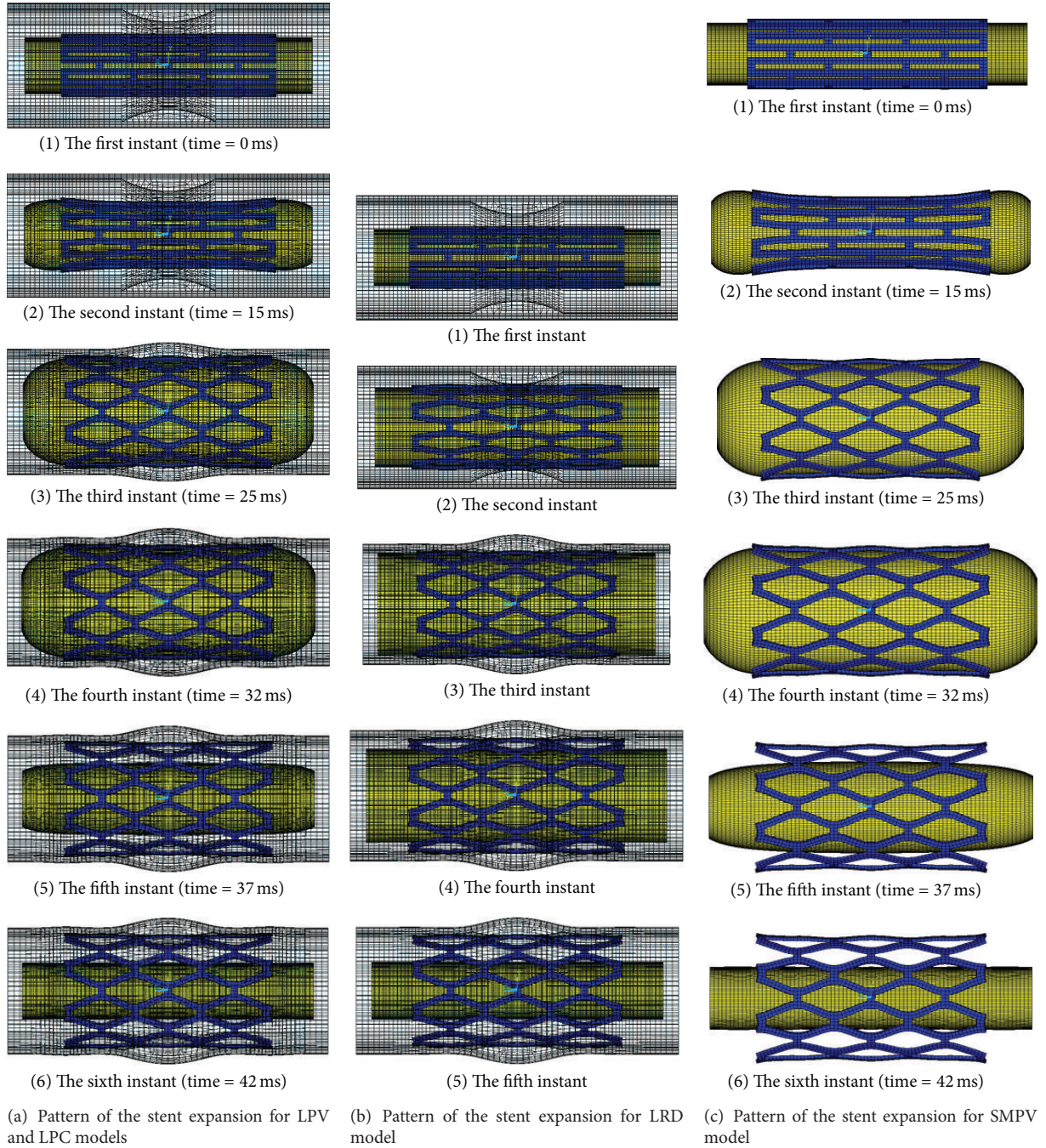


FIGURE 4: Pattern of the stent expansion based on the four FEA models.

(2) Perform RG sampling in the contracted space as

$$x_j^{(i)} = l_j + k_j^{(i)} \frac{\hat{u}_j - l_j}{q_j - 1}, \quad k_j = 0, 1, \dots, q_j - 1, \quad (10)$$

$$i = 1, 2, \dots, \prod_{j=1}^m q_j.$$

(3) Add a stochastic movement to each dimension of each sample point as

$$\frac{\alpha_{ij} u_j - l_j}{2 q_j - 1}, \quad (11)$$

where $\alpha_{ij} \in [0, 1]$ is from a uniform distribution.

2.3.4. *Expected Improvement (EI)*. The simplest way for optimization is to find the minimum of the response surface which is interpolated through the Kriging method. This way can easily lead to a local minimum, even if iterations are performed. Fortunately, an “expected improvement” function can balance local and global search. This method has been viewed as an Effective Global Optimization (EGO) [17]. The “expected improvement (EI)” method computes the extent of improvement expected to achieve if sampling at a given point. Before sampling at some point \mathbf{x} , the value of $Y(\mathbf{x})$ is unknown. Thus, $Y(\mathbf{x})$ can be regarded as a random variable normally distributed with a mean $\hat{y}(\mathbf{x})$ and variance σ^2 and given by the Kriging predictor. If the current best function value is Y_{\min} , then we will achieve an improvement of I if $Y(\mathbf{x}) = Y_{\min} - I$. The likelihood of achieving this improvement is given by the normal density function

$$\frac{1}{\sqrt{2\pi}\sigma(\mathbf{x})} \exp\left[-\frac{(Y_{\min} - I - \hat{y}(\mathbf{x}))^2}{2\sigma^2(\mathbf{x})}\right]. \quad (12)$$

The expected improvement is simply the expected value of the improvement found by integrating over the following density:

$$E[I(\mathbf{x})] = \int_{I=0}^{I=\infty} I \left\{ \frac{1}{\sqrt{2\pi}\sigma(\mathbf{x})} \exp\left[-\frac{(Y_{\min} - I - \hat{y}(\mathbf{x}))^2}{2\sigma^2(\mathbf{x})}\right] \right\} dI. \quad (13)$$

Using integration by parts, one can show that

$$E[I(\mathbf{x})] = \sigma(\mathbf{x}) [u\Phi(u) + \phi(u)], \quad (14)$$

where

$$u = \frac{Y_{\min} - \hat{y}(\mathbf{x})}{\sigma(\mathbf{x})}, \quad (15)$$

and where Φ and ϕ are the normal cumulative distribution and density functions, respectively.

The first term of (14) is the difference between the current minimum response value Y_{\min} and the prediction $\hat{y}(\mathbf{x})$ at \mathbf{x} , penalized by the probability of improvement. Hence, this value is large when $\hat{y}(\mathbf{x})$ is small. The second term is the product of the root mean squared error (RMSE) $\sigma(\mathbf{x})$ and the normal density function $\phi(u)$. The normal density function value is large when $\sigma(\mathbf{x})$ is large and $\hat{y}(\mathbf{x})$ is closed to Y_{\min} . Thus, the expected improvement will tend to be large at a point with a predicted value smaller than Y_{\min} and/or when there is a lot of uncertainty associated with the prediction.

The EI method has the following advantages: it is a balance between seeking promising areas of the design space and the uncertainty in the model and can thus allow a small DOE size; it can avoid searching the areas with large function values and reduce the computational cost; it can avoid the addition of some points close to each other in the design space that may lead to instability of the Kriging model.

2.3.5. *The Convergence Criterion*. The convergence criterion is here to satisfy

$$\frac{EI(\mathbf{x}_k)}{Y_{\max} - Y_{\min}} < \varepsilon_1, \quad (16)$$

$$|\tilde{f}(\mathbf{x}_k) - f(\mathbf{x}_k)| \leq \varepsilon_2,$$

where ε_1 and ε_2 are the convergence tolerances. Y_{\max} and Y_{\min} are the maximal and minimal function values in samples, respectively. The left-hand side of the equation is a ratio between the maximal expected improvement and the “active span” of the responses, which is also referred to as the maximal “relative EI.” $\tilde{f}(\mathbf{x}_k)$ is the approximate value of the objective function obtained by Kriging model in the k th iteration. An advantage of this convergence criterion is that the user can set the “relative” tolerances ε_1 and ε_2 without prior consideration of the magnitudes of the problem response.

2.4. *Optimization Algorithm*. Optimization design algorithm for coronary stent based on Kriging model is described as follows.

Step 1. Get a set of samples with n_s points (each point corresponding to a group of design variables) using MRG approach, and run ANSYS program to obtain the objective function $f(\mathbf{x}_i)$ for the sample point i , $i = 1, \dots, n_s$. Then, select a group of the design variables corresponding with minimum $f(\mathbf{x}_i)$ as the initial design and set $k = 1$. To be noticed is that Binary-search method was used to find the exact pressure to dilate stent at sample point i , $i = 1, \dots, n_s$ to nominal diameter for the optimization based on LPV and SMPV models, respectively.

Step 2. Build an approximate function relationship $\tilde{f}(\mathbf{x})$ between the objective function $f(\mathbf{x})$ and design variables using Kriging model based on the trial samples obtained.

Step 3. Minimize $\tilde{f}(\mathbf{x})$ to get a modified design $\mathbf{x}^{(k)}$ by means of Kriging approximate model, then compute the corresponding $\tilde{f}(\mathbf{x}^{(k)})$ by ANSYS program.

Step 4. Check convergence: if convergence criteria are satisfied, then $\mathbf{x}^* = \mathbf{x}^{(k)}$ and stop; else add the modified design \mathbf{x}^* into the set of samples, and $k = k + 1$ go to Step 2. Note that the initial design will be renewed if the modified design is better than former initial design.

In this optimization problem, MRG method was used to get the sampling points. The FEM simulation can be seen as a black-box, in which a vector \mathbf{x} of design variables (i.e., WTS, WDS, WLS, and T) is input and the corresponding response $\tilde{f}(\mathbf{x})$ (i.e., the absolute value of the dogboning rate) is output. Kriging surrogate model was used as alternative to traditional second-order polynomial response surfaces for constructing a global approximate relationship between the objective function $f(\mathbf{x})$ and design vector \mathbf{x} based on the trial samples. After the approximate relationship between the objective function and design vector was constructed, EI function is

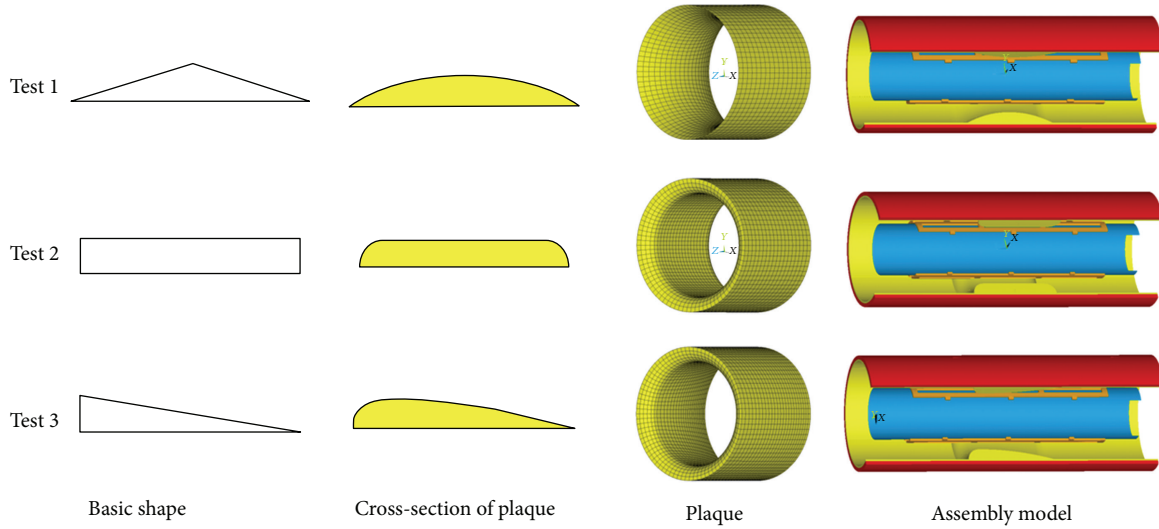


FIGURE 5: Test models with three different typical cross-section shapes of plaque. (1) Test 1: arc-shaped. (2) Test 2: bar-shaped. (3) Test 3: streamline-shaped.

TABLE 1: Optimization results.

	WDS (mm)	WTS (mm)	WLS (mm)	T (mm)	P (MPa)	Dogboning rate	Reduced by
Original stent	0.28	0.28	0.249	0.12	1.948 (LPV/LPC) 1.9114 (SMPV)	0.1452 (LPV/LPC) 0.0908 (SMPV) 0.0582 (LRD)	—
Optimal stent (LRD)	0.22	0.34	0.2568	0.1355	—	0.0061	89.52%
Optimal stent (LPV)	0.2367	0.22	0.2	0.1	1.7602	$9.71e - 5$	99.93%
Optimal stent (LPC)	0.2483	0.2881	0.2	0.1	1.948	0.0027	98.14%
Optimal stent (SMPV)	0.3262	0.2582	0.2056	0.1	1.7491	$9.803e - 5$	99.89%

used to balance local and global search and tends to find the global optimal design. Sequential quadratic programming optimization algorithm was employed to implement the design optimization based on max EI and obtain the modified design vector \mathbf{x}_k . The optimization iteration started from an initial design (here is a sample corresponding with minimum $f(\mathbf{x})$ in the trial samples). The procedure of building and maximizing EI continues until the stopping criterions are reached, such as the criterion described in Section 2.3.5. The optimization process stops when the Euclidean norm between real value $f(\mathbf{x}^{(k)})$ from FEM simulation and predictive value $\tilde{f}(\mathbf{x}^{(k)})$ from Kriging predictor falls below a given tolerance ε_1 , and the Euclidean norm between current and previous iterates falls below a given tolerance ε_2 .

3. Results and Discussion

The optimization converged after 22, 8, 13, and 12 iterations based on LRD, LPV, LPC, and SMPV model, respectively. The optimization results are shown in Table 1.

LRD model is loaded by a radial displacement applied on the inner surface of balloon (shown in Figure 2(a)). This loading mode is a simplified loading which can reduce computation consume, but it does not match the real load,

weakening the impact of stent geometries (WDS, WTS, WLS, and T) on dogboning effect. The optimization process based on LRD model may be more time-consuming. The numerical results show that the optimal WDS is smaller than WTS, which does not meet the manufacturer’s design concept.

LPV model can give the most realistic simulation of stent-balloon system expansion in narrowed artery and the optimal result is reasonable. But this model contains more elements and nodes, which will complex the FEA simulation of stent dilation.

LPC model has a same deployment pressure for all sampling designs of stent in optimization process, resulting in the expansion of stent at different degree. The optimal stent based on this model is expanded to the diameter of 5.8158 mm which is far greater than the nominal diameter of health artery (4.54 mm in this study). Thus, the optimal stent based on this FEM model is not available.

SMPV model has the same loading method as LPV model, but does not contain artery and plaque. The interaction between the vessel wall and the balloon-stent system was not considered. However, SMPV model is a simplified model and the FEM simulation is much simpler.

Three typical plaques (shown in Figure 5) are built for the testing of optimal stents obtained based on SMPV and

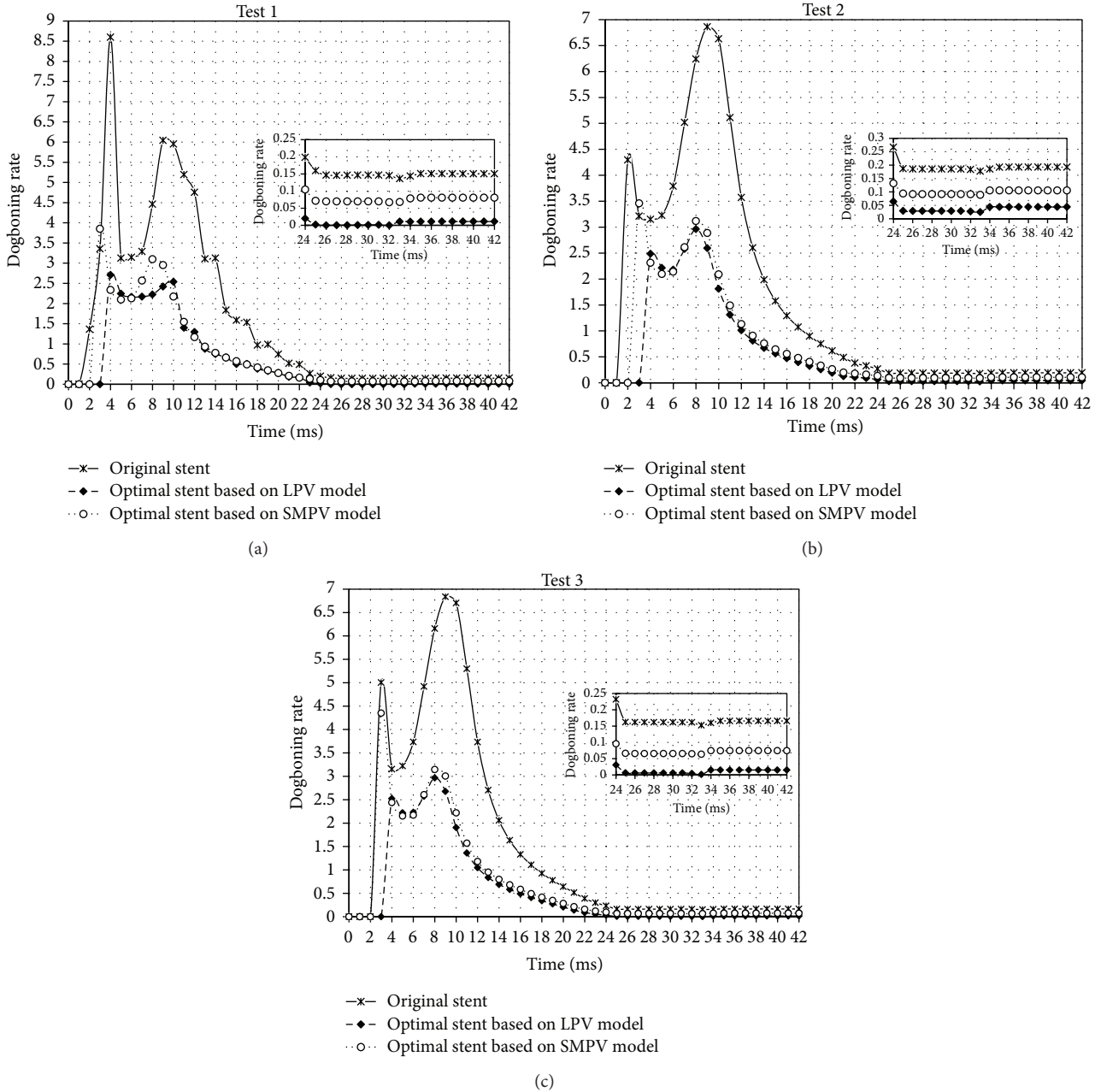


FIGURE 6: Dogboning rate for original and optimal stents along with time (mSec) of stent dilation.

TABLE 2: Test results.

Test model	Stent	WDS (mm)	WTS (mm)	WLS (mm)	T (mm)	P (MPa)	Dogboning rate	Reduced by
Test 1	Original stent	0.28	0.28	0.249	0.12	1.948	0.1452	—
	Optimal stent based on LPV	0.2367	0.22	0.2	0.1	1.7602	$9.71e-5$	99.93%
	Optimal stent based on SMPV	0.3262	0.2582	0.2056	0.1	1.7950	0.0643	55.72%
Test 2	Original stent	0.28	0.28	0.249	0.12	1.9745	0.1856	—
	Optimal stent based on LPV	0.2367	0.22	0.2	0.1	1.7868	0.0270	85.45%
	Optimal stent based on SMPV	0.3262	0.2582	0.2056	0.1	1.8140	0.0914	50.75%
Test 3	Original stent	0.28	0.28	0.249	0.12	1.9555	0.1617	—
	Optimal stent based on LPV	0.2367	0.22	0.2	0.1	1.765	0.0062	96.17%
	Optimal stent based on SMPV	0.3262	0.2582	0.2056	0.1	1.7914	0.0492	69.57%

LPV models. The dilations of original stent and optimal stents based on SMPV and LPV models in three typical stenosed arteries are respectively simulated to get the dogboning rates of them. Table 2 shows the results of the test, in which, the dogboning rates of stent dilation in narrowed arteries of the three typical plaques are significantly reduced, especially for the optimal stent based on LPV model.

Based on LPV model, after optimization the dogboning rates of stent dilation in the three test models are respectively reduced by 99.93%, 85.45% and 96.17%, while based on SMPV model, those are respectively reduced by 55.72%, 50.75%, and 69.57%, as shown in Table 2. It is clearly that LPV model is more suitable for stent optimization based on FEM model. But LPV model contains more elements and nodes, which will complex the FEA simulation of stent dilation. Furthermore, Binary-search method was used to find the exact pressures to dilate the diameters of stent at sample points to nominal diameter and this will take a lot of computation. The optimal stent obtained by using SMPV model can also decrease the dogboning rates of stent dilation in narrowed artery with the three typical plaques. It is not as significantly as that obtained by using LPV model. Because WDS, WTS, and WLS of the optimal stent based on SMPV model are larger than those of the optimal stent based on LPV model, higher deployment pressures are needed to dilate stent diameters to nominal diameter in stenosed artery. When the optimal stent obtained from SMPV model is placed inside stenosed artery, stent dilation will be constrained by the raised plaque at the proximal parts of stent, so that the distal parts of stent will open first, which can cause dogboning effect. This is the reason why the dogboning effect of the optimal stent based on SMPV model dilation in stenosed arteries cannot be dismissed. But SMPV model contains fewer elements and nodes. Therefore, the corresponding FEA simulation is much simpler.

The time-dogboning rate curves for original and optimal stents are shown in Figure 6 for the stent expansion process in three test models. The dogboning effect reaches the maximum at the prophase of loading stage and is reduced and remained in an almost constant value after stent expansion (corresponded to regime of the third and fourth instants, with the loading time from 25 to 32 ms, appeared during the expansion of the stent shown in Figures 4(a) and 4(c)). The radial displacement during this period reaches its maximum, and there is a strong effect of mutual contact between stent and artery wall. The dogboning observed during this period can cause serious transient mechanical injury. From the three test results, it can be seen that both the optimal stents based on LPV and SMPV models observed in the current study can reduce the dogboning significantly, especially for the optimal stent based on LPV model.

4. Conclusions

In this paper, the design optimizations based on four common FEM models of stent expansion are investigated to reduce the dogboning effect by using an adaptive optimization method based on Kriging surrogate model. Plaques of three typical shapes are built for general testing of optimal

stents. The results show that both LPV model and SMPV model can be used for stent optimization based on FEM model. The optimal stents based on both LPV and SMPV models can decrease dogboning effect significantly, especially for the optimal stent based on LPV model.

Acknowledgments

The authors gratefully acknowledge financial support for this work from the National Natural Science Foundation (no. 11072048), the National Basic Research Program (no. 2009CB918501) of China.

References

- [1] D. M. Beule, P. Mortier, S. G. Carlier, B. Verhegghe, R. Van Impe, and P. Verdonck, "Realistic finite element-based stent design: The impact of balloon folding," *Journal of Biomechanics*, vol. 41, no. 2, pp. 383–389, 2008.
- [2] S. N. D. Chua, B. J. Mac Donald, and M. S. J. Hashmi, "Finite-element simulation of stent expansion," *Journal of Materials Processing Technology*, vol. 120, no. 1–3, pp. 335–340, 2002.
- [3] W.-Q. Wang, D.-K. Liang, D.-Z. Yang, and M. Qi, "Analysis of the transient expansion behavior and design optimization of coronary stents by finite element method," *Journal of Biomechanics*, vol. 39, no. 1, pp. 21–32, 2006.
- [4] S. N. D. Chua, B. J. MacDonald, and M. S. J. Hashmi, "Effects of varying slotted tube (stent) geometry on its expansion behaviour using finite element method," *Journal of Materials Processing Technology*, vol. 155–156, no. 1–3, pp. 1764–1771, 2004.
- [5] F. Etave, G. Finet, M. Boivin, J.-C. Boyer, G. Rioufol, and G. Thollet, "Mechanical properties of coronary stents determined by using finite element analysis," *Journal of Biomechanics*, vol. 34, no. 8, pp. 1065–1075, 2001.
- [6] W. Wu, W.-Q. Wang, D.-Z. Yang, and M. Qi, "Stent expansion in curved vessel and their interactions: a finite element analysis," *Journal of Biomechanics*, vol. 40, no. 11, pp. 2580–2585, 2007.
- [7] F. S. Cui, H. P. Lee, C. Lu, and P. Chai, "Effects of balloon length and compliance on vascular stent expansion," *International Journal of Applied Mechanics*, vol. 2, no. 3, pp. 681–697, 2010.
- [8] D.M. Beule, P. Mortier, S. G. Carlier, B. Verhegghe, R. Van Impe, and P. Verdonck, "Realistic finite element-based stent design: the impact of balloon folding," *Journal of Biomechanics*, vol. 41, no. 2, pp. 383–389, 2008.
- [9] S. N. D. Chua, B. J. MacDonald, and M. S. J. Hashmi, "Finite element simulation of slotted tube (stent) with the presence of plaque and artery by balloon expansion," *Journal of Materials Processing Technology*, vol. 155–156, no. 1–3, pp. 1772–1779, 2004.
- [10] W.-Q. Wang, D.-K. Liang, D.-Z. Yang, and M. Qi, "Analysis of the transient expansion behavior and design optimization of coronary stents by finite element method," *Journal of Biomechanics*, vol. 39, no. 1, pp. 21–32, 2006.
- [11] S. N. Lophaven, H. B. Nielsen, and J. Sondergaard, *DACE—A Matlab Kriging Toolbox, Version 2, informatics and mathematical Modelling*, Technical University of Denmark, 2002.
- [12] D. R. Jones, M. Schonlau, and W. J. Welch, "Efficient global optimization of expensive black-box functions," *Journal of Global Optimization*, vol. 13, no. 4, pp. 455–492, 1998.
- [13] J. P. Costa, L. Pronzato, and E. Thierry, "A comparison between kriging and radial basis function networks for nonlinear prediction," in *Proceedings of the IEEE-EURASIP Workshop on*

Nonlinear Signal and Image Processing (NSIP '99), Antalya, Turkey, 1999.

- [14] C. Dumoulin and B. Cochelin, "Mechanical behaviour modelling of balloon-expandable stents," *Journal of Biomechanics*, vol. 33, no. 11, pp. 1461–1470, 2000.
- [15] F. Migliavacca, L. Petrini, V. Montanari, I. Quagliana, F. Auricchio, and G. Dubini, "A predictive study of the mechanical behaviour of coronary stents by computer modelling," *Medical Engineering and Physics*, vol. 27, no. 1, pp. 13–18, 2005.
- [16] D. E. Kioussis, A. R. Wulff, and G. A. Holzapfel, "Experimental studies and numerical analysis of the inflation and interaction of vascular balloon catheter-stent systems," *Annals of Biomedical Engineering*, vol. 37, no. 2, pp. 315–330, 2009.
- [17] H. Zahedmanesh, D. John Kelly, and C. Lally, "Simulation of a balloon expandable stent in a realistic coronary artery-Determination of the optimum modelling strategy," *Journal of Biomechanics*, vol. 43, no. 11, pp. 2126–2132, 2010.

Research Article

Propose a Wall Shear Stress Divergence to Estimate the Risks of Intracranial Aneurysm Rupture

Y. Zhang,¹ H. Takao,² Y. Murayama,² and Y. Qian¹

¹ Australian School of Advanced Medicine, Macquarie University, Sydney, NSW 2109, Australia

² Jikei University School of Medicine, Tokyo 105-8461, Japan

Correspondence should be addressed to Y. Qian; yi.qian@mq.edu.au

Received 30 July 2013; Accepted 29 August 2013

Academic Editors: H.-C. Han, M. Ohta, and A. Qiao

Copyright © 2013 Y. Zhang et al. This is an open access article distributed under the Creative Commons Attribution License, which permits unrestricted use, distribution, and reproduction in any medium, provided the original work is properly cited.

Although wall shear stress (WSS) has long been considered a critical indicator of intracranial aneurysm rupture, there is still no definite conclusion as to whether a high or a low WSS results in aneurysm rupture. The reason may be that the effect of WSS direction has not been fully considered. The objectives of this study are to investigate the magnitude of WSS ($|WSS|$) and its divergence on the aneurysm surface and to test the significance of both in relation to the aneurysm rupture. Patient-specific computational fluid dynamics (CFD) was used to compute WSS and wall shear stress divergence (WSSD) on the aneurysm surface for nineteen patients. Our results revealed that if high $|WSS|$ is stretching aneurysm luminal surface, and the stretching region is concentrated, the aneurysm is under a high risk of rupture. It seems that, by considering both direction and magnitude of WSS, WSSD may be a better indicator for the risk estimation of aneurysm rupture (154).

1. Introduction

Rupture of intracranial aneurysm (IA) is a widely studied topic. It is reported that about 5% of adults have unruptured IAs [1–3]. Though the rupture rate of IAs is not high [4], it causes serious consequences including disability and mortality [5]. On the other hand, current treatments of IAs also carry a risk. Thus, accurate assessment of IA rupture is essential for clinicians to balance the risk of surgery against the risk of natural IAs rupture [6, 7].

Research into risk factor for IAs rupture has been reported for many years, including the effect of aneurysm size, geometry, location, and others [8, 9]. Large-sized aneurysms were considered to be under high risk of rupture. However, recent studies have shown that many ruptured aneurysms were small in size [9, 10]. In order to improve estimations of risk based on medical images, multiple geometric factors were proposed, such as aspect ratio (AR), size ratio (SR), and other factors. The statistic significance of these geometric factors to aneurysm rupture has been discussed in previous publications [11–13]. In addition to performing

image diagnosis, computational fluids dynamics (CFD) technology is available to analyse hemodynamic characteristics inside the artery and aneurysm [14]. The magnitude of wall shear stress ($|WSS|$) has been proposed as a quantitative indicator for the flow characterization of ruptured cerebral aneurysms. Cebal et al. [15] performed CFD for a total of 62 cerebral aneurysms at various locations. They found that high-speed narrow jet flows were commonly observed in ruptured cases, which caused high $|WSS|$ at the inlet area of the aneurysm [15]. Shojima et al. studied twenty middle carotid artery (MCA) aneurysms. Usually, spatial averaged $|WSS|$ was higher within ruptured aneurysms than that in the parent artery. However, they also indicated that $|WSS|$ was markedly reduced at the top of or within a bleb area of the ruptured aneurysm [13, 16]. Thus, it is not clear whether high or low $|WSS|$ induces aneurysm rupture; some argue that high $|WSS|$ induces aneurysm rupture [17], while others claim that low $|WSS|$ at aneurysm dome is dangerous [18].

It may be important to note that wall shear stress (WSS) is a vector. Therefore, WSS must not be considered in terms of not only magnitude but directionality as well. In this paper,

authors propose a new concept of wall shear stress divergence (WSSD), which takes into account both the gradient and direction of WSS and can be used to identify “tensile” and “compressive” regions on the aneurysm surface. Two risk factors based on WSSD distribution are also derived in order to analyse the characteristics of ruptured aneurysms.

2. Materials and Method

2.1. Patients. Nineteen patients with middle sized ICA aneurysms were observed continuously by a three-dimensional computer tomograph angiograph (3D-CTA). For ruptured-IAs, the images were obtained during the observation of 5 months on average before the occurrence of rupture, generally at the time of the patient’s last clinical visit. The three patients who had subsequent aneurysm rupture (age range, 62–71 years; aneurysm size range, 5.3–7.7 mm) are cases 1–3 in this study. The other 16 patients were stable at followup. Their age range was between 40 and 78 years, with aneurysm being between 3.0 and 9.0 mm in size.

2.2. Wall Shear Stress Divergence. Wall shear stress divergence is expressed as following equation

$$\text{WSSD} = \text{div}(\vec{\text{WSS}}) = \frac{\partial \text{WSS}_i}{\partial x_i}, \quad i = 1, 2, 3, \quad (1)$$

where WSS_i are wall shear stress components in i directions. If WSSD has a positive value, the net effect of WSS is to stretch the aneurysm surface; otherwise, WSS is compressing the aneurysm surface. The magnitude of WSSD represents the intensity of stretching or compressing.

2.3. WSSD Based Risk Factors

2.3.1. Wave Centre of Positive WSSD (WSSD^+), Negative WSSD (WSSD^-), and $|\text{WSS}|$. As the blood flow slows down after entering the aneurysm (shown in Figure 1(a)), all stresses decay to the surroundings in the form of a wave attenuation. Figure 1(b) shows the wave centre of WSSD^+ (red ball), WSSD^- (green ball), and $|\text{WSS}|$ (yellow ball), respectively. WSSD^+ and WSSD^- can be treated as two waves propagating in different directions. The former is stretching the aneurysm surface; the latter is compressing the aneurysm surface. In one cardiac cycle, the net effects of WSSD on aneurysm volume are counteracting (Figure 1(c)).

If the wave centers of $|\text{WSS}|$ and WSSD^+ are at close locations, which is dangerous, because the combination of WSS and its gradient will result in a potentially dangerous remodelling of the aneurysm [19]. On the other hand, if the wave center for both WSSD^- and WSSD^+ are close to one another, the two components will compete at their boundaries (C region in Figure 1(c)), resulting in a constant shift in character for the WSS at the boundary, from “stretching” to “compressive”. This may cause a shift in flow reversal which may be adverse to the survival of endothelial cells [20]. Thus, DA and DB and the centre distance of WSSD^+ to $|\text{WSS}|$ and WSSD^- are introduced to estimate the risk of aneurysm rupture (Figure 1(c)).

2.3.2. Risk Factor A. Risk factor A (RFA) is given by the following equation:

$$\text{RFA} = \frac{r_{\text{effect}}}{\text{DA}} \frac{r_{\text{effect}}}{\sqrt{(x_{|\text{WSS}|,i} - x_{\text{WSSD}^+,i})^2}}, \quad i = 1, 2, 3, \quad (2)$$

where r_{effect} is the effective radius of the aneurysm (Figure 1(b)), which is given by the following equation:

$$r_{\text{effect}} = \sqrt[3]{\frac{3V}{4\pi}}. \quad (3)$$

V is the volume of aneurysm. $x_{|\text{WSS}|,i}$ and $x_{\text{WSSD}^+,i}$ are the centre of $|\text{WSS}|$ and WSSD^+ , respectively, given by the following equations:

$$x_{|\text{WSS}|,i} = \frac{1}{T} \int_0^T \frac{\sum_{j=1}^N x_i \times |\text{WSS}|_j}{\sum_{j=1}^N |\text{WSS}|_j} dt, \quad i = 1, 2, 3, \quad (4)$$

$$x_{\text{WSSD}^+,i} = \frac{1}{T} \int_0^T \frac{\sum_{j=1}^N x_i \times \text{WSSD}^+_{,j}}{\sum_{j=1}^N \text{WSSD}^+_{,j}} dt, \quad i = 1, 2, 3, \quad (5)$$

where T is the time period of cardiac cyclic, j is the indicator of mesh point, and N is the total mesh number.

2.3.3. Risk Factor B. Risk factor B (RFB) is given by the following equation:

$$\text{RFB} = \frac{r_{\text{effect}}}{\text{DB}} \frac{r_{\text{effect}}}{\sqrt{(x_{\text{WSSD}^+,i} - x_{\text{WSSD}^-,i})^2}}, \quad i = 1, 2, 3, \quad (6)$$

where $x_{\text{WSSD}^-,i}$ is the wave center of WSSD^- . Similar to (5), $x_{\text{WSSD}^-,i}$ is given by the following equation:

$$x_{\text{WSSD}^-,i} = \frac{1}{T} \int_0^T \frac{\sum_{j=1}^N x_i \times \text{WSSD}^-_{,j}}{\sum_{j=1}^N \text{WSSD}^-_{,j}} dt, \quad i = 1, 2, 3. \quad (7)$$

2.4. CFD Modeling. The conservation equations for 3D unsteady laminar flow with rigid wall boundary conditions were solved using an open source CFD code (OpenFOAM, <http://www.openfoam.com/>). The general form of the unsteady state equation is represented as

$$\begin{aligned} & \frac{\partial}{\partial t} (\rho u_i) + \frac{\partial}{\partial x_j} (\rho u_i u_j) \\ & = -\frac{\partial p}{\partial x_i} + \frac{\partial}{\partial x_j} \left[\mu \left(\frac{\partial u_i}{\partial x_j} + \frac{\partial u_j}{\partial x_i} \right) \right] + S_i, \quad (8) \\ & \frac{\partial p}{\partial t} + \frac{\partial}{\partial x_j} (\rho u_j) = 0, \end{aligned}$$

where ρ represents the density, P is the static pressure, $u_{i,j}$ are velocity components, and μ is the dynamic viscosity. Being a second-order derivative of velocity, WSSD needs a highly accurate scheme to compute. In this study, a fourth-order

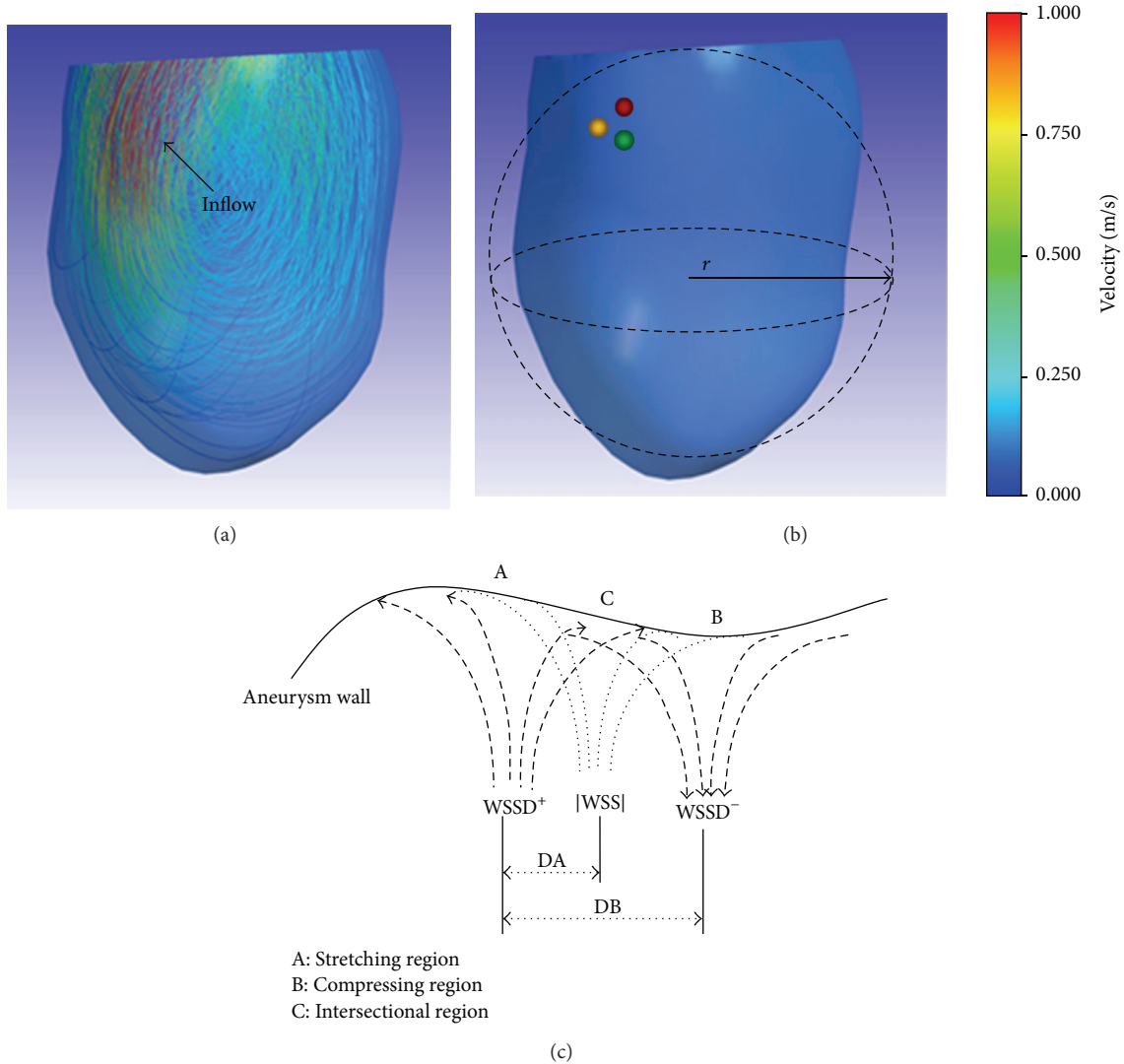


FIGURE 1: Inflow and stress centres. (a) Flow pattern. (b) Wave centres of WSSD and |WSS|; red ball: the coordinate center of WSSD⁺, green ball: the coordinate center of WSSD⁻, and yellow ball: the coordinate center of |WSS|. (c) Different actions of WSSD⁺ and WSSD⁻.

difference scheme was used to discretize the diffusion term in (8) (OpenFOAM, <http://www.openfoam.com/>). Blood was assumed to be a Newtonian fluid with density of 1050 [kg/m³] and dynamic viscosity of 0.0036 [Pa · s].

In order to reduce the entrance/exit effect of CFD, the inlet and outlet of the calculation domain were extended distally in the normal downstream direction to about 10 cm. At the inlet boundary, considering that the ICA of those patients were of similar size, uniform velocity calculated from the average of ICA flow ratios (measured to be approximately 125 mL/min) [21] was introduced as the boundary condition. A zero pressure condition was used at the outlets. In the post process, nondimensional analysis was conducted to further minimize the numerical uncertainties. Grid independent study was performed in our previous publications [22, 23]. In order to accurately measure WSS at near-wall region, the body-fitted prism layers were generated near the vessel walls to improve the resolution of the relevant scales in fluid

motion. There were five layers generated with an average nodal space, increasing by a ratio of 1.2. The distance from the first layer to the vessel surface was fixed at 0.02 mm.

3. Results

For the ruptured case 1, both |WSS| and WSSD at the systolic peak ($T = 0.27$ s) are shown in Figure 2. The magnitudes of |WSS| in two locations marked by a circle were close to each other (about 1.5 Pa). However, the values of WSSD of both regions were different; in the left panel where WSS was compressing the aneurysm surface, the WSSD had a negative value (about -1000 Pa/m), while, in the right panel where WSS was stretching the aneurysm surface, the WSSD had a positive value (about 1500 Pa/m). This indicates that only the magnitude of WSS cannot directly estimate the risk of aneurysm rupture; the direction of WSS must be also considered.

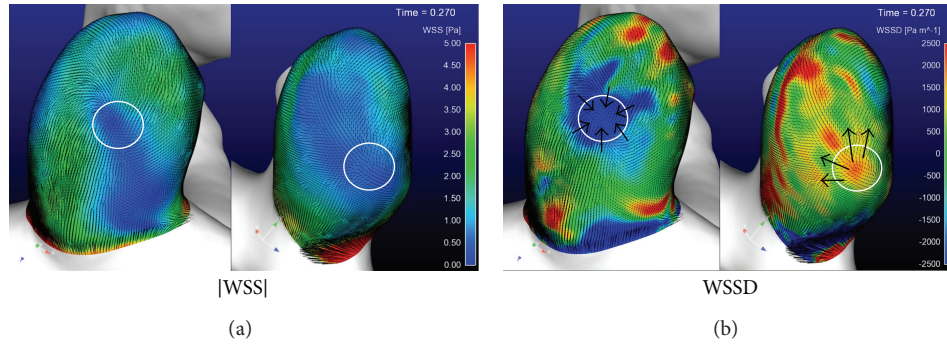


FIGURE 2: |WSS| and WSSD distributions at the systolic for a ruptured aneurysm.

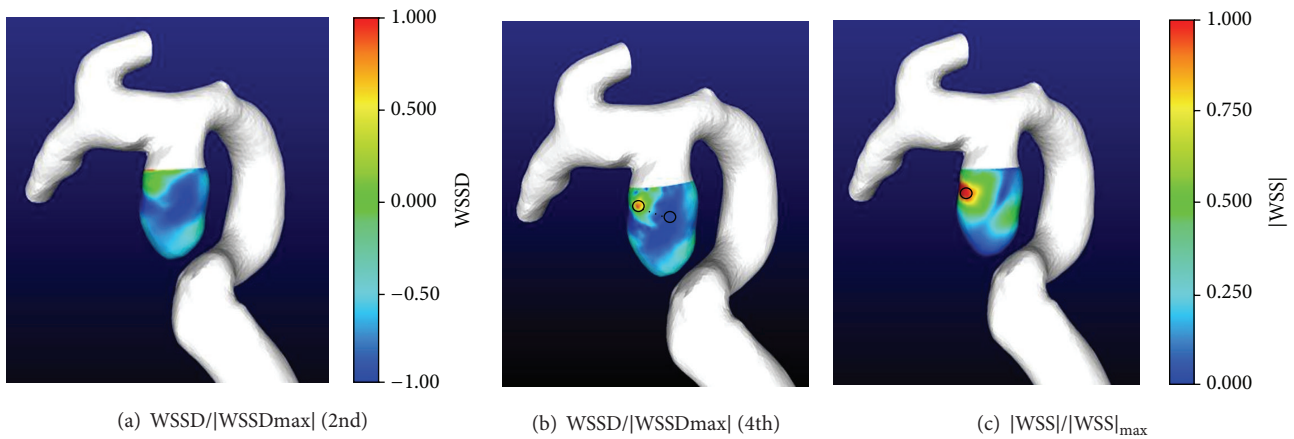


FIGURE 3: Ruptured case (case 1).

Figure 3 shows that the nondimensional distribution of WSSD and |WSS| for ruptured case 1. WSSD, calculated using a fourth-order scheme (Figure 3(b)), had a higher spatial resolution than that obtained by using second-order scheme (Figure 3(a)). The distances from the wave center of WSSD⁺ to |WSS| and WSSD⁻ were 0.4 mm and 0.6 mm, respectively. For an effective radius of aneurysm of 3 mm, (2) and (6) give the values of RFA and RFB to be 7.5 and 5.0, respectively.

For the same ruptured case, the variation of nondimensional |WSS| and WSSD⁺ at the nearest surface point to the |WSS| center is shown in Figure 4(a). At this point the maximum |WSS| and WSSD⁺ occur at the same time. As a result, the stretching effect of WSS reached the maximum. Figure 4(b) shows that WSSD was observed to change four times from “stretching” to “compression” during one cardiac cycle, at the intersection region of WSSD⁺ and WSSD⁻.

The computed results of an unruptured aneurysm (case 4) are shown in Figure 5. WSSD calculated using fourth-order scheme (Figure 5(b)) again had higher spatial resolution than that obtained by using second-order scheme (Figure 5(a)). The distance from wave centers of WSSD⁺ to WSSD⁻ reached 1.5 mm. Comparing Figures 5(b) and 5(c), the wave centres of |WSS| and WSSD⁺ are separate, with the distance in between being 1.34 mm. For the effective radius of aneurysm (4.0 mm), the calculated RFA and RFB are 2.6 and 1.7, respectively.

For the same unruptured case, the nondimensional |WSS| and WSSD⁺ at the nearest surface point to the |WSS| center is shown in Figure 6(a). Though the peak of nondimensional WSS and WSSD⁺ occurs at the same time, it is seen that WSSD⁺ reaches only 50% of its peak value; that is, the stretching effect does not reach the maximum. Figure 6(b) shows the results of WSSD at the intersectional region of WSSD⁺ and WSSD⁻. WSS only alternated 2 times between “stretching” and “compression” in one cardiac cycle.

The comparison of cases 1 and 4 validates our hypothesis that the value of RFA represents the “stretching” effect, and the value of RFB represents the directional change of WSS. Both RFA and RFB for ruptured case 1 are higher than those for unruptured case 4. Figure 7(a) shows the results of averaged RFA of ruptured and unruptured groups. For ruptured aneurysms, RFA reached 6.0 ± 2.3 , about 2 times that of unruptured aneurysms (3.0 ± 1.0). Similarly, the RFB of ruptured aneurysms was 3.8 ± 1.2 , again about 2 times that of unruptured aneurysms (2.0 ± 1.7) (Figure 7(b)).

4. Discussion

4.1. WSS and Aneurysm Rupture. How WSS results in aneurysm rupture has long been discussed in previous studies. It is believed that magnitude of wall shear stress |WSS| alone

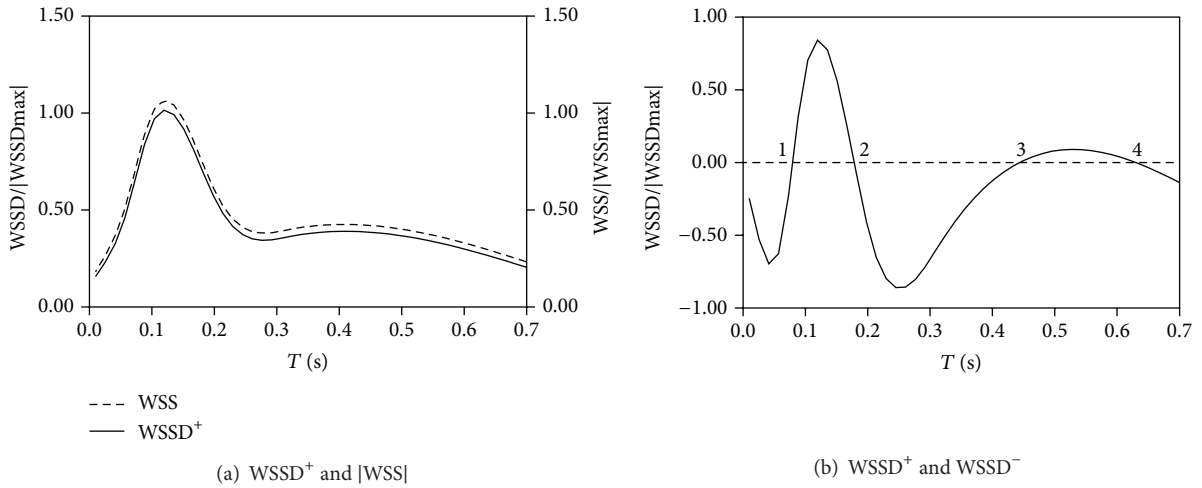


FIGURE 4: WSSD versus time for case 1.

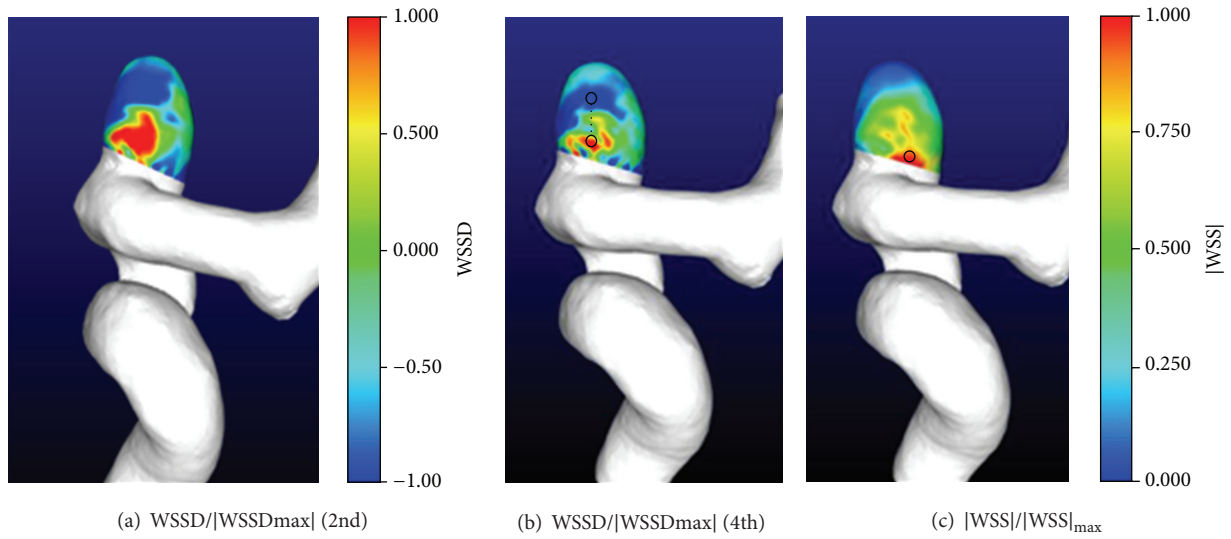


FIGURE 5: Unruptured case (case 4).

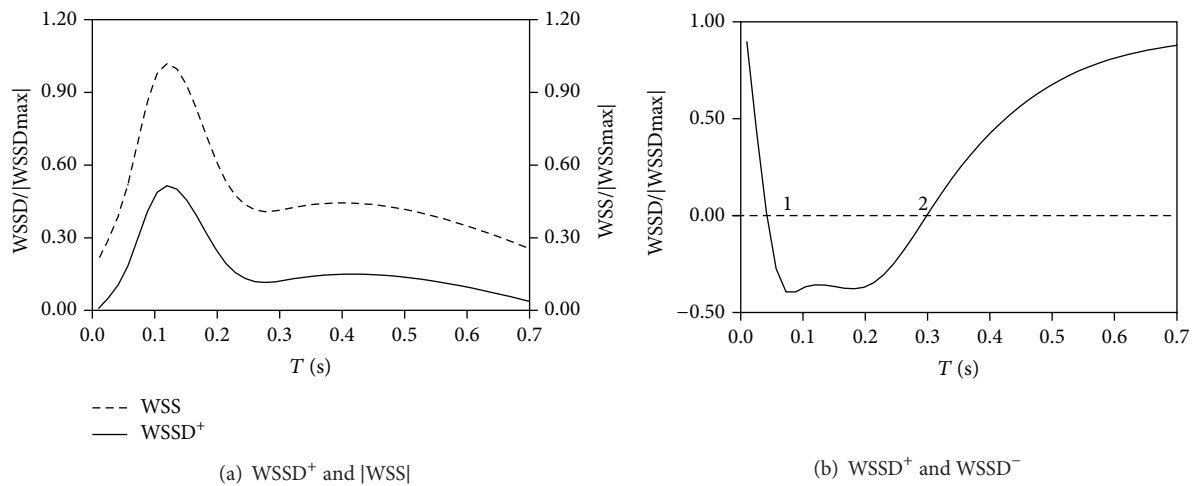


FIGURE 6: WSSD versus time for case 4.

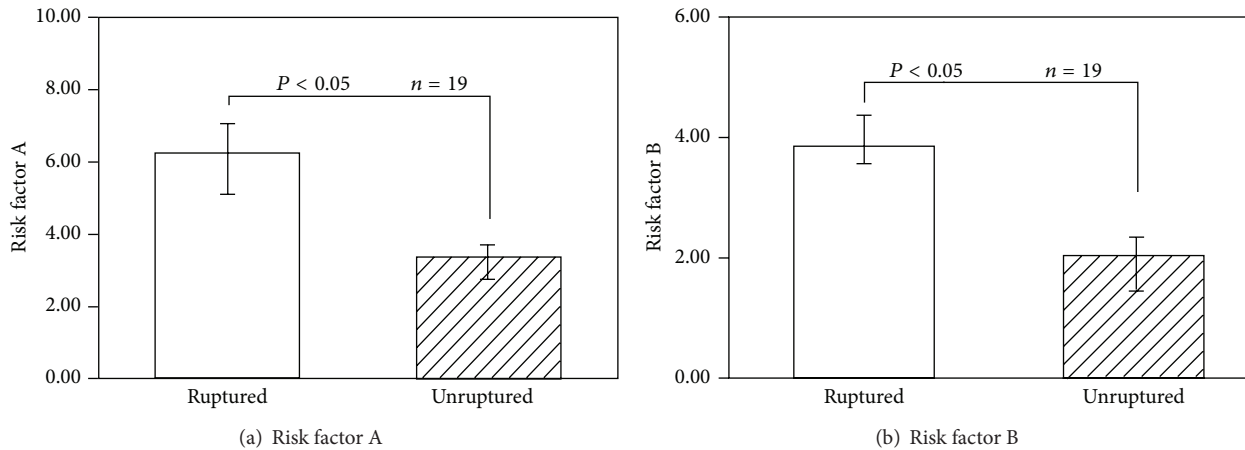


FIGURE 7: Risk factors.

cannot reasonably predict the aneurysm rupture as it does not include any directional information of WSS and therefore is not able to identify whether the WSS generated is stretching or compressing the aneurysm luminal surface. Physiological studies have likewise shown that the endothelial cells lining blood vessels are subjected to WSS and responded to both magnitude and directional changes [8, 24, 25]. In any specific area, the overall effect of WSS may result in a stretching or compressive force upon the intima surface, contributing to the different responses exhibited by the endothelial cells. This response may lead to the appearance of self-sustaining aneurysm remodelling, resulting in further aneurysm growth and rupture [26].

Oscillatory shear index (OSI) has been proposed to measure the directional changes of WSS, with high OSI correlating to aneurysm rupture [9, 27]. It should likewise be noted that OSI is only able to depict the directional change of WSS at a point and is not able to indicate whether the force generated is tensile or compressive. To address this issue, a gradient oscillatory number (GON) was developed to test the number of incidences in which the force generated varied from tensile to compressive at a certain point [28]. However, for both OSI and GON, the effect of WSS magnitude was counteracted in calculation. The combination of the high magnitude of WSS and high wall shear stress gradient (WSSG) was thus proposed to estimate the remodelling of vessel walls in response to aneurysm formation. Current reports have indicated that the intersectional area of high WSS and high gradients in WSS may represent a “dangerous” hemodynamic condition for aneurysm formation [19].

Previous research has implied that WSS magnitude alone cannot fully explain the influence of WSS on the rupture of aneurysms. WSS magnitude, gradient, and direction must all be completely and comprehensively examined, in order to reasonably estimate the risk of aneurysm formation and rupture.

4.2. What Are the Contributions of WSSD Based Analysis? In the current study, we proposed a new concept of WSSD. Compared with $|WSS|$, WSSD considers the directions of WSS.

Compared with OSI, WSSD can identify the performance of WSS at $WSSD^+$ region; WSS is stretching while, at $WSSD^-$ region, WSS is compressing the aneurysm luminal surface. The magnitude of WSSD represents the strength of stretching or compression.

Recent study has shown that the combination of high $|WSS|$ and high WSSG may result in the aneurysm rupture. We showed similar results; the combination of high $|WSS|$ and high $WSSD^+$ may result in the aneurysm rupture. It is worth to know the difference between WSSG and $WSSD^+$. The former only represents the gradient of the magnitude of WSS but does not include WSS directions. The latter is in the same order of WSSG but can identify that, at the dangerous location, high $|WSS|$ regions must stretch the aneurysm luminal surface. At low $|WSS|$ regions, high OSI points are considered to be dangerous for aneurysm rupture, as WSS changes its directions at those points [29]. In this study, we further identify that if the directional change of WSS results in the alternation of a specific area between “tensile” ($WSSD^+$) to “compressive” ($WSSD^-$), it is more likely to be dangerous. In one word, WSSD based analysis further highlights the dangerous factors.

4.3. The Limitation of the Current Study. One of the limitations of this study is the small number of ruptured cases examined. We should highlight that the aneurysm cases were obtained from long-term patient follow-up observations conducted in the clinic. The ruptured aneurysms were strictly selected from images taken prior to rupture (not after rupture for most other studies). The selected patients were all of similar ages, all being female, nonsmokers with no family history of aneurysm rupture. The aneurysms were located at the same loci (ICA) and exhibited similar sizes. We are moreover keeping a record of all patient data and will continually introduce new cases into future research.

5. Conclusion

A new concept of WSSD was proposed in this paper, which considers both WSS magnitude and effective directions in the

prediction of aneurysm rupture. Based on WSSD, two risk factors RFA and RFB are derived, which can be calculated through the use of CFD with a high-order scheme. Our results revealed that aneurysms with high values of RFA and RFB are under high risk of rupture.

Acknowledgment

This study was partially supported by the Australian Research Council Discovery Project, DP1112985.

References

- [1] L. L. Teunissen, G. J. E. Rinkel, A. Algra, and J. van Gijn, "Risk factors for subarachnoid hemorrhage a systematic review," *Stroke*, vol. 27, no. 3, pp. 544–549, 1996.
- [2] M. H. Vlak, G. J. E. Rinkel, P. Greebe, J. G. Van Der Bom, and A. Algra, "Trigger factors and their attributable risk for rupture of intracranial aneurysms: a case-crossover study," *Stroke*, vol. 42, no. 7, pp. 1878–1882, 2011.
- [3] G. J. E. Rinkel, M. Djibuti, A. Algra, and J. Van Gijn, "Prevalence and risk of rupture of intracranial aneurysms: a systematic review," *Stroke*, vol. 29, no. 1, pp. 251–256, 1998.
- [4] N. K. de Rooij, F. H. H. Linn, J. A. van der Plas, A. Algra, and G. J. E. Rinkel, "Incidence of subarachnoid haemorrhage: a systematic review with emphasis on region, age, gender and time trends," *Journal of Neurology, Neurosurgery and Psychiatry*, vol. 78, no. 12, pp. 1365–1372, 2007.
- [5] L. H. Phillips, J. P. Whisnant, W. M. O'Fallon, and T. M. Sundt Jr., "The unchanging pattern of subarachnoid hemorrhage in a community," *Neurology*, vol. 30, no. 10, pp. 1034–1040, 1980.
- [6] N. F. Kassell, J. C. Torner, E. C. Haley Jr., J. A. Jane, H. P. Adams, and G. L. Kongable, "The International cooperative study on the timing of aneurysm surgery. Part I: overall management results," *Journal of Neurosurgery*, vol. 73, no. 1, pp. 18–36, 1990.
- [7] M. J. Wermer, I. C. van der Schaaf, A. Algra, and G. J. E. Rinkel, "Risk of rupture of unruptured intracranial aneurysms in relation to patient and aneurysm characteristics: an updated meta-analysis," *Stroke*, vol. 38, no. 4, pp. 1404–1410, 2007.
- [8] M. I. Baharoglu, C. M. Schirmer, D. A. Hoit, B. Gao, and A. M. Malek, "Aneurysm inflow-angle as a discriminant for rupture in sidewall cerebral aneurysms: morphometric and computational fluid dynamic analysis," *Stroke*, vol. 41, no. 7, pp. 1423–1430, 2010.
- [9] J. Xiang, S. K. Natarajan, M. Tremmel et al., "Hemodynamic-morphologic discriminants for intracranial aneurysm rupture," *Stroke*, vol. 42, no. 1, pp. 144–152, 2011.
- [10] T. R. Forget, R. Benitez, E. Veznedaroglu et al., "A review of size and location of ruptured intracranial aneurysms," *Neurosurgery*, vol. 49, no. 6, pp. 1322–1326, 2001.
- [11] S. Dhar, M. Tremmel, J. Mocco et al., "Morphology parameters for intracranial aneurysm rupture risk assessment," *Neurosurgery*, vol. 63, no. 2, pp. 185–196, 2008.
- [12] M. Rahman, J. Smietana, E. Hauck et al., "Size ratio correlates with intracranial aneurysm rupture status: a prospective study," *Stroke*, vol. 41, no. 5, pp. 916–920, 2010.
- [13] M. Shojima, M. Oshima, K. Takagi et al., "Magnitude and role of wall shear stress on cerebral aneurysm: computational fluid dynamic study of 20 middle cerebral artery aneurysms," *Stroke*, vol. 35, no. 11, pp. 2500–2505, 2004.
- [14] J. M. Dolan, J. Kolega, and H. Meng, "High wall shear stress and spatial gradients in vascular pathology: a review," *Annals of Biomedical Engineering*, vol. 41, no. 7, pp. 1411–1427, 2013.
- [15] J. R. Cebal, M. A. Castro, J. E. Burgess, R. S. Pergolizzi, M. J. Sheridan, and C. M. Putman, "Characterization of cerebral aneurysms for assessing risk of rupture by using patient-specific computational hemodynamics models," *American Journal of Neuroradiology*, vol. 26, no. 10, pp. 2550–2559, 2005.
- [16] M. Shojima, M. Oshima, K. Takagi et al., "Role of the blood-stream impacting force and the local pressure elevation in the rupture of cerebral aneurysms," *Stroke*, vol. 36, no. 9, pp. 1933–1938, 2005.
- [17] T. Hassan, E. V. Timofeev, T. Saito et al., "A proposed parent vessel geometry-based categorization of saccular intracranial aneurysms: computational flow dynamics analysis of the risk factors for lesion rupture," *Journal of Neurosurgery*, vol. 103, no. 4, pp. 662–680, 2005.
- [18] L. Goubergrits, J. Schaller, U. Kertzscher et al., "Statistical wall shear stress maps of ruptured and unruptured middle cerebral artery aneurysms," *Journal of the Royal Society Interface*, vol. 9, no. 69, pp. 677–688, 2012.
- [19] H. Meng, Z. Wang, Y. Hoi et al., "Complex hemodynamics at the apex of an arterial bifurcation induces vascular remodeling resembling cerebral aneurysm initiation," *Stroke*, vol. 38, no. 6, pp. 1924–1931, 2007.
- [20] O. Traub and B. C. Berk, "Laminar shear stress: mechanisms by which endothelial cells transduce an atheroprotective force," *Arteriosclerosis, Thrombosis, and Vascular Biology*, vol. 18, no. 5, pp. 677–685, 1998.
- [21] Y. Qian, H. Takao, M. Umezu, and Y. Murayama, "Risk analysis of unruptured aneurysms using computational fluid dynamics technology: preliminary results," *American Journal of Neuroradiology*, vol. 32, no. 10, pp. 1948–1955, 2011.
- [22] Y. Qian, J. L. Liu, K. Itatani, K. Miyaji, and M. Umezu, "Computational hemodynamic analysis in congenital heart disease: simulation of the Norwood procedure," *Annals of Biomedical Engineering*, vol. 38, no. 7, pp. 2302–2313, 2010.
- [23] Y. Zhang, T. Furusawa, S. F. Sia, M. Umezu, and Y. Qian, "Proposition of an outflow boundary approach for carotid artery stenosis CFD simulation," *Computer Methods in Biomechanics and Biomedical Engineering*, vol. 16, no. 5, pp. 488–494, 2013.
- [24] A. B. Fisher, S. Chien, A. I. Barakat, and R. M. Nerem, "Endothelial cellular response to altered shear stress," *American Journal of Physiology*, vol. 281, no. 3, pp. L529–L533, 2001.
- [25] Z. Zeng, B. J. Chung, D. Michael, and A. M. Robertson, "An in-vitro device for evaluation of cellular response to flows found at the apex of bifurcations," in *Advances in Mathematical Fluid Mechanics*, pp. 631–667, 2009.
- [26] H. Meng, E. Metaxa, L. Gao et al., "Progressive aneurysm development following hemodynamic insult: laboratory investigation," *Journal of Neurosurgery*, vol. 114, no. 4, pp. 1095–1103, 2011.
- [27] G. Lu, L. Huang, X. L. Zhang et al., "Influence of hemodynamic factors on rupture of intracranial aneurysms: patient-specific 3D mirror aneurysms model computational fluid dynamics simulation," *American Journal of Neuroradiology*, vol. 32, no. 7, pp. 1255–1261, 2011.
- [28] Y. Shimogonya, T. Ishikawa, Y. Imai, N. Matsuki, and T. Yamaguchi, "Can temporal fluctuation in spatial wall shear stress gradient initiate a cerebral aneurysm? A proposed novel

hemodynamic index, the gradient oscillatory number (GON),” *Journal of Biomechanics*, vol. 42, no. 4, pp. 550–554, 2009.

- [29] H. Meng, V. M. Tutino, J. Xiang, and A. Siddiqui, “High WSS or low WSS? Complex interactions of hemodynamics with intracranial aneurysm initiation, growth, and rupture: toward a unifying hypothesis,” *American Journal of Neuroradiology*, 2013.

Research Article

Why Is ABI Effective in Detecting Vascular Stenosis? Investigation Based on Multibranch Hemodynamic Model

Xiaoyun Li,¹ Ling Wang,¹ Chi Zhang,¹ Shuyu Li,¹ Fang Pu,^{1,2} Yubo Fan,^{1,2} and Deyu Li^{1,2}

¹ Key Laboratory for Biomechanics and Mechanobiology of Ministry of Education, School of Biological Science and Medical Engineering, Beihang University, Beijing 100191, China

² State Key Laboratory of Virtual Reality Technology and Systems, Beihang University, Beijing 100191, China

Correspondence should be addressed to Deyu Li; deyuli@buaa.edu.cn

Received 5 June 2013; Accepted 1 August 2013

Academic Editors: H.-C. Han, M. Ohta, and A. Qiao

Copyright © 2013 Xiaoyun Li et al. This is an open access article distributed under the Creative Commons Attribution License, which permits unrestricted use, distribution, and reproduction in any medium, provided the original work is properly cited.

The ankle-brachial index (ABI), defined as the ratio of systolic pressure in the ankle arteries and that in the brachial artery, was a useful noninvasive method to detect arterial stenoses. There had been a lot of researches about clinical regularities of ABI; however, mechanism studies were less addressed. For the purpose of a better understanding of the correlation between vascular stenoses and ABI, a computational model for simulating blood pressure and flow propagation in various arterial stenosis circumstances was developed with a detailed compartmental description of the heart and main arteries. Particular attention was paid to the analysis of effects of vascular stenoses in different large-sized arteries on ABI in theory. Moreover, the variation of ABI during the increase of the stenosis severity was also studied. Results showed that stenoses in lower limb arteries, as well as, brachial artery, caused different variations of blood pressure in ankle and brachial arteries, resulting in a significant change of ABI. Furthermore, the variation of ABI became faster when the severity of the stenosis increased, validating that ABI was more sensitive to severe stenoses than to mild/moderate ones. All these findings revealed the reason why ABI was an effective index for detecting stenoses, especially in lower limb arteries.

1. Introduction

The partial occlusion of arteries due to stenotic obstruction is one of the most frequent cardiovascular diseases in human beings. The vascular stenosis frequently affects the blood pressure and flow of large and middle-sized arteries. Mathematical models based on one-dimensional flow equations are usually used to study the hemodynamic mechanism for the effects of vascular stenoses on cardiovascular system. Young et al. [1–3] developed finite element models including nonlinearities arising from geometry and material properties to analyze the characteristics of blood flow and pressure decrease caused by an arterial stenosis. Garcia et al. [4] and Singh and Shah [5] analyzed the decreases of instantaneous maximal transvalvular pressure in aortic stenosis using numerical models. Pralhad and Schultz [6] and Feng et al. [7] studied influences on blood cellular constituents and related blood diseases on molecular level. Models used in those studies were mostly applied to the analysis of hemodynamic

effects of stenoses on blood pressure decreases or flow characteristics. However, few studies focused on the related detective indexes of the vascular stenosis, such as the ankle-brachial index (ABI).

ABI, defined as the ratio of systolic pressure in the ankle arteries (the posterior tibial artery in this model) and systolic pressure in the brachial artery (Figure 1), was an important noninvasive measurement for the detection of arterial obstructive disease, especially for the lower extremity arterial stenosis [8–10]. The American College of Cardiology (ACC) and the American Heart Association (AHA) proposed to grade ABI into four levels [8], as shown in the diagram below. ACC/AHA had recommended the evaluation standards of normal ABI to be 0.91~1.30, and also a cutoff of 0.90 to define a low ABI value. The ABI value greater than 1.30 indicated that the vascular was uncompressible, suggesting that vascular calcification might have occurred. The ABI was generally unreliable for stenoses detection in such situations. The ABI value that ranged from 0.41 to 0.90 predicted the presence of

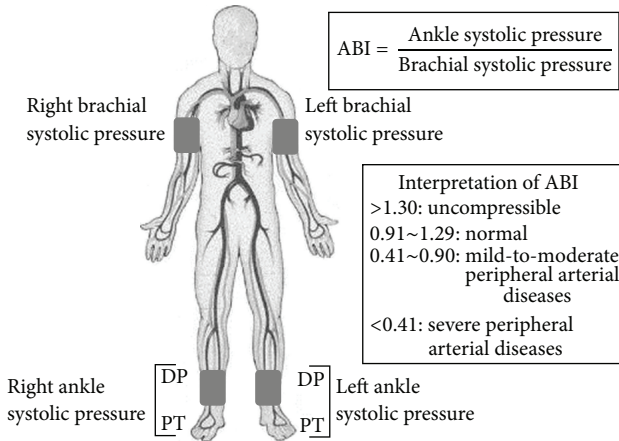


FIGURE 1: Measurement of the ankle-brachial index (ABI). DP indicates dorsalis pedis artery; PT, posterior tibial artery.

mild-to-moderate stenoses. Severe stenoses were diagnosed with the ABI value less than 0.41 in clinical data.

A lot of efforts have been made in the last decade to discuss the effectiveness and specificity of ABI in detecting arterial stenoses with clinical data. These researches have acquired a great number of insights into the sensitivity and specificity of ABI to diagnose peripheral arterial stenoses. Decrinis et al. [11] and Carter [12] found the sensitivity of ABI to be 94% and the specificity to be 100% by carrying out measurements in 146 limbs with angiographically documented arterial occlusive disease (AOD) and in 85 limbs without AOD. This strongly proved the validity of ABI in detecting arterial stenoses in lower extremity. Furthermore, many statistic studies were made to compare the sensitivity and the effectiveness of ABI in detecting arterial stenoses with different severities [13–15]. All experimental data agree to the point that the ABI measurement is a reliable noninvasive diagnostic method in assessing lower extremity arterial stenoses, which is alternative to conventional digital subtraction angiography (DSA). The ABI value shows a decreasing tendency with increasing severity of the stenoses in patients with peripheral arterial stenotic diseases. However, these findings are just clinical regularities, lacking the mechanism study to interpret these situations.

The present study is thus performed to develop a computational multibranch model of the entire cardiovascular system including typical arterial units of lower/upper limb. The model is used to investigate the correlation between ABI and the stenosis in theory. The influences of stenoses located in different sites of the cardiovascular system on ABI are discussed in this paper, as well as the variation tendency of ABI value caused by the stenosis with the increasing severity.

2. Methods

A lumped parameter multibranch model with 17 arterial units was developed to simulate the pulse wave propagation of the cardiovascular system. Construction of the model was implemented based on a phenomenological characterization

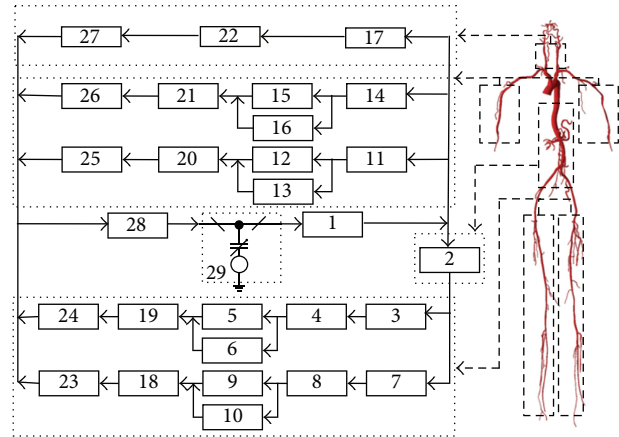


FIGURE 2: The electric analog circuit model of the entire cardiovascular system. Each component is comprised of a compliance variable C , a resistance R , and an inductance L (1: aorta (a); 2: thoracic and abdominal aortae (l); 3/7: left/right femoral artery (afl/afr); 4/8: left/right popliteal artery (apl/apr); 5/9: left/right posterior tibial artery (atl/atr); 6/10: other left/right lower limb arteries (all/alr); 11/14: left/right brachial artery (abl/abr); 12/15: left/right radial artery (arl/arr); 13/16: left/right ulnar arteries (aul/aur); 17: carotid artery (ac); 18/19: left/right lower limb capillaries (alpl/alpr); 20/21: left/right upper limb capillaries (aupl/aupr); 22: brain (acp); 23/24: left/right lower limb veins (vll/vlr); 25/26: left/right upper limb veins (vul/vur); 27: jugular veins (vc); 28: system vena (ve); 29: C_{lv} represents the compliance of the left ventricular). The effects of inertia for veins are not considered in this model.

of hemodynamics using an electrical analog method. It was assumed that human body was completely symmetric and that the cardiovascular system could be represented by a lumped parameter model. Another assumption was that the blood was a Newtonian fluid and that the dispersed arterial networks could be modeled using linear circuit elements [19, 20]. Blood pressure P (mmHg) corresponded to voltage, and flow rate Q (mL/s) was analogous to the current. Compliance of the artery played the role of capacitances C (mL/mmHg). R (mmHg·s/mL) and L (mmHg·s²/mL) represented impedance and inertia of the blood flow, respectively [20–22]. Based on the above assumptions, the cardiovascular system was depicted by the electrical circuit shown in Figure 2.

2.1. Model of the Heart. An elastic model was defined to predict blood pressure of the left ventricular given as follows:

$$P_{lv}(t) = E_{lv}(t) * (V_{lv} - V_d) + P_{th}, \quad (1)$$

where V_{lv} (mL) is the stressed ventricular volume and V_d (mL) is a constant which is referred to as the ventricular volume at zero diastolic pressure. P_{th} (mmHg) stands for the intrapleural pressure. E_{lv} (mmHg/mL) represents the time-varying elasticity of the left ventricular.

Elastance-based model of the ventricles had been widely adopted since firstly proposed by Suga et al. in the 1970s

TABLE 1: Physiologic geometry data of main arteries in the model.

No.	Arterial unit	Length l (cm)	Radius r (cm)	Thickness h (cm)	Elasticity E ($\times 10^6$ dyne/cm)
1	Brachial artery	23.5	0.2575	0.0525	4
2	Radial artery	23.4	0.1600	0.0430	8
3	Ulnar artery	23.7	0.1970	0.0470	8
4	Femoral artery	35.4	0.2400	0.0500	5
5	Popliteal artery	18.8	0.2000	0.0485	6
6	Posterior tibial artery	32.2	0.1800	0.0450	16
7	Anterior tibial artery 1	2.5	0.1300	0.0390	16
	Anterior tibial artery 2	30.0	0.1000	0.0200	16
8	Peroneal artery	31.8	0.1300	0.0290	16
9	Thoracic aorta	15.6	0.9830	0.1173	4
10	Abdominal aorta	15.9	0.6700	0.0893	4

TABLE 2: Values of the parameters used in the heart model and the cardiac valve model [16–18].

No.	Parameter	Value	Unit
1	Cl_{ed} (end-diastolic compliance of the left ventricle)	10	mL/mmHg
2	Cl_{es} (end-systolic compliance of the left ventricle)	0.4	mL/mmHg
3	P_{th} (intrapleural pressure)	-4	mmHg
4	V_d (ventricular volume at zero diastolic pressure)	10	mL
5	$R_{mv,open}$ (resistance value of the open mitral valve)	0.014	mmHg-s/mL
6	$R_{av,open}$ (resistance value of the open aortic valve)	0.006	mmHg-s/mL
7	T (cardiac cycle)	0.8	s

[23, 24]. In this study, the idealized time evolution of the elastance function was used as follow [20]:

$$E_{lv}(t) = \begin{cases} \frac{1}{2} \left(\frac{1}{Cl_{es}} - \frac{1}{Cl_{ed}} \right) * \left(1 - \cos \left(\frac{\pi(t - t_i)}{T_s} \right) \right), & t_i \leq t \leq t_i + T_s, \\ \frac{1}{2} \left(\frac{1}{Cl_{es}} - \frac{1}{Cl_{ed}} \right) * \left(1 + \cos \left(\frac{2\pi(t - (t_i + T_s))}{T_s} \right) \right), & t_i + T_s \leq t \leq t_i + T_s + T_r, \\ \frac{1}{Cl_{ed}}, & t_i + T_s + T_r \leq t \leq t_{i+1}, \end{cases} \quad (2)$$

where the subscript i refers to the i th cardiac cycle. Cl_{es} and Cl_{ed} are values of end-systolic compliance and end-diastolic compliance, respectively. Furthermore, T_s and T_r respectively, stand for the systolic time period and the time for

isovolumetric relaxation, which are functions of the cardiac cycle T (s):

$$T_s = 0.3\sqrt{T}, \quad T_r = \frac{T_s}{2} = 0.3\frac{\sqrt{T}}{2}. \quad (3)$$

Values of the parameters used in the heart model mentioned above (Cl_{ed} , Cl_{es} , V_d , P_{th} and T) are listed in Table 2.

2.2. Model of the Cardiac Valves. Cardiac valves played an important role in the cardiovascular system to ensure the blood flowing in the correct direction. A time-varying resistance model was developed to simulate the effect of the valves, which controlled the blood flow into (the mitral valve) and out of (the aortic valve) the left ventricle and it was described as [16, 25]:

$$R_{mv} = \min(R_{mv,open} + \exp(-2(P_{ve} - P_{lv})), 20), \quad (4)$$

$$R_{av} = \min(R_{av,open} + \exp(-2(P_{lv} - P_a)), 20),$$

where P_{lv} , P_{ve} , and P_a stand for the blood pressure of the left ventricle, the system vena, and aorta, respectively. $R_{mv,open}/R_{av,open}$ represents the baseline resistance value (seen in Table 2) when the mitral/aortic valve is opened. Accordingly, a small resistance is defined to depict the “open” valve, and a several orders larger resistance is used to simulate the “closed” valve.

2.3. Model of the Blood Vessel. In this model, an electrical circuit composed of linear electric elements was used to depict the cardiovascular system. For each of the arterial and venous units, the electric circuit model of the vascular was simulated as in Figure 3.

Differential equations were obtained by formulating the mass and momentum conservations, as follows:

$$\begin{aligned} \frac{dP_o}{dt} &= \frac{Q_i - Q_o}{C}, \\ \frac{dQ_i}{dt} &= \frac{P_i - P_o - Q_i * R}{L}, \end{aligned} \quad (5)$$

where Q_i and Q_o are inflow and outflow of the related vessel, respectively. Similarly, P_i and P_o are blood pressure upstream and downstream of the related vessel, respectively.

Blocked blood vessels with various stenosis severities were simulated in order to account for the correlation between vascular stenoses and ABI. The stenosis severity α was defined as the percentage reduction in cross-sectional area of the related vessel [26] as follows:

$$\alpha = \left(1 - \frac{A_s}{A_0}\right) \times 100\%, \quad (6)$$

where A_s and A_0 refer to cross-sectional areas of the stenotic and normal vessel segments.

2.4. Solution of the Model. The governing differential equations of the model were solved with the fourth-order Runge-Kutta algorithm. Simulations started from early systole when the ventricles began to contract. The cardiac cycle was set to be 0.8 s, and physiological conditions were fixed for all of the simulations. The geometrical parameters of the 17 arterial units were prescribed based on the data reported in [27, 28] (Table 1). Values of the resistance (R), capacitance (C), and inductance (L) for each artery were calculated using (7) [27, 29] based on the geometrical data as follows:

$$R = \frac{8\mu l}{\pi r^4}, \quad C = \frac{3\pi l r^3}{2Eh}, \quad L = \frac{9\rho l}{4\pi r^2}, \quad (7)$$

where l , r and h represent the length, radius and thickness of the vessel, respectively; E is the elastic parameter of the vascular; ρ is the blood density; ν is the viscosity of the blood. The values of ρ and ν are set as 1.06 g/mL and 0.004 Pa-s respectively, in this study.

2.5. Sensitivity Analysis of the Model. To better understand the stability of the parameters in the model, the sensitivity of the model output vectors on each of the parameters was analyzed. Basic methods for differential equation analysis [30, 31] were used to obtain the sensitivity equations of our cardiovascular system model. Following the algorithm developed by Ellwein et al. [16], the relative sensitivity $S_{i,j}$ of the output vector y_i to the parameter β_j was defined by

$$S_{i,j} = \frac{\partial y_i}{\partial \beta_j} \frac{\beta_j}{y_i} \Big|_{\beta=\beta_0}, \quad \beta_j, y_i \neq 0, \quad (8)$$

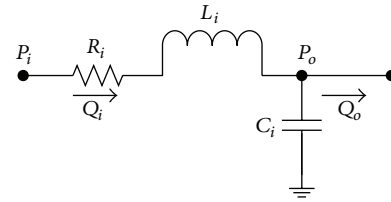


FIGURE 3: Electric circuit analog of the blood vessel segment. Flow through the model is defined by Q (mL/s). Pressures related to each compartment are marked by P (mmHg). Resistors are denoted by R (mmHg-s/mL), while capacitors and inductances are denoted by C (mL/mmHg) and L (mmHg-s²/mL), respectively.

where y_i denotes the output vectors of the models, and here it refers to P_{abl}/P_{abr} , P_{arl}/P_{arr} , P_{afl}/P_{afr} , and P_{atl}/P_{atr} (blood pressure of left/right brachial, radial, femoral, and posterior tibial artery, resp.) which could be detected noninvasively; β_j denotes all the parameters in the model (resistances, capacitances and inductances); β_0 denotes the nominal values for the parameters. All of the variables are assumed to be continuous. Thus, $S_{i,j}$ could be expressed as a function of time.

Based on the above computations, an averaged relative sensitivity S_i was used to get the total sensitivity to the j th parameter β_j in the following form [16, 32]:

$$S_i = \frac{1}{N} \sum_{j=1}^N |S_{i,j}|. \quad (9)$$

3. Results

3.1. Validation of the Model. Blood pressure pulses at several typical sites of the cardiovascular system in normal cases were shown in Figure 4. On the whole, the pressure waveforms obtained by the model were similar to the vivo data reported by Sun et al. [33], Reymond [34], and Blanco et al. [35]. The pressure magnitudes and time-constants involved were reasonable, thus verifying that the results obtained by the simulation model were consistent with human physiological conditions.

To assess the sensitivity of the parameters, the indice S could be ranked into four classes as shown in Table 3 [32, 36]. The computational result showed that sensitivities of parameters in our model were mostly in grades I and II; only two parameters ($R_{mv,open}$ and $R_{av,open}$) were in grade III; thus, validated that our model was stable to simulate the pulse wave propagation in the cardiovascular system.

3.2. Sensitivity and Effectiveness of ABI. The computational model was applied further to study the influences on ABI of arterial stenoses located in femoral artery (no. 3), popliteal artery (no. 4), posterior tibial artery (no. 5), brachial artery (no. 11), radial artery (no. 12), and ulnar artery (no. 13), respectively. Moreover, the variation of ABI during the increase of the stenosis severity was also studied.

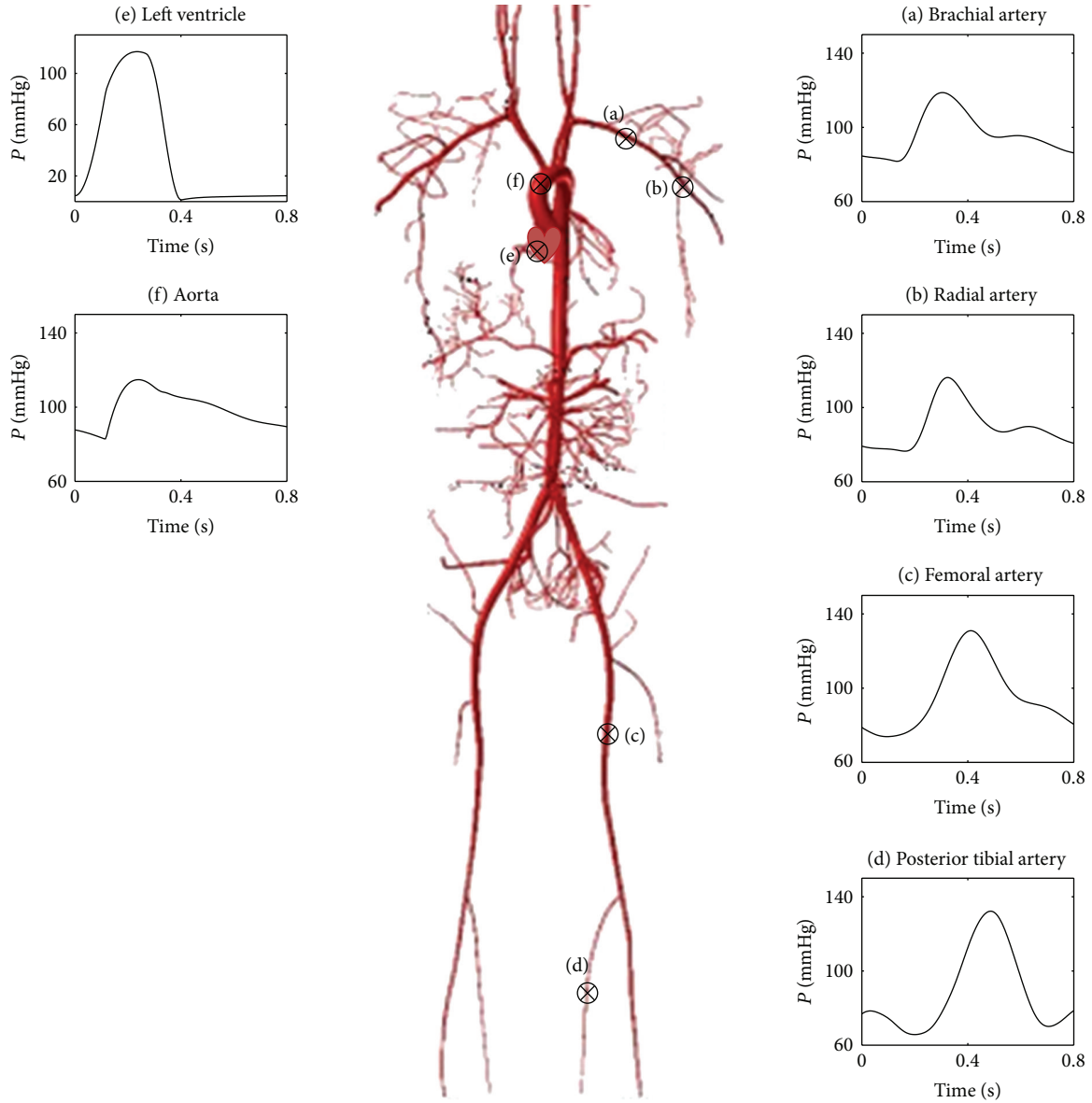


FIGURE 4: Blood pressure waveforms of the cardiovascular system in a single cardiac cycle.

TABLE 3: Sensitivity classes.

Class	Index	Sensitivity
I	$0.00 \leq S < 0.05$	Small to negligible
II	$0.05 \leq S < 0.20$	Medium
III	$0.20 \leq S < 1.00$	High
IV	$ S \geq 1.00$	Very high

3.2.1. Correlation between ABI and Stenosis Locations. This model was used to study influences on ABI of stenoses located in different arteries. The simulation result (Figure 5) showed that ABI was capable to diagnose arterial stenoses in lower extremity arteries (femoral artery, popliteal artery, and posterior tibial artery). However, there were limitations to detect arterial stenoses in upper limb, other than brachial

artery whose blood pressure directly affected ankle-brachial index calculations. It was difficult for ABI to detect radial and ulnar arterial stenoses for the reason that the relative decreases of brachial and posterior tibial systolic pressure were unobvious, as shown in Figure 6, which directly affected the result for ABI calculation in such vascular stenosis circumstances.

3.2.2. Tendency of ABI with Arterial Stenosis of Increasing Severity. As ABI was effective to detect arterial stenoses of lower extremity limb arteries as well as brachial artery, assessment of the tendency of ABI with arterial stenoses of different severities was studied. The arterial stenosis was graded into three levels in clinical data: mild stenosis (1%~29%), moderate stenosis (30%~69%), and severe stenosis (70%~99%). As Figure 7 showed, the decrease/increase of

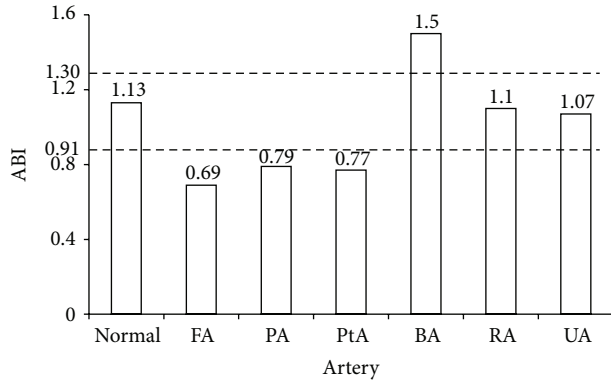


FIGURE 5: ABI for the normal case and for the stenosis cases with severities of 70% at 6 arteries, respectively. FA (femoral artery), PA (popliteal artery), PtA (posterior tibial artery), BA (brachial artery), RA (radial artery), and UA (ulnar artery) denote the locations of the stenoses. The dotted lines represent the evaluation standards of normal ABI (0.91~1.30) proposed by ACC/AHA. Vascular stenoses may have occurred if the value of ABI exceeds this range.

ABI became larger when severity of stenoses was located in lower/upper limb artery changing from mild to severe. This was because systolic blood pressures in brachial artery changed more dramatically than those in posterior tibial artery in various arterial stenoses circumstances as shown in Figure 8. That was to say, ABI was more sensitive to severe stenoses than to mild/moderate stenoses located in all of the four arteries, both the lower extremity arteries (femoral artery, popliteal artery and posterior tibial artery) and the upper limb artery (brachial artery).

4. Discussion

In the complex cardiovascular system, the hemodynamic influences of an arterial stenosis were closely related to the whole system. It was of great significance to detect arterial stenoses effectively and noninvasively for both the clinical diagnosis and the medical research. ABI, as a useful and a noninvasive detection method in clinical data, was proved to be effective and reliable in diagnosing arterial stenoses, especially for lower extremity arterial stenoses. Therefore, it was important to investigate the mechanism of ABI in detecting stenoses located in different sites of the cardiovascular system with various severities. Liang et al. [26] proposed that ABI was only effective for the stenosis present in the artery located in series with the ankle artery but parallel with the brachial artery. However, their research was based on study of stenoses located in aortic valvular, thoracic aorta, abdominal aorta, and so forth, without more analysis of stenoses located just in upper or lower limb arteries. There was little specific research about the distinction between diagnoses of stenoses located in lower limb arteries and in upper ones using ABI. The present study improved their study by constructing a computational multibranch model of the entire cardiovascular system clearly with several typical independent arterial units of upper and lower limbs.

Simulation results for the stenoses in six arteries showed that the ability of ABI to diagnose arterial stenoses depended strongly on the location where the stenosis occurred. ABI, as an index for assessing vascular stenoses, was effective for stenoses in lower extremity arteries (femoral artery, popliteal artery, and posterior tibial artery) and also brachial artery. However, the value of ABI was not able to predict stenoses of other upper limb arteries, such as radial and ulnar arterial stenoses. This was because the relative decreases of brachial and posterior tibial systolic pressure were unobvious (Figure 6), which directly affected the result for ABI calculation. It should be noted that there were limitations for ABI to predict brachial stenoses. The value of ABI could be more than 1.30, the upper bound of ABI, under the condition of severe brachial stenoses. Other imaging examination methods should be supplemented for the confirmation of brachial stenosis.

Our study also evidenced that the sensitivity and the effectiveness of ABI were higher to severe stenoses than to mild/moderate ones. This was because the changes of systolic blood pressures in brachial artery and posterior tibial artery that resulted from stenoses located in various lower limb arteries were different. Taking femoral arterial stenoses and popliteal arterial stenosis, for example (Figure 8), which did not affect the ABI calculation directly, the systolic blood pressure of posterior tibial artery was more sensitive than that of brachial artery to lower limb stenoses. Blood pressure of the posterior tibial artery changed more greatly when the stenosis severity increased from mild to severe. Accordingly, the variation of the ABI value became dramatical when it was calculated using the systolic blood pressure of posterior tibial artery divided by the systolic blood pressure of brachial artery. Therefore, the ABI, as a valid stenosis indicator, was more sensitive and effective to severe stenoses than to mild/moderate ones. The results were somehow supported by the clinical experimental data collected by Xu [15].

The present study was based on simulations for the cardiovascular system of a healthy adult without heart disease or other arterial diseases. However, the reality would be much more complicated by the idea that some changes of hemodynamic factors associated with a single stenosis in the study could be also caused by the presence of multiple arterial stenoses or other cardiac diseases. Furthermore, the variations of blood pressure might be underestimated, since the compensatory responses of the physiologic system to arterial stenoses were not considered. These limitations pointed to our future research, but they did not challenge the fundamental conclusions about the sensitivity and the effectiveness of ABI in detecting a single stenosis.

5. Conclusion

A lumped parameter multibranch model of the cardiovascular system including 17 arterial units based on first-order differential equations has been developed in this study. This computational model has explicitly accounted for the pulse wave propagation in the arterial system. Furthermore, the model includes a physiological description of dynamics as a

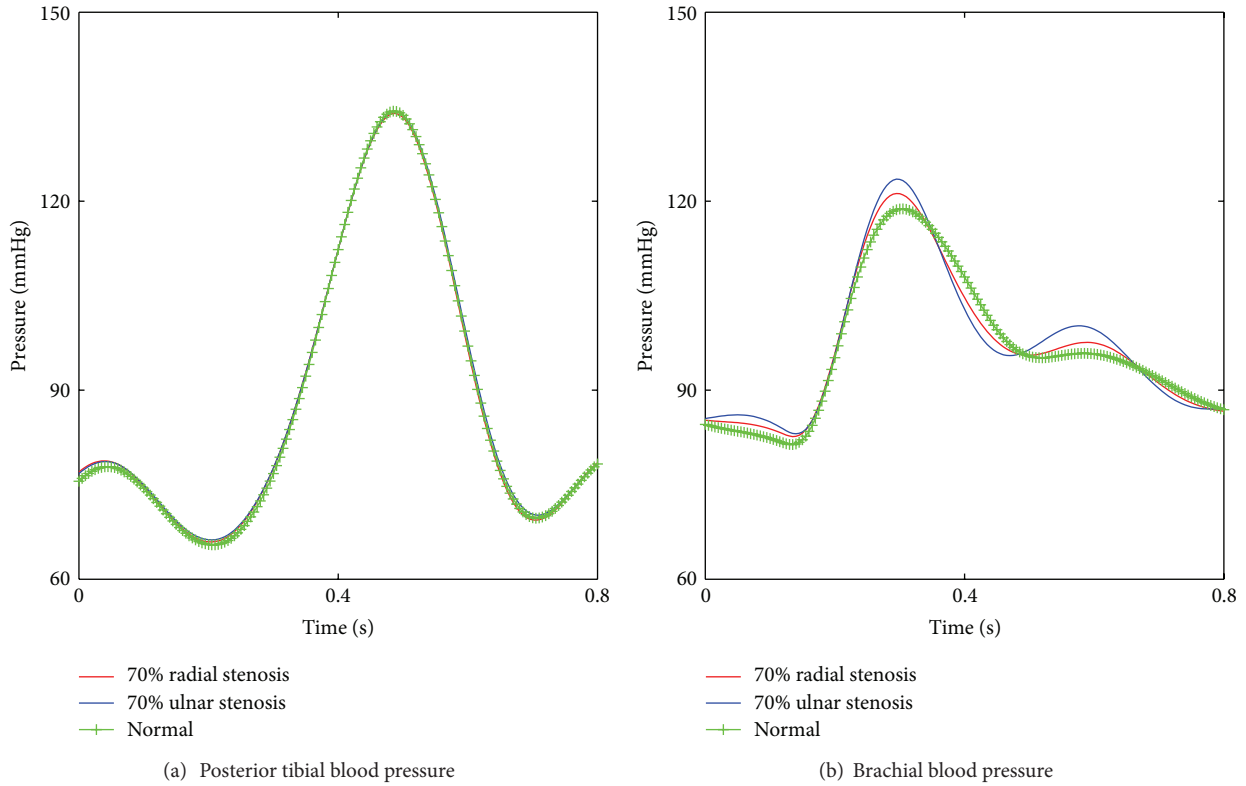


FIGURE 6: Comparison of the arterial blood pressure between the normal case and the cases with 70% radial stenosis and 70% ulnar stenosis respectively. (a) Posterior tibial blood pressure; (b) brachial blood pressure.

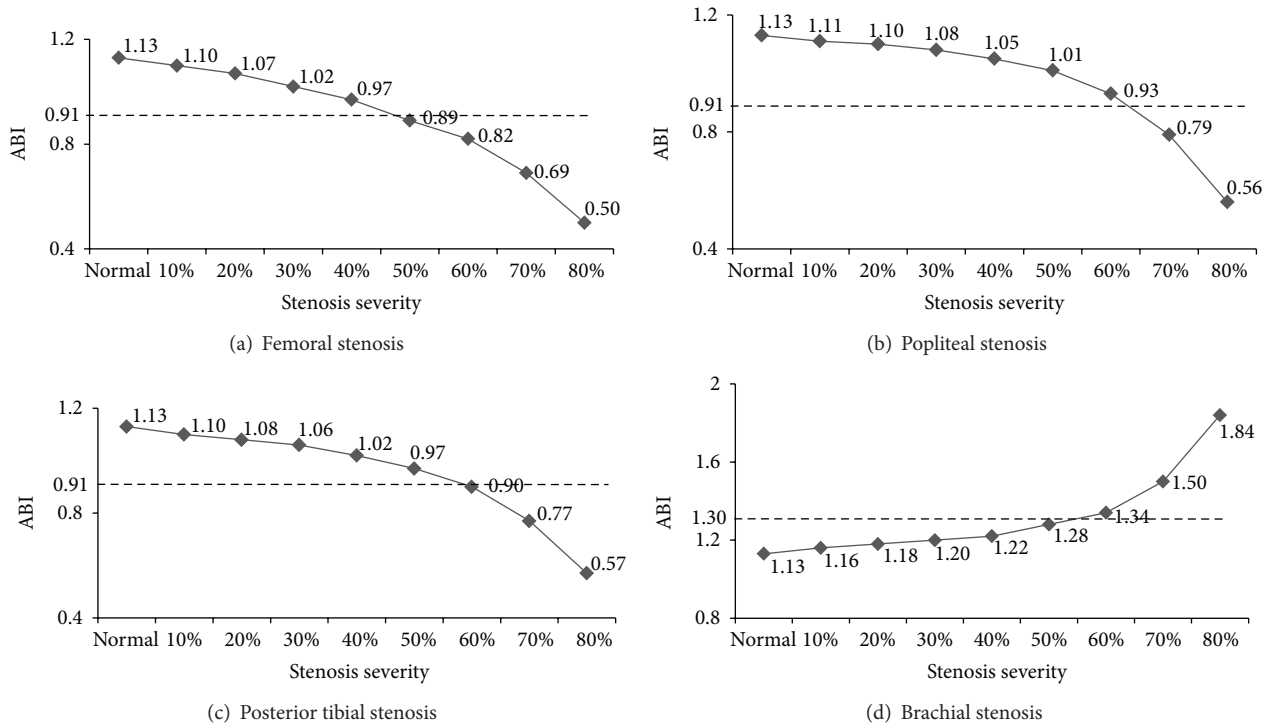


FIGURE 7: Changes of ABI value with stenosis increased from 0% to 80% at 4 arteries, respectively. (a) variation tendency of ABI with femoral stenosis; (b) variation tendency of ABI with popliteal stenosis; (c) variation tendency of ABI with posterior tibial stenosis; (d) variation tendency of ABI with brachial stenosis. The dotted line in each figure represents the evaluation standards of normal ABI (0.91~1.30) which is used as the threshold for stenoses diagnosis in clinical data.

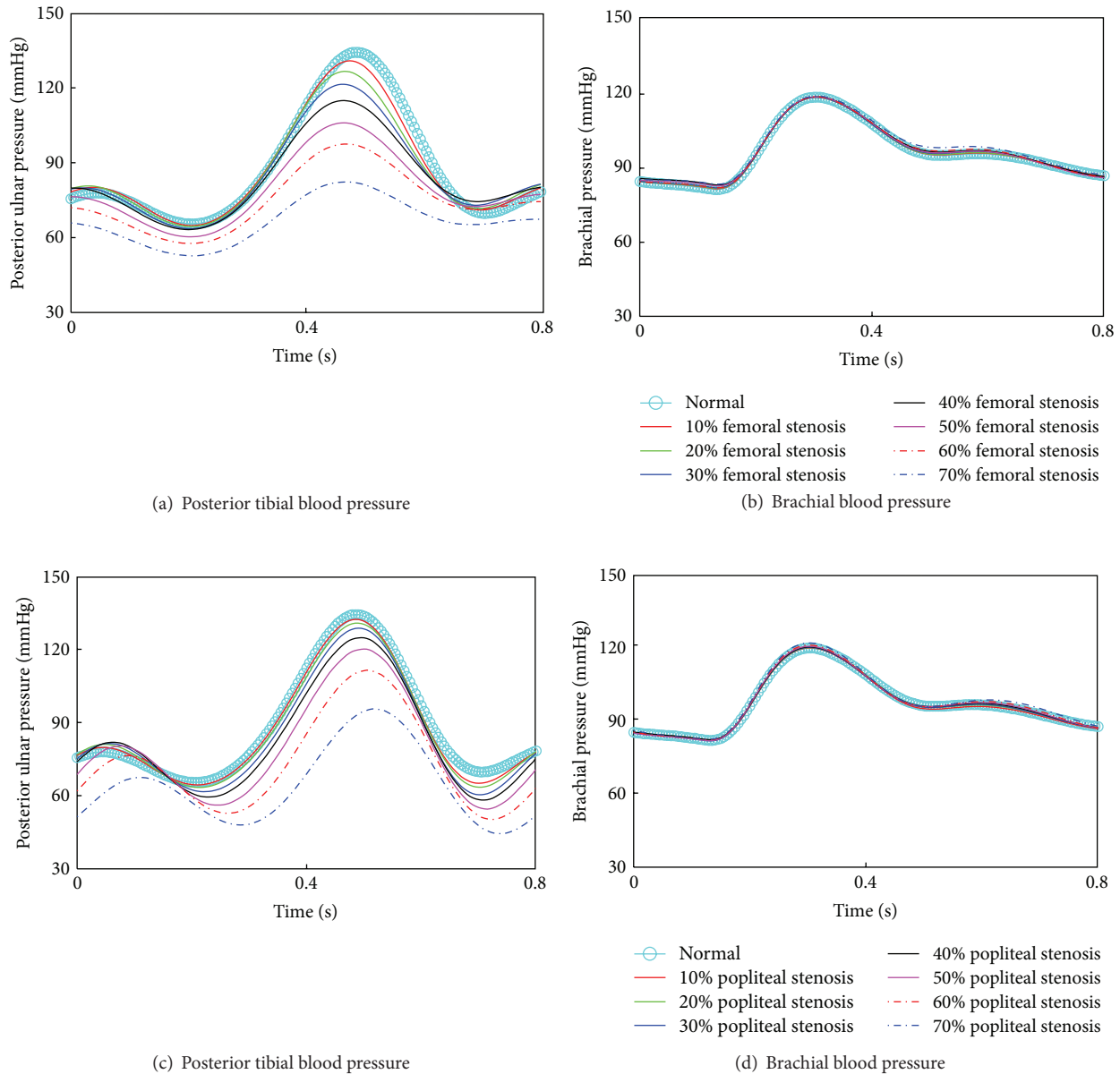


FIGURE 8: Blood pressure in a single cardiac cycle of posterior tibial artery and brachial artery with stenosis severities increasing from 0% to 70%. (a), (b): Stenoses located in femoral artery; (c), (d) Stenoses located in popliteal artery.

response to hemodynamic pressure changes caused by vascular stenoses and clearly depicts typical characteristic changes of the blood pressures. In clinical data, ABI is a useful, reliable and noninvasive method in detecting arterial stenoses, especially in diagnosing stenoses in lower extremity arteries. The model is thus applied to study the correlation between the stenosis and ABI.

Results show a strong location-dependence of ABI in predicting the stenosis. Stenoses located in the four arteries (femoral artery, popliteal artery, posterior tibial artery, and brachial artery) would cause significant variations of blood pressure in brachial and posterior tibial arteries, thus made ABI effective in diagnosing stenoses in these arteries. The main accomplishment of this study provides a theoretical

basis for clinical diagnosis. It is also validated that ABI is more sensitive to severe stenoses than to mild/moderate ones, which is supported by the clinical experience of ABI diagnosis. The main accomplishment of this study has revealed the reason for why ABI acts as an effective index for arterial stenoses detection, providing the theoretical basis for optimizing the application of ABI.

Acknowledgments

This study was supported by the National Key Technology R & D Program (2012BAI19B04), the National Natural Science Foundation of China (grants nos. 61190123 and 61101008), and

the grant from the State Key Laboratory of Virtual Reality Technology and Systems, Beihang University China.

References

- [1] N. Stergiopoulos, D. F. Young, and T. R. Rogge, "Computer simulation of arterial flow with applications to arterial and aortic stenoses," *Journal of Biomechanics*, vol. 25, no. 12, pp. 1477–1488, 1992.
- [2] D. F. Young and F. Y. Tsai, "Flow characteristics in models of arterial stenoses. I. Steady flow," *Journal of Biomechanics*, vol. 6, no. 4, pp. 395–410, 1973.
- [3] D. F. Young and F. Y. Tsai, "Flow characteristics in models of arterial stenoses. II. Unsteady flow," *Journal of Biomechanics*, vol. 6, no. 5, pp. 547–559, 1973.
- [4] D. Garcia, L. Kadem, D. Savéry, P. Pibarot, and L.-G. Durand, "Analytical modeling of the instantaneous maximal transvalvular pressure gradient in aortic stenosis," *Journal of Biomechanics*, vol. 39, no. 16, pp. 3036–3044, 2006.
- [5] S. Singh and R. R. Shah, "A numerical model for the effect of stenosis shape on blood flow through an artery using power-law fluid," *Advances in Applied Science Research*, vol. 1, no. 1, pp. 66–73, 2010.
- [6] R. N. Pralhad and D. H. Schultz, "Modeling of arterial stenosis and its applications to blood diseases," *Mathematical Biosciences*, vol. 190, no. 2, pp. 203–220, 2004.
- [7] R. Feng, M. Xenos, G. Girdhar et al., "Viscous flow simulation in a stenosis model using discrete particle dynamics: a comparison between DPD and CFD," *Biomechanics and Modeling in Mechanobiology*, vol. 11, no. 1-2, pp. 119–129, 2012.
- [8] E. R. Mohler III, "Peripheral arterial disease: identification and implications," *Archives of Internal Medicine*, vol. 163, no. 19, pp. 2306–2314, 2003.
- [9] S. T. Yao, J. T. Hobbs, and W. T. Irvine, "Ankle systolic pressure measurements in arterial disease affecting the lower extremities," *British Journal of Surgery*, vol. 56, no. 9, pp. 676–679, 1969.
- [10] K. I. Paraskevas, I. Kotsikoris, S. A. Koupidis, A. D. Giannoukas, and D. P. Mikhailidis, "Ankle-brachial index: a marker of both peripheral arterial disease and systemic atherosclerosis as well as a predictor of vascular events," *Angiology*, vol. 61, no. 6, pp. 521–523, 2010.
- [11] M. Decrinis, S. Doder, G. Stark, and E. Pilger, "A prospective evaluation of sensitivity and specificity of the ankle/brachial index in the follow-up of superficial femoral artery occlusions treated by angioplasty," *Clinical Investigator*, vol. 72, no. 8, pp. 592–597, 1994.
- [12] S. A. Carter, "Indirect systolic pressures and pulse waves in arterial occlusive diseases of the lower extremities," *Circulation*, vol. 37, no. 4, pp. 624–637, 1968.
- [13] X. Guo, J. Li, W. Pang et al., "Sensitivity and specificity of ankle-brachial index for detecting angiographic stenosis of peripheral arteries," *Circulation Journal*, vol. 72, no. 4, pp. 605–610, 2008.
- [14] A. V. Doobay and S. S. Anand, "Sensitivity and specificity of the ankle-brachial index to predict future cardiovascular outcomes: a systematic review," *Arteriosclerosis, Thrombosis, and Vascular Biology*, vol. 25, no. 7, pp. 1463–1469, 2005.
- [15] D. Xu, J. Li, L. Zou et al., "Sensitivity and specificity of the ankle-brachial index to diagnose peripheral artery disease: a structured review," *Vascular Medicine*, vol. 15, no. 5, pp. 361–369, 2010.
- [16] L. M. Ellwein, H. T. Tran, C. Zapata, V. Novak, and M. S. Olufsen, "Sensitivity analysis and model assessment: mathematical models for arterial blood flow and blood pressure," *Cardiovascular Engineering*, vol. 8, no. 2, pp. 94–108, 2008.
- [17] K. Lu, J. W. Clark, F. H. Ghorbel, D. L. Ware, and A. Bidani, "A human cardiopulmonary system model applied to the analysis of the Valsalva maneuver," *American Journal of Physiology. Heart and Circulatory Physiology*, vol. 281, no. 6, pp. H2661–H2679, 2001.
- [18] S. R. Pope, "Estimation and identification of parameters in a lumped cerebrovascular model," *Mathematical Biosciences and Engineering*, vol. 6, no. 1, pp. 93–115, 2009.
- [19] R. Mukkamala, *A Forward Model-Based Analysis of Cardiovascular System Identification Methods*, Massachusetts Institute of Technology, Cambridge, Mass, USA, 2000.
- [20] Z. Samar, *Cardiovascular Parameter Estimation Using a Computational Model*, Massachusetts Institute of Technology, Cambridge, Mass, USA, 2005.
- [21] T. Heldt, *Computational Models of Cardiovascular Response To Orthostatic Stress*, Massachusetts Institute of Technology, Cambridge, Mass, USA, 2004.
- [22] Y. B. Shi, P. Lawford, and R. Hose, "Review of zero-D and 1-D models of blood flow in the cardiovascular system," *BioMedical Engineering Online*, vol. 10, article 33, pp. 1–38, 2011.
- [23] H. Suga, K. Sagawa, and A. A. Shoukas, "Load independence of the instantaneous pressure-volume ratio of the canine left ventricle and effects of epinephrine and heart rate on the ratio," *Circulation Research*, vol. 32, no. 3, pp. 314–322, 1973.
- [24] H. Suga and K. Sagawa, "Instantaneous pressure volume relationships and their ratio in the excised, supported canine left ventricle," *Circulation Research*, vol. 35, no. 1, pp. 117–126, 1974.
- [25] M. S. Olufsen, J. T. Ottesen, H. T. Tran, L. M. Ellwein, L. A. Lipsitz, and V. Novak, "Blood pressure and blood flow variation during postural change from sitting to standing: Model development and validation," *Journal of Applied Physiology*, vol. 99, no. 4, pp. 1523–1537, 2005.
- [26] F. Y. Liang, S. Takagi, R. Himeno, and H. Liu, "Multi-scale modeling of the human cardiovascular system with applications to aortic valvular and arterial stenoses," *Medical and Biological Engineering and Computing*, vol. 47, no. 7, pp. 743–755, 2009.
- [27] A. P. Avolio, "Multi-branched model of the human arterial system," *Medical and Biological Engineering and Computing*, vol. 18, no. 6, pp. 709–718, 1980.
- [28] J. J. Wang and K. H. Parker, "Wave propagation in a model of the arterial circulation," *Journal of Biomechanics*, vol. 37, no. 4, pp. 457–470, 2004.
- [29] X. Li, J. Bai, S. Cui, and S. Wang, "Simulation study of the cardiovascular functional status in hypertensive situation," *Computers in Biology and Medicine*, vol. 32, no. 5, pp. 345–362, 2002.
- [30] M. Eslami, "Introduction to system sensitivity theory," *IEEE Transactions on Systems, Man and Cybernetics*, vol. 6, no. 10, pp. 337–338, 1980.
- [31] P. M. Frank, *Introduction To System Sensitivity Theory*, Academic Press, New York, NY, USA, 1978.
- [32] T. Lenhart, K. Eckhardt, N. Fohrer, and H.-G. Frede, "Comparison of two different approaches of sensitivity analysis," *Physics and Chemistry of the Earth*, vol. 27, no. 9-10, pp. 645–654, 2002.
- [33] Y. Sun, M. Beshara, R. J. Lucariello, and S. A. Chiaramida, "A comprehensive model for right-left heart interaction under the influence of pericardium and baroreflex," *American Journal of*

Physiology. Heart and Circulatory Physiology, vol. 272, no. 3, pp. H1499–H1515, 1997.

- [34] P. Reymond, *Pressure and Flow Wave Propagation in Patient-Specific Models of the Arterial Tree*, ETH Lausanne, Lausanne, Switzerland, 2011.
- [35] P. J. Blanco, S. M. Watanabe, and R. A. Feijoo, “Identification of vascular territory resistances in one dimensional hemodynamics simulations,” *Journal of Biomechanics*, vol. 45, no. 12, pp. 2066–2073, 2012.
- [36] A. Saltelli, S. Tarantola, and K. P.-S. Chan, “A quantitative model-independent method for global sensitivity analysis of model output,” *Technometrics*, vol. 41, no. 1, pp. 39–56, 1999.